

**SUBWAVELENGTH GRATINGS FOR POLARIZATION CONTROL IN  
TERAHERTZ AND VISIBLE FREQUENCY RANGES**

**DENG LIYUAN**

*(B. SCI.)*

*HUAZHONG UNIVERSITY OF SCIENCE & TECHNOLOGY*

**A THESIS SUBMITTED**

**FOR THE DEGREE OF PHILOSOPHY OF**

**ENGINEERING**

**DEPARTMENT OF ELECTRICAL AND COMPUTER ENGINEERING**

**NATIONAL UNIVERSITY OF SINGAPORE**

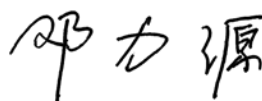
**2013**

## DECLARATION

I hereby declare that this thesis is my original work and it has been written by me in its entirety.

I have duly acknowledged all the sources of information which have been used in the thesis.

This thesis has also not been submitted for any degree in any university previously.



---

Deng Liyuan  
19 August 2013

## **Acknowledgements**

I owe my gratitude and appreciation to all the people listed below who have made my graduate study possible and a treasurable experience.

Firstly I'd like to express my deepest gratitude to my supervisors, Prof. Chua Soo Jin and Dr. Teng Jinghua. Being a reputational professor and creative scientist, Prof Chua made my doctoral research a truly pleasant one. He gave me the freedom to explore topics I am interested in. Meanwhile, he provided me the necessary guidance in thinking and behaving professionally. With his years of experience in semiconductor and photonic devices, Dr. Teng always suggested brilliant and practical ideas. He also gave advice to solve the difficulties I encountered in experiments and kindly provided necessary resources through collaboration.

I would like to thank Dr. Zhang Liang, an alumni from Prof Chua's group, for the tremendous guidance and help in the early years of my PhD study. He shared his experience in experiments and insights in graduate study without reservation. Without his suggestions and help, my PhD study would be much harder.

I am grateful to members of Dr. Teng's group and researchers in IMRE who have helped me a lot in the fabrication and measurement. Mr. Norman Ang taught me every detail step of fabricating GaN LED. Mr. Chum's excellent EBL technique makes the polarized LED project successful. I extend my thanks to Dr. Zhang Xinhai, Dr. Hendrix, Mr. Steve Wu and Ms. Liu Hongwei, for their help in the THz measurements and valuable technical discussion. I'd like to express my gratitude and respect to Dr. Liu Hongfei, who showed me by himself what is

the true passion to scientific research.

I also would like to thank my friends and colleagues in the center for optoelectronics (COE), including Ms. Tang Jie, Mr. Liu Yi, Mr. Huang Jian, Ms. Gao Hongwei, Ms. Niu Jing and Mr. Zhang Li, for their friendship and collaboration. The four years' PhD time spent together with you guys is truly wonderful.

Most of all, I would like to specially thank my parents, my brother and my sister for their endless love and support through all these years. The warmth of family provides me the forward momentum forever.

# Table of Contents

Acknowledgements.....	ii
Table of Contents .....	iv
Summary.....	viii
List of Figures .....	x
List of Tables.....	xiii
List of Publications .....	xiv
Chapter 1 Introduction .....	1
1.1 Overview .....	1
1.1.1 Subwavelength Grating.....	1
1.1.2 Terahertz Waves .....	8
1.1.3 GaN LEDs.....	10
1.2 Motivation.....	12
1.3 Organization of the Thesis .....	13
Chapter 2 Simulation and Theory .....	15
2.1 Introduction.....	15
2.2 Simulation .....	15

2.2.1 Finite-Difference Time-Domain Method.....	15
2.2.2 Lumerical FDTD.....	18
2.3 Surface plasmon resonances .....	19
2.3.1 Surface Plasmons Polaritons at the Planar Interface.....	20
2.3.2 Localized Surface Plasmon Resonance .....	24
2.3.3 THz plasmonics .....	27
2.4 Summary .....	30
Chapter 3 Fabrication and Characterization Equipment.....	31
3.1 Introduction.....	31
3.2 Fabrication Equipment.....	31
3.2.1 Photolithography.....	31
3.2.2 Electron-beam Lithography .....	35
3.2.3 Reactive Ion Etching.....	37
3.2.4 Deep Reactive Ion Etching .....	39
3.3 Characterization Equipment.....	40
3.3.1 Scanning Electron Microscope .....	40
3.3.2 Fourier transform infrared spectroscopy.....	43
3.3.3 THz time-domain spectroscopy .....	45

3.3.4 Optical-pump THz-probe spectroscopy .....	47
3.4 Summary .....	50
Chapter 4 Application of Subwavelength Metallic Grating as a High Performance THz Polarizer .....	52
4.1 Introduction.....	52
4.1.1 Linear polarizer .....	52
4.1.2 THz polarizer .....	53
4.2 Grating Design .....	54
4.3 Grating Fabrication .....	63
4.4 Results and Discussion .....	65
4.5 Summary .....	68
Chapter 5 Application of InSb Subwavelength Gratings as an All Optical Terahertz Plasmonic Modulator.....	69
5.1 Introduction.....	69
5.1.1 InSb as the THz plasmonics Material .....	69
5.2 Subwavelength Grating Design and Fabrication .....	72
5.3 Characterization and Discussion.....	75
5.4 Summary .....	83

Chapter 6 Application of Subwavelength Grating in Visible Range to Realize a Polarized InGaN Light Emitting Diode .....	85
6.1 Introduction.....	85
6.1.1 Polarized LED.....	85
6.2 Subwavelength Grating Design .....	87
6.3 Polarized LED fabrication .....	93
6.3.1 GaN LED fabrication.....	93
6.3.2 Subwavelength Al grating fabrication .....	95
6.4 Polarized LED Characterization .....	97
6.5 Summary.....	103
Chapter 7 Summary and Future Work .....	104
Bibliography .....	108
List of Acronyms.....	115



## Summary

Subwavelength grating has become an important component in modern optics and photonics, being widely used as polarizer, wave plate, beam collimator and anti-reflection coating. The design flexibility of this artificial structure has enabled numerous properties and applications that are unachievable with natural materials to be realized. The recent decades have witnessed the huge surge of research interest in terahertz waves and GaN LEDs. THz wave, the latest explored electromagnetic wave band, has unique properties and could be used in areas such as security screening, medical imaging and communication. Due to the lack of materials that naturally response to THz waves, subwavelength grating based devices are excellent candidates for THz components, such as THz polarizer and modulator. Subwavelength grating integrated with conventional LED can generate polarized emission, which greatly broadens the applicability of LEDs.

In this thesis, we have studied three applications of subwavelength gratings for polarization control in terahertz and visible frequency ranges. The devices were fabricated through various micro- and nano-fabrication techniques. Firstly, we demonstrated an extremely high performance THz polarizer with bilayer metallic wire-grid structure. The polarizer was tested by THz-TDS and showed an average extinction ratio of 69.9 dB in a broad frequency range of 0.6 - 3 THz and maximum extinction ratio of 84.9 dB at 1.67 THz, outperforming all the THz polarizers ever demonstrated. Next, the optically tunable THz plasmonic response of InSb subwavelength grating was studied. By optically pumping the InSb with a 405 nm wavelength

laser emitting at 120 mW, the transmittance at 1.5 THz was reduced from 0.6 to 0.32, a change of 46.7%. At laser pump fluence of  $0.74 \mu\text{J}/\text{cm}^2$ , the excited carrier lifetime was determined to be 834 ps using optical pump-THz probe technique, giving a potentially high-speed THz modulator with modulation speed up to 1.2 GHz. Finally, a polarized GaN LED integrated with Al subwavelength grating was demonstrated. Al grating with a period of 200 nm, Al thickness 200 nm and duty cycle 50% was fabricated on top of the p-contact of conventional GaN LED. The polarization ratio achieved was 5.6 for blue GaN LEDs and 2.1 for green ones.

## List of Figures

<b>Figure 1.1</b> Schematic of subwavelength grating. $P$ , grating period; $\lambda$ , wavelength of incident light; $a$ , half the size of grating elements; $R_0$ , 0 <sup>th</sup> order reflection; $T_0$ , 0 <sup>th</sup> order transmission...	2
<b>Figure 1.2</b> Location of the “THz wave” in the whole electromagnetic spectrum, adopted from Ref. [27].	8
<b>Figure 1.3</b> Band gap, emission wavelength and lattice constant of various semiconductor materials, adopted from Ref. [37].	12
<b>Figure 2.1</b> Yee lattice for FDTD calculation.	16
<b>Figure 2.2</b> Interface of the Lumerical FDTD software.	19
<b>Figure 2.3</b> Coordinates of SPP propagation at a planar interface between a metal and a dielectric. $P$ -polarized light is also plotted.	22
<b>Figure 2.4</b> Schematic of a subwavelength sphere placed into an electrostatic field.	25
<b>Figure 3.1</b> Schematic of photolithography using positive and negative photoresist.	32
<b>Figure 3.2</b> Typical process flow of photolithography.	33
<b>Figure 3.3</b> (a)-(b): Images of photoresist (AZ 5214E) grating lines of 1 $\mu\text{m}$ width, viewed from top and side respectively. (c)-(e): Optical microscopic images of photoresist patterns in different steps of GaN LED fabrication.	34
<b>Figure 3.4</b> Elionix ELS-7000 e-beam lithography system.	37
<b>Figure 3.5</b> 200 nm period grating on ZEP 520A with different dilute strength. (a) undiluted; (b) 1:1 diluted with Anisol.	37
<b>Figure 3.6</b> A Si grating obtained in this work after DRIE with photoresist unstripped.	40
<b>Figure 3.7</b> Basic working principle of a SEM.	41
<b>Figure 3.8</b> Illustration of signals produced by interaction of electrons with atoms.	42
<b>Figure 3.9</b> Schematic of Fourier transform infrared spectroscopy.	44
<b>Figure 3.10</b> Schematic of the setup for THz-TDS, adopted from Ref. [30].	46

<b>Figure 3.11</b> Schematic for (a) photoconductive emitter and (b) photoconductive detector, adopted from Ref. [50].	47
<b>Figure 3.12</b> Schematic of OPTP setup used in this project.	49
<b>Figure 3.13</b> Electro-optical rectification of ZnTe for THz generation.	50
<b>Figure 3.14</b> Schematic of electro-optical sampling.	50
<b>Figure 4.1</b> Schematics of (a) SWGP and (b) BWGP. P: wire-grid period; w: metal wire width; t: metal layer thickness; d: metal layer spacing. Normally incident THz radiation with TM or TE polarization is also indicated. H: magnetic field; E: electric field.	56
<b>Figure 4.2</b> Complex permittivity of three metals (Au, Al and Ag) in THz frequency range.	56
<b>Figure 4.3</b> FDTD simulation results of the TM transmittance and ER of SWGPs with different periods.	58
<b>Figure 4.4</b> (a) TM transmittance and (b) ER as a function of frequency (0.6 – 3 THz) when the Au thickness is increased from 50 nm to 400 nm. Period and duty cycle are fixed at 4 $\mu\text{m}$ and 50%, respectively.	59
<b>Figure 4.5</b> Comparison of polarization performance of SWGP with that of BWGP by FDTD analysis. (a) Frequency dependent TM and TE transmittances. (b) ER as a function of frequency. Lines with solid squares are for BWGP and lines with open square are for SWGP.	61
<b>Figure 4.6</b> Dependence of the performance of BWGP on (a) metal thickness and (b) two metal layer spacing by FDTD analysis.	62
<b>Figure 4.7</b> Scanning electron micrographs of the fabricated BWGP. (a) Top view; (b) Cross-section view. Inset: Enlarged view of the Si ridge and two metal layers.	64
<b>Figure 4.8</b> Electric field signals in time domain for (a) TM polarized incident wave and (b) TE polarized incident wave passing through the fabricated WGPs. Inset: Normalized transmittance of BWGP as a function of polarizer angle at 1 THz and the corresponding fitting curve to $\cos^2\theta$ .	67
<b>Figure 4.9</b> (a) TM and TE transmittance and (b) ER of the WGPs as a function of frequency.	67
<b>Figure 6.1</b> Schematic diagram of the GaN LED integrated with subwavelength grating.	87

<b>Figure 6.2</b> Polarization performances of subwavelength gratings made by different metals, Al, Ag and Au. ....	89
<b>Figure 6.3</b> Dependence of polarization performance on grating period. ....	89
<b>Figure 6.4</b> Dependence of polarization performance on metal thickness. ....	90
<b>Figure 6.5</b> Dependence of polarization performance on grating duty cycle. ....	91
<b>Figure 6.6</b> FDTD simulation results of the polarization performance of grating with optimized parameters. ....	92
<b>Figure 6.7</b> Schematic diagrams of the fabrication steps of GaN LED. ....	93
<b>Figure 6.8</b> Schematic diagrams showing the fabrication steps of Al subwavelength grating. ....	96
<b>Figure 6.9</b> SEM pictures of (a) resist grating after e-beam exposure and developing; (b) after RIE etching of SiO <sub>2</sub> ; (c) top view of the final Al grating; (d) cross-sectional view of the final Al grating. ....	96
<b>Figure 6.10</b> (a) I-V curve of the fabricated LED, showing a turn-on voltage of 3.5 V. (b) Output power from the front surface of LED as a function of injection current. The photodetector of the power meter was placed 20 mm above the LED surface. ....	99
<b>Figure 6.11</b> Electroluminescence (EL) spectra of the fabricated GaN LED under different injection currents. There is a slight blue-shift as the current is increased from 1 to 70 mA. ..	99
<b>Figure 6.12</b> Transmission and ER of the Al nanograting on quartz substrate. The nanograting's parameters are: Al thickness 190 nm, grating period 200 nm, and duty cycle 55%. ....	100
<b>Figure 6.13</b> Polarization measurement of the polarized green GaN LED. ....	101
<b>Figure 6.14</b> Polarization measurement of the polarized blue GaN LED. ....	102
<b>Figure 6.15</b> SEM image of the fabricated Al nanograting on a green GaN LED. ....	102

## List of Tables

<b>Table 3.1</b> Typical photolithography parameters used in this work.....	34
<b>Table 3.2</b> Etching parameters for several materials used in this thesis.....	39
<b>Table 4.1</b> Dimensions of the four polarizers fabricated.....	64
<b>Table 5.1</b> Mobility and plasma frequency of InSb with different carrier concentrations [76]. .....	71

## List of Publications

### Patent:

- (1) J. H. Teng, S. J. Chua, L. Zhang and **L. Y. Deng**, “GaN LED with Polarized Light Emission”, US 12/939,322, (2010);

### Papers:

- (1) **Liyuan Deng**, Jinghua Teng, Hongwei Liu, Qing Yang Wu, Jie Tang, Xinhai Zhang, Stefan A. Maier, Kian Peng Lim, Chun Yong Ngo, Soon Fatt Yoon, and Soo Jin Chua, “Direct Optical Tuning of the Terahertz Plasmonic Response of InSb Subwavelength Gratings.” *Advanced Optical Materials*, 1, 128 (2013);
- (2) **Liyuan Deng**, Jinghua Teng, Liang Zhang, Qing Yang Wu, Hong Liu, Xinhai Zhang and Soo Jin Chua, “Extremely High Extinction Ratio Terahertz Broadband Polarizer Using Bilayer Subwavelength Metal Wire-grid Structure.” *Applied Physics Letters*, 101, 011101 (2012);
- (3) **Liyuan Deng**, Jinghua Teng, Jian Huang, Norman Ang, Chum Chan Choy and Soo Jin Chua, “GaN Light Emitting Diode with High Extinction Ratio Linearly Polarized Light Emission.” Manuscript under preparation;
- (4) Jian Huang, Kar Hoo Patrick Tung, **Liyuan Deng**, Ning Xiang, Jianrong Dong, Aaron James Danner and Jinghua Teng, “Surface Plasmon Enhanced Photoluminescence in Gold Capped InGaAs Quantum Disk Array.” *Optical Materials Express*, 3, 2003 (2013);
- (5) Jie Tang, **Liyuan Deng**, Chuan Beng Tay, Nguyen Xuan Sang, Xinhai Zhang, Jianwei Chai, Hao Qin, Thirumalai Venkatesan, and Soo Jin Chua, “Determination of the carrier concentration dependent electron effective mass of n-type ZnO thin film by terahertz time domain spectroscopy.” *Journal of Applied Physics*, 115, 033111 (2014);
- (6) Liang Zhang, Jinghua Teng, Hendrix Tanoto, Sooyee Yew, **Liyuan Deng** and Soo Jin Chua, “Terahertz wire-grid polarizer by nanoimprinting lithography on high resistivity

silicon substrate”, *IRMMW-THz (Infrared Millimeter and Terahertz Waves)*, Sept. 2010, pp.1-2;

### **Conference presentations:**

- (1) **L. Y. Deng**, J. H. Teng and S. J. Chua, “Optical Tuning of the Terahertz Plasmonics Response of InSb Subwavelength Gratings.” *OTST 2013 (International Workshop on Optical Terahertz Science and Technology)*, Kyoto, Japan, Apr. 1-5, 2013;
- (2) **L. Y. Deng**, J. H. Teng, C. C. Chum and S. J. Chua, “Polarized Light Emission from InGaN Light Emitting Diode by Utilizing Subwavelength Metallic Grating Structure.” *MRS Fall Meeting 2012*, Boston, U.S., Nov. 25-30, 2012;
- (3) **L. Y. Deng**, C. M. Lai, C. C. Chum, J. H. Teng and S. J. Chua, “Design and Fabrication of InGaN/GaN Light Emitting Diode with Polarized Light Emission.” *ICYRAM 2012 (International Conference of Young Researchers on Advanced Materials)*, Singapore, July 1-6, 2012;
- (4) **L. Y. Deng**, J. H. Teng, Q. Y. Wu, H. Liu, X. H. Zhang, and S. J. Chua, “Broadband terahertz polarizer with extremely high extinction ratio based on bilayer metal wire-grids.” *2<sup>nd</sup> ECE Graduate Student Symposium (NUS)*, Singapore, May 10-11, 2012;
- (5) **L. Y. Deng**, J. H. Teng, Q. Y. Wu, H. Liu, X. H. Zhang, and S. J. Chua, “High Performance Bilayer Metallic Wire-grid Polarizer for Terahertz Wave.” *5<sup>th</sup> MRS-S Conferences on Advanced Materials*, Singapore, March 20-22, 2012;
- (6) **L. Y. Deng**, S. S. Norman, S. J. Chua and J. H. Teng, “GaN Light Emitting Diode with Linearly Polarized Light Emission.” *ICMAT 2011 (International Conference on Material for Advanced Technologies)*, Singapore, June 26-July 1, 2011;



# Chapter 1 Introduction

## 1.1 Overview

### 1.1.1 Subwavelength Grating

In the past decades, more compact and faster electronic chips with sub-micrometer-size critical dimensions (CD) have been manufactured benefiting from the advancement of nanofabrication technologies. As pointed out by the report of International Technology Roadmap for Semiconductors 2011, IC production will achieve 23 nm lithographic CD by year 2015 [1]. Apart from the remarkable achievements in microelectronics, advanced nanofabrication techniques have also enabled people in photonic community to realize structures with size well below the wavelength of light, exhibiting enormous novel functionalities. One-dimensional (1D) or two-dimensional (2D) grating structures with period smaller than the wavelength of light - called “subwavelength grating”- are typical examples. From the view point of grating diffraction, as the wavelength-to-period ratio is larger than 1, no diffraction orders exist and only specular orders propagate, as illustrated in **Figure 1.1**. Therefore, it is also called “zero-order grating” or “high spatial-frequency grating” in some literatures. Depending on which frequency range of the electromagnetic spectrum is used, subwavelength grating can be fabricated by different methods, i.e. mechanical machining for usage in microwave or lower frequencies, photolithography for terahertz (THz) to mid-infrared ranges, and e-beam/nanoimprinting lithography for visible to ultraviolet ranges.

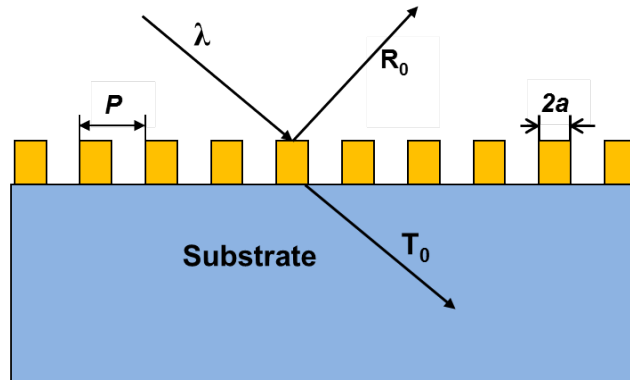


**Figure 1.1** Schematic of subwavelength grating.  $P$ , grating period;  $\lambda$ , wavelength of incident light;  $a$ , half the size of grating elements;  $R_0$ , 0<sup>th</sup> order reflection;  $T_0$ , 0<sup>th</sup> order transmission.

Subwavelength grating, as an artificial structure exhibiting various interesting behaviors, has long been an active research topic and finds applications in optical components, such as polarizer, beam splitter, beam collimator, filter or in newly developed plasmonic and metamaterial devices.

The polarization effect of subwavelength transmission grating was firstly noticed by Heinrich Hertz in 1888 [2]. He observed that when the electric field of normally incident radiation was oriented parallel to the diffraction grating elements, no energy could be detected beyond the grating. On the other hand, when the electric field of normally incident field was perpendicular to the grating elements, the transmitted energy was almost same as the incident radiation. Wavelength of the radiation Hertz used was approximately 66 cm and the diffraction grating was constructed of 1-mm-diameter copper wires with a separation of 3 cm.

During the ensuing years many attempts were made to gain complete and detailed experimental data and also to develop a satisfactory theoretical model to explain this phenomenon. However,

on the experimental side, the data acquired by early investigators were unreliable [3]. That was mainly caused by the lack of a constant source giving reliable monochromatic radiations with sufficient intensity and also the lack of reliable detectors. The first one to give theoretical interpretation of the Hertz's effect was J. J. Thomson in 1892 [4]. Thomson restricted his study to the case where the wave was incident normally on the grating and the electric field of the incident wave was parallel to the grating element. The assumption  $\lambda \gg P$ , where  $\lambda$  is the wavelength and  $P$  is the period of grating, was applied to the case he studied. Thomson proposed that incident radiation on the grating would induce current flowing in the wires, and that these currents would in turn generate electromagnetic field in the space surrounding the wires. This generated field at some distance from the grating would be nearly the same in magnitude as the case if the grating were a continuous metal surface, although there would be an alternation in phase. Thomson's results indicated that the parallel electric field would be totally reflected, independent of the wire size. Although Thomson's opinion provided an easy-to-understand physical model to explain the main feature of the Hertz's effect, his conclusion that the reflection was independent of wire geometry was shown later to be incorrect. In 1898, Horace Lamb gave a more complete investigation of the phenomenon by solving the two-dimensional, time-independent wave equations with proper boundary conditions under the assumption of  $\lambda \gg P$  [5]. Contrary to the conclusions of Thomson, his results indicated a dependence of the transmitted intensity on the size of the wires being used. Between 1905 and 1915, W. Von Ignatowsky presented the first exact treatment of grating

diffraction in a series of his papers [6]. His considerations were completely general with no assumptions on geometry of the grating elements. From his calculation, the transmitted intensity was given in the form of an infinite series with terms of the expansion being dependent upon inverse powers of  $(1-\lambda/P)$ .

For a period of around 30 years after the work of Ignatowsky, little was done on the subject either from theory or experiment part. Interest in the topic was renewed with the development in radar and microwaves techniques during the World War II, although still under the situations where  $\lambda \gg P$  and  $P \gg a$ . In 1939, W. Wessel gave a more careful treatment of the concept of induced current in the metal wires proposed by J. J. Thomson [7]. He achieved an analytical expression for the transmission coefficient by determining the magnitude of the current in the wire in term of the resistance and self-inductance of the grating using integral equations method. Agreement between the transmission coefficients given by Lamb, Ignatowsky and Wessel improved considerably for larger values of  $\lambda/P$  and  $P/a$ . In the same year, the theoretical results obtained by Wessel were verified experimentally by Esau, Ahrens, and Kebbel. Meanwhile, R. Honerjager investigated the transmission for the parallel orientation as a function of incident angle [8]. The previous investigations were all focused on microwave or even longer wavelengths, where metals (materials of grating elements) were treated with infinite conductivity. Lewis and Casey extended the results of Wessel and Honerjager to the case of the grating elements with finite resistivity [9]. However at that time it was just an anticipated effect for a grating in the near infrared or at even higher frequencies, which could

not be realized by experimentalist. In 1956, after detailed experiments in the microwave and infrared (IR) frequency ranges, Pursley demonstrated that the performance of grating in the microwave region could be extrapolated to the IR if the geometry of the grid was reduced linearly with the wavelength ( $\lambda/P$  as constant) [10]. The empirical coefficients obtained for wire gratings were also compared with those calculated from the first and second orders approximations of the exact series solution derived by Ignatowsky. For large  $P/a$  (10 or more), the first and second order approximations had nearly identical values and were closely matched to the measurement. As  $P/a$  decreased, higher order approximations were necessary, especially as  $\lambda/P$  approaches unity. However, higher approximations of the series solution became difficult to evaluate.

According to Pursley, the wire-grid transmission polarizer should be applicable to even higher frequency ranges like IR, near-IR or visible. In radio and microwave frequencies, as the wavelength is very large, the metal wires used usually have the dimension of several mm or sub-mm and was assembled into a grating by winding onto a frame. It is obvious that a grid of unsupported metal wires becomes fragile and is more difficult to construct when the dimension of wires is only tens of micrometers or smaller, which is desirable for applications at higher frequencies. In 1960, Bird and Parrish overcame the problem by supporting the metal grid with a plastic substrate ( $\text{CF}_2\text{CFCI}$ ) [11]. They used a plastic grating replica as a substrate and deposited metal onto the tips of the grooved faces by oblique evaporation at nearly grazing incidence to the grating surface. IR polarizers on other substrates like polymethylmethacrylate

(PMMA) or polyethylene were fabricated using the same method [12]. However, the limitation of this method is that the substrates were restricted to materials that can be formed into replicas only. Also the shape of fabricated metallic grating was not regular.

The progress in the development of subwavelength grating was slow in both theory and fabrication parts. Rigorous solutions of Maxwell's equations in the complex models are needed to calculate the transmission coefficients. Meanwhile, before 1960s, the fabrication capability limits the realization of subwavelength gratings of smaller feature sizes applicable at higher frequencies.

To solve these problems, simplified approaches based on appropriate assumptions were developed in theories, among which was the effective medium theory (EMT) proposed in 1950s. More excitingly, with the development of computer science and algorithm from 1970s, scientists have developed a completely new way to solve Maxwell's equations through numerical iteration. Most commonly used methods nowadays include finite-element method, finite-difference method, and beam propagation method. The advances of numerical methods have allowed people to easily design various optical components using subwavelength structures.

In fabrication, very large scale integration (VLSI) fabrication techniques (primarily photolithography and etching) were developed in 1960s. It facilitated in solving the fabrication issues and realizing devices that were impossible in the past. These novel optical devices with subwavelength structures fabricated by VLSI techniques have the advantages of reduction in

size and weight, elimination of exotic materials, increased design freedom and capability of integration. With the decrease in the critical dimension, the usage of metal wire grids as polarizers have been pushed to higher frequencies like visible or even ultraviolet. Also the precisely defined grating profiles achieved by advanced fabrication techniques facilitated the comparison of experimental results with theoretical ones.

In 1967, Auton used lithographic method to fabricate infrared transmission polarizers for the first time [13]. By using this advanced fabrication technique, gratings can be formed on many different substrates like silicon or germanium with well-defined metal wire profiles. After that various lithography methods have also been utilized to fabricate subwavelength grating polarizers, for example, laser interference lithography [14], nanoimprinting lithography [15], electron-beam lithography [16], and many others [17]. It should be noted that nanoimprinting lithography has become a cheaper and more efficient approach to fabricate subwavelength wire grids on large area, facilitating the development and commercialization of wire-grid based polarizers significantly [18, 19]. Alternative fabrication approaches for fabricating visible and UV wavelength range wire-grid polarizers other than solely decreasing the period have been proposed to ease the fabrication challenge and gain high performance, such as double patterning method [20, 21], and bilayer subwavelength gratings [22]. Subwavelength grating polarizer made of dielectric materials (amorphous silicon,  $\text{SiO}_2$ ) working in resonant conditions and on various different substrates were also studied [23].

Subwavelength grating polarizers have been integrated with other optoelectronic devices to

achieve novel properties, such as high brightness and high contrast LCD [24], polarization-sensitive photodetector [25], polarized LED [26] and so on.

### 1.1.2 Terahertz Waves

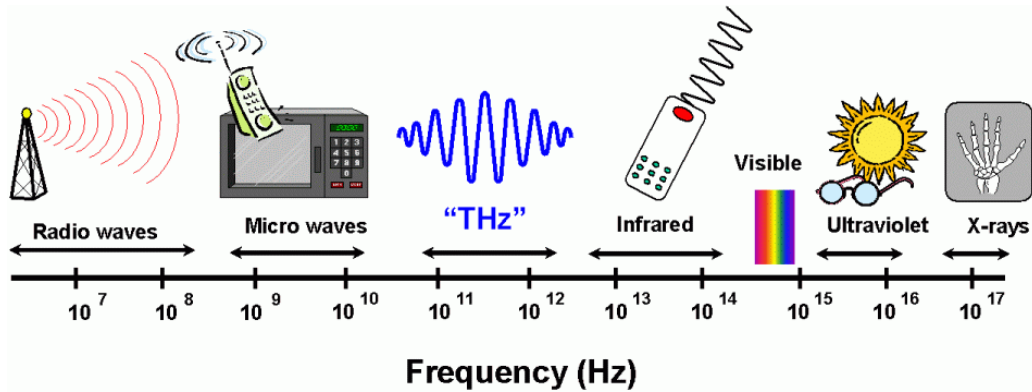


**Figure 1.2** Location of the “THz wave” in the whole electromagnetic spectrum, adopted from Ref. [27].

THz waves are generally referred to electromagnetic waves with frequencies ranging from 0.1 to 10 THz, which has long remained undeveloped mainly due to the lack of compact and efficient radiation sources and detectors [27]. As shown in **Figure 1.2**, THz radiation lies between the microwave and the infrared light in the electromagnetic spectrum. Semiconductor electronic devices (such as transistors) that are used to generate radio or micro waves can only reach up to hundreds of gigahertz. The output power of these devices falls as  $1/f^4$  or faster since their operation is dependent on transport of charge carriers, which is limited by both carrier transit time and parasitic capacitances in devices and circuits [28]. Consequently, electromagnetic wave emitted from electronic devices is limited to below 1 THz. On the other



hand, photonic devices (such as laser diodes) operating at much higher frequencies emit light as a result of quantum-mechanical energy level transition, which have their minimum achievable frequency limit imposed by electronic bandgap. The emitted light is limited to above 10 THz even using small bandgap materials such as lead-salts. Limitations of two wave generation approach forms the so-called “THz gap” [29].

Although being the least researched and developed in the whole electromagnetic spectrum, THz radiation has unique properties that inherently make it an important medium for various applications [30]. For instance, the ability of THz radiation to penetrate through many optically opaque materials has enabled applications in safety, security and non-invasive diagnostics. Although X-ray and microwave can also transmit through similar substances, THz radiation has the advantage of being non-ionizing compared to X-rays, because of its low photon energy of THz radiation (1 THz corresponds to photon energy 4.14 meV) and rendering much higher spatial resolution compared to microwave in imaging applications due to its shorter wavelength. Moreover, many large molecules have fingerprint absorption in THz region, enabling the spectroscopic analysis of material composition and detection of toxic and explosive materials in security screening. THz spectroscopy is also a wonderful tool for physicists and chemists to study rotational or vibrational modes of molecules. THz technology is also widely used in astronomy and atmospheric science. For astronomers, light emitted by cool interstellar dust, which falls in the terahertz frequency range, gives information about the formation of stars and planet. For atmospheric scientist, many gases in the upper atmosphere

have thermal emission lines at THz frequencies which give information on ozone destruction, global warming and pollution.

Since the 1990s, big breakthroughs in THz generation and detection techniques, such as THz quantum cascade laser [31] and time-domain spectroscopy, have aroused great interest and promoted the huge development in more efficient THz emitters [32], detectors [33], and THz components [34]. Among them, high performance THz polarizers, as a quasi-optical device to manipulate the THz waves, are highly demanded for THz spectroscopy and imaging applications.

### **1.1.3 GaN LEDs**

A light emitting diode (LED) is a semiconductor light source, which consists of a diode junction formed by p-type and n-type semiconductors. When the diode is properly biased, electrons from n-type semiconductor and holes from p-type semiconductor are able to recombine in the vicinity of the junction, releasing energy in the form of photons. LED was first created in 1927 [35, 36], but the first practical LED in visible range was developed by 1962. After that, tremendous progress has been achieved in this exciting area. Compared to conventional light sources like incandescent bulb or fluorescent lamp, LEDs present the advantages including higher efficiency, lower energy consumption, longer lifetime, smaller size, more flexible color temperature, improved physical robustness, lower cost, and also faster switching. LEDs are regarded as the next generation light source, and have been used in applications as diverse as traffic light signals, automotive lighting, large-panel display,

backlighting for LCD screen, decoration lighting, and optical fiber telecommunication systems.

Color of LED is determined by the band gap of the semiconductor material, as illustrated in **Figure 1.3** [37]. It shows that the InGaN material system is able to cover the whole visible range of the electromagnetic spectrum. InGaN LED was developed in the early 1990s and became commercially available in the late 1990s, largely due to the efforts of Prof. Shuji Nakamura and Nichia Chemical Industries Corporation [38]. Nowadays, InGaN has become the primary material for blue and green LEDs. InGaN red LED is still a challenge to make and is under intense research. Now the main research emphasis of GaN society is on how to furthermore improve the light emission efficiency and realize white/high power LED. On the other hand, special-functional LEDs such as LEDs with polarized light emission are also highly desirable for their potentials in making display and imaging systems more compact and robust. Polarized LED can be used as back-lighting for LCD, which increases the contrast of display image. In addition, polarized light carries additional information, which is useful in polarization resolved microscopy and 3D display.

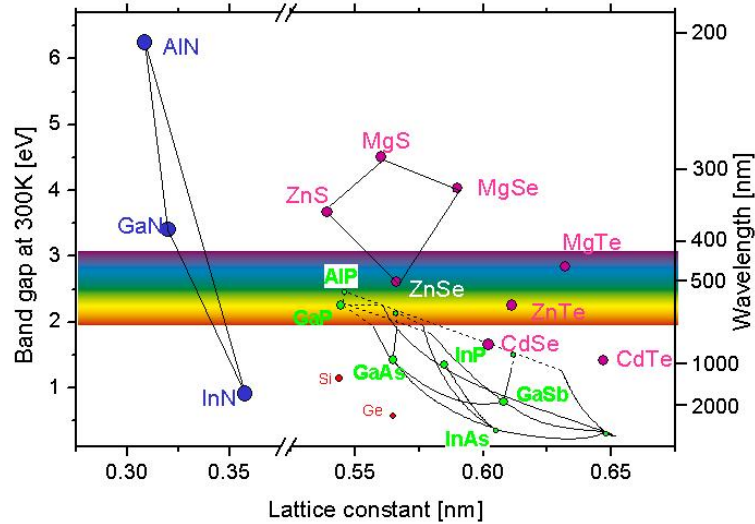


**Figure 1.3** Band gap, emission wavelength and lattice constant of various semiconductor materials, adopted from Ref. [37].

## 1.2 Motivation

Along with the development of THz technology, there are huge demands for THz quasi-optical components such as waveguides, polarizers, wave plates, lens, beam-splitters, modulators and so on. However, the fact that most of natural materials do not response or only response slightly to THz radiations has impeded the development of high-efficient THz components. Meanwhile, subwavelength grating based devices have already been applied in other electromagnetic wave bands and become important components in modern optics and photonics, exhibiting the advantages of small size, high efficiency, design flexibility and easy-to-integrate. It is natural to extend the usage of subwavelength grating to the newly investigated THz waves and exploit the benefits of subwavelength grating to achieve high-efficient THz components. Also, subwavelength metal/semiconductor structures have been discovered to support surface plasmons, enabling novel phenomena in light-matter

interaction and manipulation. In this thesis, I attempt to make a higher performance THz polarizer by using the subwavelength metal grating structure and demonstrate a novel THz modulator based on the plasmonic effect of subwavelength semiconductor gratings.

GaN-based LEDs have been successfully commercialized in areas like solid-state lighting and large-panel display resulting from years of continuous efforts in improving material quality and reducing production cost. Apart from daily lighting, LEDs have more applications, among which data communication and 3D display are two examples. In both cases, the polarization state of the light emitting from LED plays a crucial role. Being small and easy-to-integrate, subwavelength grating is an excellent polarization control component in making polarized light emission from LEDs. Therefore, I am motivated to investigate the integration of subwavelength grating with GaN LED to achieve polarized light emission.

### **1.3 Organization of the Thesis**

In this thesis, the application of subwavelength grating for polarization control in both THz and visible frequency ranges is explored. The thesis is organized as follows:

In Chapter 1, after giving an overview of the background of this work, motivation of the work and organization of the thesis are outlined. Following that, fundamental theories such as finite difference in time-domain, and surface plasmons that are necessary to understand the following chapters are briefly described in Chapter 2. The simulation software used is also introduced.

In Chapter 3, principles of the fabrication and characterization equipment used in the thesis are

explained in details. In particular, the processing parameters adopted and specifications of the equipment are given, which are crucial in fabricating devices with desired properties and analyzing measurement results properly.

Chapter 4 demonstrates an extremely high performance THz polarizer by utilizing bilayer subwavelength grating structure. A subwavelength grating can be used as a linear polarizer, effectively converting unpolarized THz wave into linearly polarized wave. By utilizing the bilayer subwavelength structure proposed, the polarizer exhibits outstanding polarization performance, the highest ever reported.

Chapter 5 presents the experimental results of an optically tunable subwavelength InSb grating in THz frequency range. By tuning the material property of InSb by external lasers, the plasmonic response of the InSb grating can be actively tuned. The carrier lifetime study indicates a potentially high-speed THz modulator based these tunable plasmonic responses.

Chapter 6 shows the experimental results of a polarized GaN LED by integrating conventional LED with Al subwavelength grating, an application of subwavelength grating in the visible range. By fabricating Al subwavelength grating directly on top of the conventional LED chip, light emitting from the LED becomes polarized. Simulation results on the effects of different grating parameters and fabrication steps are described in detail. Characterization results on conventional GaN LED, subwavelength grating polarizer in visible range and polarized LED by integrating them together are shown. Finally, a summary of the thesis and possible future works are given in Chapter 7.

## **Chapter 2 Simulation and Theory**

### **2.1 Introduction**

In this chapter, the simulation technique and theoretical background knowledge are described. Firstly, the theory of finite-difference in time-domain (FDTD) method is explained. Next, the Lumerical<sup>®</sup> FDTD software used to implement the numerical study is introduced. In particular, specific conditions and parameters for simulation of 2D grating structures are discussed. Finally, surface plasmon theory is provided for better understanding of Chapter 5.

### **2.2 Simulation**

#### **2.2.1 Finite-Difference Time-Domain Method**

The finite-difference time-domain (FDTD) method is a state-of-the-art method for solving Maxwell's equations in complex geometries. Being a direct time and space solution, it offers the user a unique insight into all types of problems in electromagnetics and photonics. In addition, FDTD can also obtain the frequency solution by exploiting Fourier transforms, thus a full range of useful quantities can be calculated, such as the complex Poynting vector and the transmission/reflection of light.

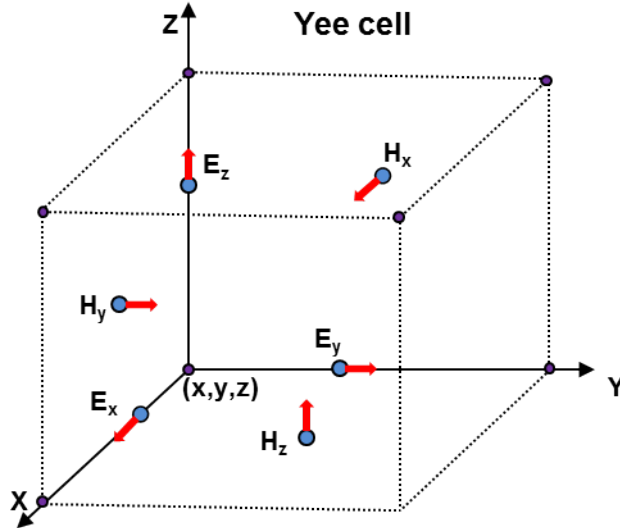


**Figure 2.1** Yee lattice for FDTD calculation.

FDTD solves Maxwell's curl equations in non-magnetic materials:

$$\begin{aligned}
 \frac{\partial \vec{D}}{\partial t} &= \nabla \times \vec{H} \\
 \vec{D}(\omega) &= \varepsilon_0 \varepsilon_r(\omega) \vec{E}(\omega) \\
 \frac{\partial \vec{H}}{\partial t} &= -\frac{1}{\mu_0} \nabla \times \vec{E}
 \end{aligned} \tag{2.1}$$

In Cartesian coordinate, the Maxwell's curl equation can be reduced to six scalar differential equations containing six electromagnetic field components:  $E_x$ ,  $E_y$ ,  $E_z$ ,  $H_x$ ,  $H_y$ , and  $H_z$ . One example is:

$$-\mu_0 \frac{\partial H_x}{\partial t} = \frac{\partial E_z}{\partial y} - \frac{\partial E_y}{\partial z} . \tag{2.2}$$

When  $\Delta x$ ,  $\Delta y$  and  $\Delta z$  are spatial discretizations and  $\Delta t$  is a time step, the function  $F(x,y,z,t)$  is discretized as

$$F(x, y, z, t) = F(i\Delta x, j\Delta y, k\Delta z, n\Delta t) = F^n(i, j, k). \tag{2.3}$$



Also the differential equation can be discretized in space and time to finite-difference equation via:

$$\begin{aligned}\frac{\partial F^n(i, j, k)}{\partial x} &= \frac{F^n(i + \frac{1}{2}, j, k) - F^n(i - \frac{1}{2}, j, k)}{\Delta x} + O((\Delta x)^2), \\ \frac{\partial F^n(i, j, k)}{\partial t} &= \frac{F^{n+\frac{1}{2}}(i, j, k) - F^{n-\frac{1}{2}}(i, j, k)}{\Delta t} + O((\Delta t)^2),\end{aligned}\tag{2.4}$$

where central difference center is chosen to minimized the approximation error.

Yee proposed a lattice model of the difference centers for solving Maxwell's equations, as shown in **Figure 2.1**. Take  $H_x$  for example, the spatial difference centers in the x, y, and z directions are respectively found to be  $x = i\Delta x$ ,  $y = (j + \frac{1}{2})\Delta y$  and  $z = (k + \frac{1}{2})\Delta z$ . The time difference center  $t = n\Delta t$ . So equation (2.2) can be discretized to:

$$\begin{aligned}H_x^{n+1/2}(i, j + \frac{1}{2}, k + \frac{1}{2}) &= H_x^{n-1/2}(i, j + \frac{1}{2}, k + \frac{1}{2}) \\ &- \frac{\Delta t}{\mu_0} \left\{ \begin{aligned} &\frac{1}{\Delta y} [E_z^n(i, j + 1, k + \frac{1}{2}) - E_z^n(i, j, k + \frac{1}{2})] \\ &-\frac{1}{\Delta z} [E_y^n(i, j + \frac{1}{2}, k + 1) - E_y^n(i, j + \frac{1}{2}, k)] \end{aligned} \right\}.\end{aligned}\tag{2.5}$$

The other components can be obtained through a similar method. Magnetic fields  $H_\alpha^{n+1/2}$  with the half-integer time step  $(n+1/2)\Delta t$  are calculated by using the electric fields with the integer time step  $n\Delta t$ . Then those fields are used to calculate the electric fields  $E_\alpha^{n+1}$  with the integer time step  $(n+1)\Delta t$ . Repeating these two steps, the time evolution of the electric and magnetic fields are calculated directly.

### 2.2.2 Lumerical FDTD

In this thesis, the FDTD simulations are done by a commercial software Lumerical<sup>®</sup> FDTD [39]. The subwavelength gratings are assumed to be infinitely long along the wire direction, so 2D simulations are adopted. **Figure 2.2** shows the interface of the software. The simulation model contains four parts, i.e. structures, simulation region, sources and monitors. The structures describe the physical shape, dimensions and materials of the device to be investigated. Material properties can be found in the build-in material database or imported through particular models. The simulation region defines the simulation area, time, accuracy and other properties. As the gratings are assumed to repeat infinite times, one unit cell with periodic boundary conditions is calculated in actual simulations. The mesh size is less than 20 nm in all the cases studied throughout this thesis. Care should be taken for metals as they are highly dispersive. Mesh override regions are applied to metal areas to reduce the mesh size to be less than 2 nm. Sources specify the wavelength range and polarization state of the incident light. Normally incident plane waves are used in all the studies. The monitors collect the electromagnetic wave components ( $E$ ,  $H$ ,  $P$ ) in time/frequency domain and calculate the transmission/reflection coefficient. It should be noticed that monitors should be placed at least half wavelength away from the structures to avoid collection of evanescent waves and reduce simulation errors. This is of particular importance for the study of polarizers as the TE transmittance is inherently low, small noise will induce large simulation inaccuracy.

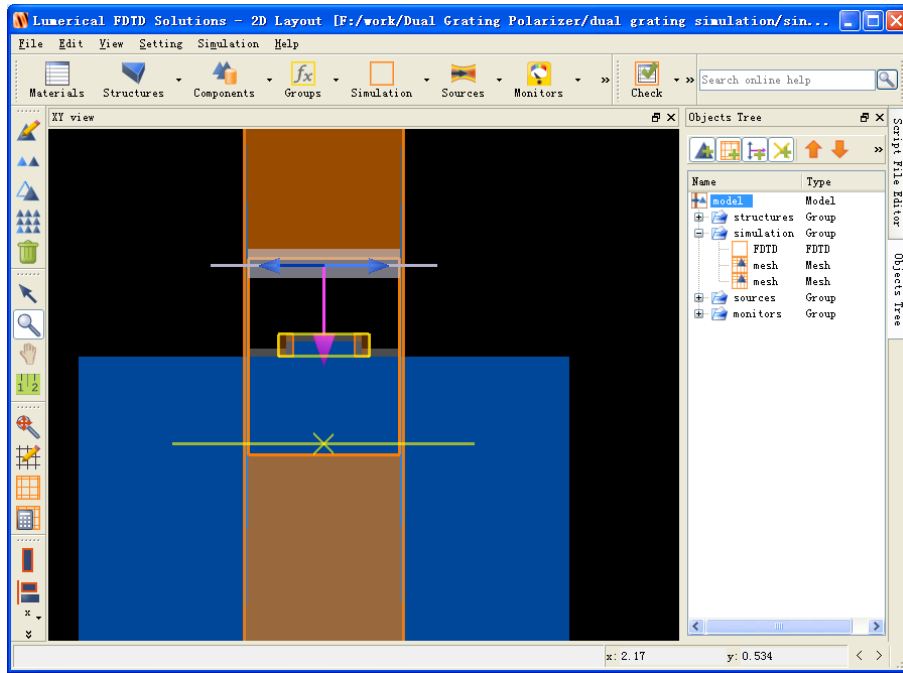


**Figure 2.2** Interface of the Lumerical FDTD software.

### 2.3 Surface plasmon resonances

The advances in techniques, especially the ability to pattern and characterize metals in nanometer scale, have also aroused people's intense interest in surface plasmons (SPs). SPs are basically the coherent electron oscillations at the interface between a metal and dielectric [40]. Energy of the incident light (photons) can be coupled to the SPs, resulting in a hybridized excitation called surface plasmon polaritons (SPP). When the frequencies and wave vectors of photons and SPs match each other, resonance occurs, called surface plasmon resonance (SPR). As the wave vector of SPR is much larger than that of light in vacuum, light can be confined into a region much smaller than the diffraction limit. There has been great interest in the past decade in this emerging field called *plasmonics*.

### 2.3.1 Surface Plasmons Polaritons at the Planar Interface

SPP is essentially an electromagnetic wave bound to and travels along the interface of two medium, typically metal and dielectric. To understand the surface plasmon, it is necessary to know the frequency dependent complex dielectric functions of metals. Therefore we will start with a discussion of the optical properties of metals.

Metals consist of conduction electrons that can move freely. The presence of an electric field  $\vec{E}(\omega)$  causes an electron to displace from its original place by a displacement  $\vec{r}$ , which causes a dipole moment  $\mu = e\vec{r}$ . The cumulative effect of all dipole moments associated with all individual electrons results in a macroscopic polarization  $P = ne\vec{r}$ , where  $n$  is the electron density. Macroscopic polarization is also described as:

$$\vec{P}(\omega) = \varepsilon_0 \chi_e(\omega) \vec{E}(\omega), \quad (2.6)$$

where  $\chi_e(\omega)$  is the susceptibility of metal. Susceptibility is connected to the dielectric function of metal  $\varepsilon(\omega)$  by  $\varepsilon(\omega) = 1 + \chi_e(\omega)$ . Under the force of the external electric field, motion of electrons can be solved by classical mechanics, so  $\vec{r}$ ,  $P(\omega)$ ,  $\chi_e(\omega)$  and  $\varepsilon(\omega)$  can all be calculated.

By taking into account only the motion of free electrons, Drude-Sommerfeld model gives free-electron gas the equation of motion as follows:

$$m^* \frac{\partial^2 \vec{r}}{\partial t^2} + m^* \Gamma \frac{\partial \vec{r}}{\partial t} = eE_0 e^{-i\omega t}, \quad (2.7)$$

where  $m^*$  is the effective mass of free electrons,  $E_0$  and  $\omega$  are the amplitude and angular frequency of the applied electric field, respectively. As only free electrons are considered, this motion equation contains no restoring force. The second term in the left hand side stands for the damping caused by electron scattering. Considering harmonic motion of electrons that  $r(t) = r_0 e^{-i\omega t}$  and solving the above equations yields

$$\varepsilon(\omega) = 1 - \frac{\omega_p^2}{\omega^2 + i\Gamma\omega} = 1 - \frac{\omega_p^2}{\omega^2 + \Gamma^2} + i \frac{\Gamma\omega_p^2}{\omega(\omega^2 + \Gamma^2)}, \quad (2.8)$$

where  $\omega_p = \sqrt{ne^2/(\varepsilon_0 m^*)}$  is the volume plasma frequency. Typically,  $\omega_p$  lies in the ultraviolet spectrum region and  $\Gamma$  is orders smaller than  $\omega_p$ . For example,  $\omega_p$  approximately equals to  $1.5 \times 10^{16}$  rad/s,  $1.4 \times 10^{16}$  rad/s and  $2.2 \times 10^{16}$  rad/s for silver, gold and aluminum, respectively; while  $\Gamma$  is about  $7.7 \times 10^{13}$  rad/s,  $1.1 \times 10^{14}$  rad/s and  $1.1 \times 10^{15}$  rad/s for silver, gold and aluminum, respectively [41]. Therefore, for visible light and electromagnetic waves at lower frequencies, real part of the dielectric constant is negative. The free electrons oscillate  $180^\circ$  out of phase relative to the driving electric field, resulting in the high reflectivity of metals. The imaginary part of the dielectric function describes the energy dissipation resulting from electron scattering.

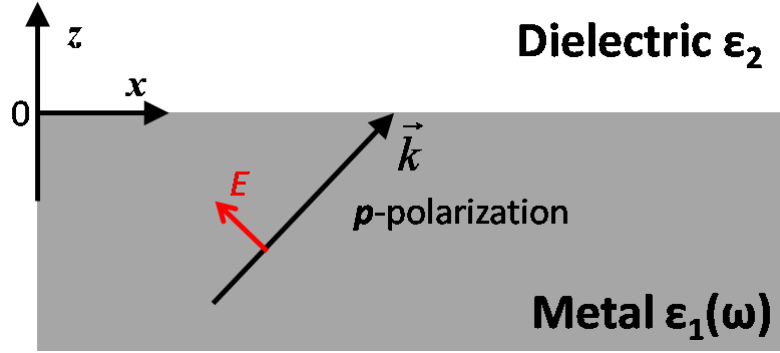


**Figure 2.3** Coordinates of SPP propagation at a planar interface between a metal and a dielectric. *P*-polarized light is also plotted.

It has been verified that Drude-Sommerfeld model describes optical characteristics of metal quite accurately for light at frequencies lower than near infrared. At higher frequencies, the model should be amended by considering bound electrons. It also describes well the optical behavior of semiconductor materials at low frequencies. In this thesis, dielectric function of InSb in THz range is calculated by this model.

Next let's consider a surface wave at the plane interface between a metal ( $z < 0$ ) and a dielectric ( $z > 0$ ), where the metal has a frequency-dependent dielectric function  $\epsilon_1(\omega)$  and the dielectric has a real dielectric constant  $\epsilon_2$ , as shown in **Figure 2.3**. The wave needs to satisfy the wave equation:

$$\nabla \times \nabla \times \vec{E}(r, \omega) - \frac{\omega^2}{c^2} \epsilon_1(\omega) \vec{E}(r, \omega) = 0. \quad (2.9)$$

For *p*-polarized light ( $E_y = 0$ ), we have:

$$\vec{E}_j = \begin{pmatrix} E_{j,x} \\ 0 \\ E_{j,z} \end{pmatrix} \exp(ik_x x + ik_{j,z} z - i\omega t), \quad j = 1, 2, \quad (2.10)$$

and  $k_x = k_{1,x} = k_{2,x}$  as the nature of a surface wave. The subscript  $j$  indicates two different medium, where 1 is for metal and 2 is for dielectric. Substituting (2.10) into (2.9) yields that

$$k_x^2 + k_{j,z}^2 = \varepsilon_j k^2 \quad j = 1, 2. \quad (2.11)$$

Also, exploiting the fact that the displacement fields in both half-spaces have to be source free, i.e.  $\nabla \cdot \vec{D} = 0$ , leads to

$$k_x E_{j,x} + k_{j,z} E_{j,z} = 0, \quad j = 1, 2. \quad (2.12)$$

Continuity requirement for the parallel component of  $\vec{E}$  and the perpendicular component of  $\vec{D}$  leads to another set of equations:

$$\begin{aligned} E_{1,x} - E_{2,x} &= 0, \\ \varepsilon_1 E_{1,z} - \varepsilon_2 E_{2,z} &= 0. \end{aligned} \quad (2.13)$$

Equations (2.12) and (2.13) form a homogeneous system of four equations for four unknown field components. The existence of a solution requires that the respective determinant vanishes, that is

$$\varepsilon_1 k_{2,z} - \varepsilon_2 k_{1,z} = 0. \quad (2.14)$$

Combining equations (2.11) and (2.14) together, we arrive at the dispersion relation for surface wave:

$$k_x^2 = \frac{\varepsilon_1 \varepsilon_2}{\varepsilon_1 + \varepsilon_2} k^2 = \frac{\varepsilon_1 \varepsilon_2}{\varepsilon_1 + \varepsilon_2} \frac{\omega^2}{c^2}. \quad (2.15)$$

The normal component of the wave vector is

$$k_{j,z}^2 = \frac{\varepsilon_j^2}{\varepsilon_1 + \varepsilon_2} k^2, \quad j = 1, 2. \quad (2.16)$$

For visible light, noble metals have negative dielectric constants with absolute exceeding that of dielectric like air or glass, which means  $\varepsilon_1 \varepsilon_2 < 0$  and  $\varepsilon_1 + \varepsilon_2 < 0$ . So  $k_{j,z}$  is purely imaginary and  $k_x$  is real. As a consequence, the wave propagates in  $x$  direction, while its field decays exponentially in  $z$  direction and is spatially confined near the metal surface. This confinement can give rise to strongly enhanced optical near-fields near the interface [42].

It should be noticed that s-polarized light is not considered because its electric field component lies in the plane of the interface and cannot excite charge density waves on the metal surface. Therefore s-polarized light is not suitable for SPP excitation.

### 2.3.2 Localized Surface Plasmon Resonance

It is shown in the description of SPP in the last section that SPs propagating along the interface between metal and dielectric is strongly confined in the  $z$  direction, which is the interface normal direction. Thus it is natural to consider situations where electrons are confined in two or three dimensions, which are in the cases of deep-subwavelength metallic wires or particles. The overall displacement of the electrons with respect to the positively charged lattice leads to a restoring force, which in turn gives rise to a specific particle plasmon resonance. As the separated particle prohibits the propagation of SPs, it is termed as localized surface plasmon resonance (LSPR). In the following, properties of LSPRs will be discussed.

The interaction of a particle of size  $d$  with the electromagnetic field can be analyzed using the



simple *quasi-static approximation* provided that  $d \ll \lambda$ , i.e. the particle is much smaller than the wavelength of light in the surrounding medium. The phase of the harmonically oscillating electromagnetic field is practically constant over the whole particle volume, so the spatial field distribution can be calculated by assuming the simplified problem of a particle in an electrostatic field. It is convenient to start with a simple situation (**Figure 2.4**): a homogeneous, isotropic sphere of radius  $a$  with dielectric function  $\varepsilon(\omega)$  located at the origin in a uniform static electric field  $\vec{E} = E_0 \hat{z}$ . The surrounding medium is isotropic and non-absorbing with dielectric constant  $\varepsilon_d$ .

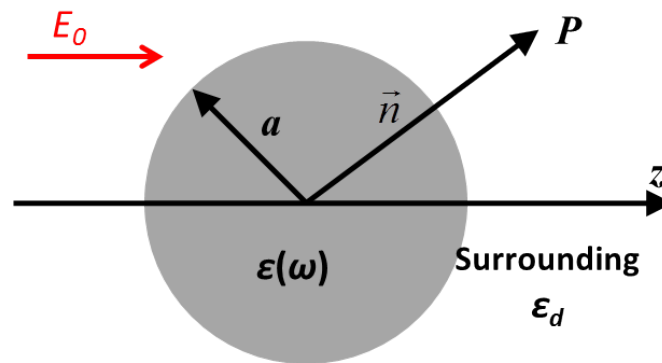


**Figure 2.4** Schematic of a subwavelength sphere placed into an electrostatic field.

By considering the Laplace equation for the potential  $\nabla^2 \Phi = 0$  and applying boundary conditions, we derive that dipole moment  $\vec{p}$  of the dipole induced by electrostatic field in the sphere is

$$\vec{p} = 4\pi\varepsilon_0\varepsilon_d a^3 \frac{\varepsilon(\omega) - \varepsilon_d}{\varepsilon(\omega) + 2\varepsilon_d} \vec{E}_0. \quad (2.16)$$

By defining polarizability  $\alpha$  via  $\vec{p} = \varepsilon_0 \varepsilon_d \alpha \vec{E}_0$ , we get

$$\alpha = 4\pi a^3 \frac{\varepsilon(\omega) - \varepsilon_d}{\varepsilon(\omega) + 2\varepsilon_d}. \quad (2.17)$$

The distribution of electric field inside and outside the sphere is given by

$$\vec{E}_{in} = \frac{3\varepsilon_d}{\varepsilon(\omega) + 2\varepsilon_d} \vec{E}_0, \quad (2.18a)$$

$$\vec{E}_{out} = \vec{E}_0 + \frac{3\vec{n}(\vec{n} \cdot \vec{p}) - \vec{p}}{4\pi\varepsilon_0\varepsilon_d} \frac{1}{r^3}, \quad (2.18b)$$

$\vec{n}$  is the unit vector in the direction of the point P of interest. It is clear that when  $\text{Re}[\varepsilon(\omega)] = -2\varepsilon_d$ , the polarizability experiences a resonant enhancement. Resonance condition is strongly shape-dependent. For instance, electric field inside a subwavelength metallic wire is:

$$\vec{E}_{in} = \frac{2\varepsilon_d}{\varepsilon(\omega) + \varepsilon_d} \vec{E}_0, \quad (2.19)$$

and resonance occurs at  $\text{Re}[\varepsilon] = -\varepsilon_d$ . For an ellipsoid with semiaxes  $a_1 \leq a_2 \leq a_3$ , specified

by  $\frac{x^2}{a_1^2} + \frac{y^2}{a_2^2} + \frac{z^2}{a_3^2} = 1$ , its polarizabilities  $\alpha_i$  ( $i=1, 2, 3$ ) along the principle axes are given by

$$\alpha_i = 4\pi a_1 a_2 a_3 \frac{\varepsilon(\omega) - \varepsilon_d}{3\varepsilon_d + 3L_i(\varepsilon(\omega) - \varepsilon_d)}, \quad (2.20)$$

where  $L_i$  is a geometrical factor. The geometrical factors satisfy  $\sum L_i = 1$  and for a sphere  $L_1 + L_2 + L_3 = 1$ . Real structures can be far more complicated than the above mentioned simple geometries like ideal sphere; however the basic physics of the localized surface

plasmon resonance of a sub-wavelength metallic nanostructure is well described by the special case.

The localized plasmon resonance frequency depends strongly on the dielectric environment. When  $\varepsilon_d$  increases, to satisfy condition  $\varepsilon(\omega) = \varepsilon_d$ , resonance frequency will decrease, as  $\varepsilon(\omega)$  is larger at a longer wavelength. So the resonance frequency red-shifts. As the denominator is not completely zero at resonance ( $\text{Im}[\varepsilon] \neq 0$ ), the resonant strength is limited and bandwidth is increased.

It has been shown that under certain conditions, resonance occurs in polarizability, consequently the electric field both inside and outside the nanostructure is resonantly enhanced. It is this field-enhancement at plasmon resonance on which many of the prominent applications of metal nanoparticles in optical devices rely.

### **2.3.3 THz plasmonics**

The capability of SPPs to confine electromagnetic energy at the interface of a conductor and a dielectric within the subwavelength scale makes them useful for many applications including subwavelength microscopy, non-linear optics, sensing, waveguide and photolithography. However, at frequencies much lower than the plasma frequency, the propagation constants of SPPs approaches the wave vectors in the dielectric materials and SPPs evolve into grazing-incidence light fields extending over a great number of wavelengths into the dielectric space from the interface, called Sommerfeld-Zenneck waves. The field penetration into the

conductor decreases at lower frequencies due to the large permittivity of the metal. In the limiting case of a perfect electrical conductor (PEC), SPPs vanish as appreciable field amplitude inside the metal is essential to provide the non-zero component of the electric field parallel to the surface, which is necessary for the establishment of an oscillating spatial charge distribution. Therefore, many of the advantages of plasmonics such as deep sub-wavelength energy confinement vanish at lower frequencies.

However, there are generally two approaches to extend the concepts of SPPs to the THz frequency range. One approach is called *designer* or *spoof* surface plasmon polaritons, where the geometry instead of the intrinsic materials properties leads to the establishment of a highly confined surface wave. It is known that no electromagnetic field resides inside a PEC, making it impossible to support electromagnetic surface modes and forbidding the existence of SPPs. However, Pendry and co-workers have shown that once the surface of a perfect conductor is periodically corrugated, bound electromagnetic surface waves mimicking SPPs turns out to be sustainable (**Figure 2.5**) [43, 44]. For real metals with finite conductivity, these *designer* or *spoof* SPPs dominate over the delocalized Sommerfeld-Zenneck waves. If the size and spacing of the corrugations is much smaller than the wavelength, the photonic response of the corrugated surface can be described by an effective medium with a plasma-form dielectric function, where the effective plasma frequency is determined by the geometry. This approach has aroused great interest because of the interesting possibility to engineer the dispersion

relation of surface waves at will using a geometry-based approach, allowing tailoring plasmon resonances to particular frequencies.

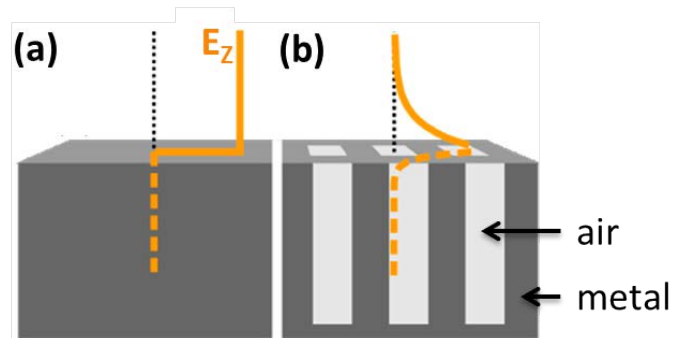


**Figure 2.5** A schematic representation of electric fields associated with a mode propagating along the surface of a metal. (a) At lower frequencies, the metal is almost perfectly conducting and the field ( $E_z$ ) extends far beyond the metal. (b) By corrugating the metal with an array of subwavelength holes, the field is localized near the interface. (Adopted from Ref. [44])

The second approach is to use highly doped semiconductors which exhibit plasma frequencies in the THz range. They offer the potential for sustaining SPPs at THz frequencies. The behavior of highly doped semiconductors mimics that of noble metals in the visible frequencies. For example, SPP can exist at the interface between air and InSb with carrier concentration of  $10^{17} \text{ cm}^{-3}$ . The propagation constant of SPP is larger than the wave vector in InSb ( $\beta > k_0 n$ ). Field localization occurs at the interface, resembling that of metals at visible frequencies, although with a large absorption. Furthermore, semiconductors offer a unique and hugely beneficial advantage over metals: since the surface charge density can be modified by thermal excitation, photocarrier generation or direct carrier injection, plasma frequencies and SPP properties can be tuned within the THz frequency range. Active devices for switching or

modulation applications become possible.

## **2.4 Summary**

In summary, FDTD theory and Lumerical® software used to implement the FDTD simulation have been introduced in this chapter. In addition, important parameters and settings of 2D grating structure simulation used frequently in this thesis are provided. Finally, surface plasmon theory essential to understand Chapter 5 has been discussed.

## **Chapter 3 Fabrication and Characterization Equipment**

### **3.1 Introduction**

This chapter describes processes and equipment that are employed to fabricate subwavelength devices throughout this thesis, including micro- and nano-patterning methods and pattern transfer techniques. Various instruments used to characterize fabrication results and device performance is also described. Working principles, process parameters, equipment models and capabilities are presented in particular.

### **3.2 Fabrication Equipment**

Subwavelength gratings used in this thesis were fabricated by lithography (photolithography or electron-beam lithography), followed by pattern transfer via plasma etching. In this section, the working principle, operating procedure and processing parameters chosen for these steps are described.

#### **3.2.1 Photolithography**

Photolithography is a process to pattern a substrate, which transfers geometric patterns from masks to a light sensitive chemical called “photoresist” on the substrate. **Figure 3.1** shows the schematic of photolithography. Under uniform UV light illumination, chemical properties of the portion of photoresist (underneath transparent parts of the mask) exposed to UV light becomes different from the other part. Depending on which part is soluble to a developer after UV light exposure, photoresist can be categorized into positive tone or negative tone. In the

case of positive tone, photoresist exposed to UV light is dissolved by a developer, leaving photoresist patterns same as the chrome patterns on the mask.

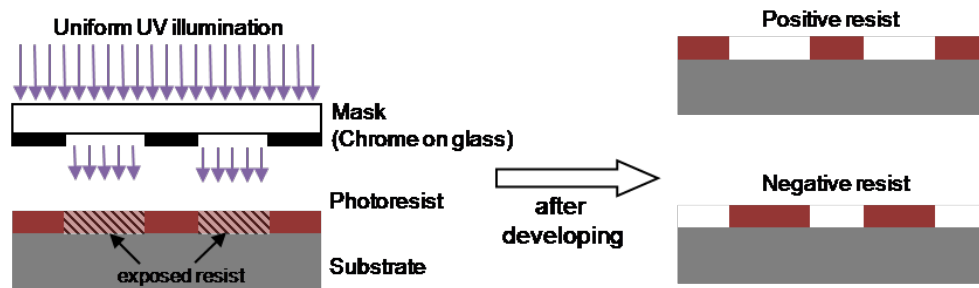


**Figure 3.1** Schematic of photolithography using positive and negative photoresist.

Typical process steps of photolithography are illustrated in **Figure 3.2**. Firstly, the sample surface is cleaned sequentially by acetone, IPA, and DI water with ultrasonic agitation for 5 minutes each round. In some cases, adhesion promoter such as hexamethyldisilazane (HMDS) is coated onto the sample surface (order of monolayer thick) to increase the adhesion between photoresist and sample. The HMDS layer is hydrophobic and can prevent moisture condensation on the sample surface. After sample surface conditioning, photoresist is coated onto the sample by “spin coater”. The thickness of photoresist obtained depends on the type of photoresist used and spin velocity. After that the sample is soft-baked at 95 °C to dense the photoresist by partially evaporating out solvents contained in it. The thickness of photoresist decreases after soft baking. Then the baked sample is exposed under UV light. Alignment between sample and mask is performed if overlay lithography is needed to complete a device.



After developing in photoresist developer, the pattern appears on the photoresist, which can be transfer to the underneath samples by either additive or subtractive pattern transfer techniques. Exposure time and develop time determine the fidelity of obtained photoresist pattern to original one in mask.

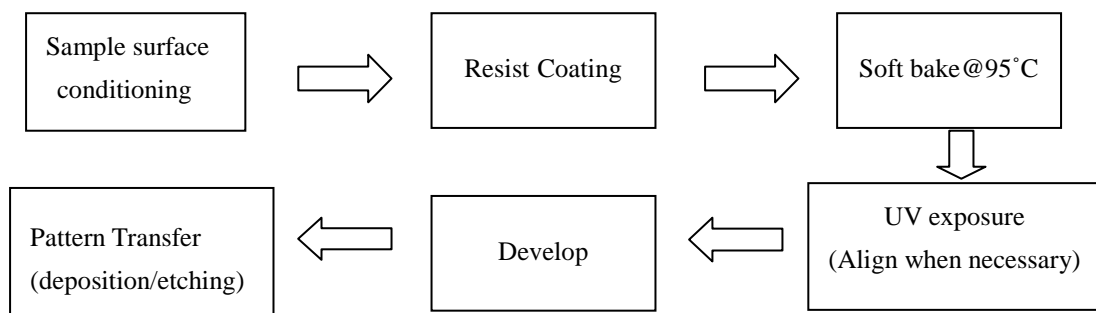


**Figure 3.2** Typical process flow of photolithography.

The photolithography tool used in this work is Karl Suss MA8 mask aligner. The UV light source is filtered from a mercury lamp, centered at 365 nm with an intensity of 8.5 mW/cm<sup>2</sup>. The minimum feature size can be achieved is ~1 μm with good fidelity and reproducibility. Parameters like spin velocity, bake time, temperature, expose and developing time affect the pattern obtained in photoresist. **Table 3.1** lists the photolithography parameters for 3 types of photoresist used in this thesis.

In this work, photolithography is intensely used to fabricate 1D subwavelength grating and GaN LEDs. **Figure 3.3** shows typical images of the photoresist patterns obtained, which will be described in detail in the following chapters.

**Table 3.1** Typical photolithography parameters used in this work.

Photoresist	AZ 5214E	AZ 4330	AZ 4620
Spin Velocity/ Duration	5000 rpm / 30 s	5000 rpm / 30 s	5000 rpm / 30 s
Bake Temp/ Duration	95 °C / 90 s	95 °C / 150 s	95 °C / 150 s
Typical Thickness	1.4 $\mu\text{m}$	3.6 $\mu\text{m}$	6.0 $\mu\text{m}$
Expose Time	4 s	5 s	6 s
Develop Time	12 s	40 ~ 45 s	120 ~ 130 s

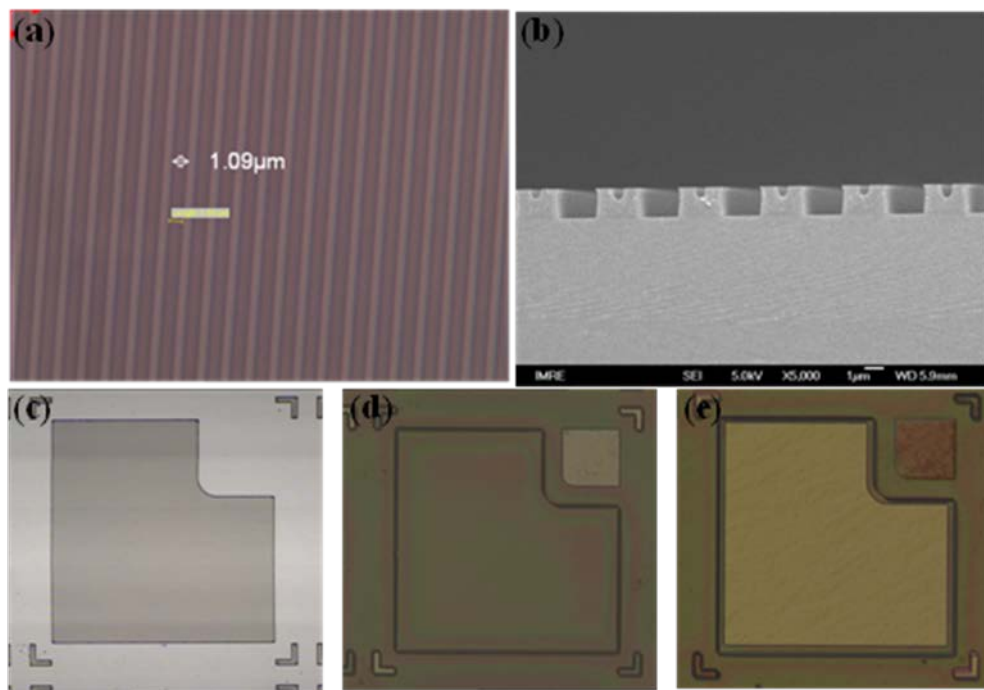


**Figure 3.3** (a) -(b): Images of photoresist (AZ 5214E) grating lines of 1  $\mu\text{m}$  width, viewed from top and side respectively. (c)-(e): Optical microscopic images of photoresist patterns in different steps of GaN LED fabrication.

### **3.2.2 Electron-beam Lithography**

The minimum feature achievable by photolithography is limited by optical diffraction, which is  $\sim 1 \mu\text{m}$  for the equipment used in this thesis. Smaller patterns shown in this work are fabricated by electron-beam lithography (EBL). EBL appears in the early 1960s, almost the same time as optical lithography. It evolved from scanning electron microscopy (SEM, will describe later) as a result of the discovery of an electron-sensitive polymer material, called polymethylmethacrylate (PMMA) [45]. After electrons emitting from the source, they are accelerated by a high voltage (up to 100 kV), which facilitates the focusing by electromagnetic lens. Finally, a fine focused electron beam impinges into a thin resist layer to break the polymer backbone bonds (positive resist) or cross-link the polymer chains (negative resist). By removing exposed (positive resist) or non-exposed (negative resist) regions of the resist, patterns are formed in resist, which can be subsequently transferred to underlying substrates by additive or subtractive methods. Because of the much smaller focus spot enabled by electron optics, EBL demonstrates a much higher resolution capability than photolithography. EBL was already able to pattern features as small as 60 nm in 1970s [46]. Nowadays, state-of-the-art EBL system combined with special e-beam resist materials and processes has enabled the fabrication of structures less than 10 nm [47].

In EBL, as electron beam is deflected electromagnetically to various positions to expose the resist. The patterns are simply determined by CAD design and there is no need of a physical mask. EBL has been widely used in photomask-making, low-volume production of

semiconductor components, as well as the research of science and technology in nano-world.

However, low throughput and high cost are the main limitations of EBL.

The equipment used to perform EBL in this thesis is Elionix ELS-7000 (**Figure 3.4**). In this system, Zirconia/Tungsten ( $ZrO_2/W$ ) is used as the field emission electron source, where  $ZrO_2$  is used to reduce the work function barrier of the tip's surface so that electron emission is enhanced.  $ZrO_2/W$  is chosen for lower energy spread, enhanced brightness, and better stability over long writing time. The maximum acceleration voltage is 100 kV and diameter of focused electron beam can be as small as 1.8 nm. By optimizing parameters, structures with dimension less than 10 nm can be fabricated. In this thesis, this system was used to fabricate nano-gratings with a period of 200 nm. The resist used is ZEP 520A, of which the thickness can be adjusted based on dilute strength. For instance, with a spin-coating velocity of 3000 rpm, thickness of undiluted ZEP 520A is ~400 nm, while that for diluted (ZEP 520A: Anisol, 1:1) is ~120 nm. After optimization, diluted resist (1:1) and dosage of  $280 \mu C/cm^2$  are used throughout the grating structures fabrication by EBL in this thesis. **Figure 3.5** shows two typical resist lines obtained in this work by EBL.



**Figure 3.4** Elionix ELS-7000 e-beam lithography system.

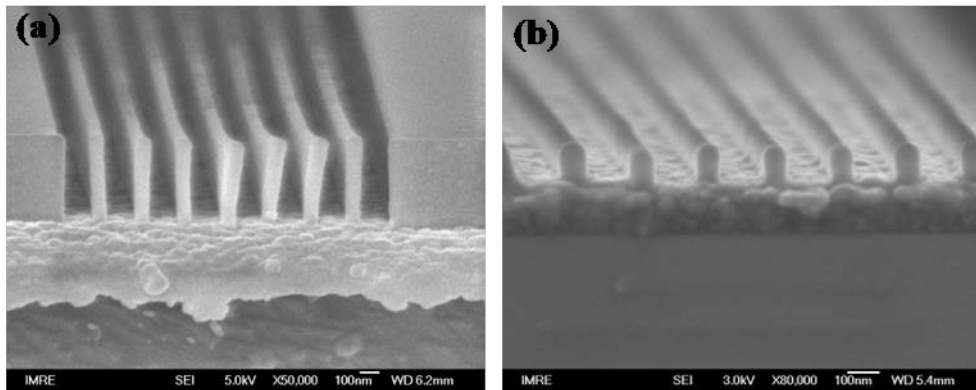


**Figure 3.5** 200 nm period grating on ZEP 520A with different dilute strength. (a) undiluted; (b) 1:1 diluted with Anisol.

### 3.2.3 Reactive Ion Etching

Reactive ion etching (RIE) is a kind of subtractive method for transferring patterns from photoresist to underlying layers. It is a dry etching method using reactive ion plasma to remove materials, possessing the advantage of fine controllability when compared to wet chemical etching.

In the parallel plate RIE system used in this work, plasma is generated between the parallel plates located at a low pressure chamber, from gas molecules or atoms. By connecting the

plates with radio frequency (RF) alternating voltage (13.56 MHz), a strongly oscillating electromagnetic field forms between the parallel plates, which would strip electrons from some of the gas molecules/atoms and turn them into plasma, a medium contains positive ions and negative electrons. Under a proper bias voltage, positive ions will accelerate towards one electrode, where the sample is located. The bombardment by positive ions will change the surface properties of the sample, promoting chemical reactions between surface material and neutral gas radicals. The ions can also etch some materials by physical sputtering. After chemical reaction, the volatile products are brought out of the chamber by gas flow. Compared to wet chemical etching, RIE is an anisotropic etching benefiting from the vertical bombardment of ions. In some cases, side-wall etching inhibitor is added to enhance vertical etching. Besides the parallel plate RIE, other types also exist, including inductively coupled plasma (ICP) RIE. In ICP, the plasma energy is supplied by electric current which are provided by time-varying magnetic fields. It can increase the plasma density and uniformity. By using ICP, it is possible to control the plasma density and bombardment energy independently.

RIE etching result depends strongly on process parameters, such as gas type, pressure, gas flow, and RF power. The gas needs to fulfill two conditions: be reactive with the material intended to remove and produces a volatile product that can be taken out of the chamber. Gas flow, pressure and RF power will determine the plasma density and etching rate.

**Table 3.2** lists the detailed parameters used for etching the materials in this thesis. RIE

system used in this work is Oxford Plasmalab 80 Plus and ICP used is Unaxis SLR-7710-8R.

**Table 3.2** Etching parameters for several materials used in this thesis.

Etch Material	Gas flow (sccm)	Pressure (mTorr)	Temperature	RF power (W)	ICP power (W)
GaN/InSb	BCl <sub>3</sub> 20 Cl <sub>2</sub> 10	5	6°C	200	500
SiO <sub>2</sub>	CHF <sub>3</sub> 25 Ar 25	30	N.A.	150	N.A.
Al	BCl <sub>3</sub> 30 Cl <sub>2</sub> 40	5	20°C	200	500

### 3.2.4 Deep Reactive Ion Etching

Deep reactive ion etching (DRIE) is a highly anisotropic Si etching process. In this thesis, DRIE is used to etch deep trenches in Si with Bosch process. Bosch process contains cycles of two fundamental steps of etching and passivation. The first step is a standard RIE etch. SF<sub>6</sub> ions attack the wafer from nearly vertical direction and react with Si isotropically. After a short duration (several seconds) of isotropic etching, a chemically inert passivation layer of C<sub>4</sub>F<sub>8</sub> is deposited. This passivation layer falls on both the bottom and sidewall of the etch opening. In the following etching round, ion bombardment will occur vertically and only removes the passivation layer deposited on the bottom of the opening, enabling the vertical etching. However, sidewall etching will be inhibited by the inert passivation layer. By alternating the two steps, high aspect ratio structures with steep sidewall can be achieved. The DRIE system

used in this work is Oxford Plasmalab ICP 180. **Figure 3.6** shows a Si grating fabricated using the Bosch process with photoresist unstripped, which is an intermediate step of fabricating the THz polarizer used in Chapter 4. The undulating sidewall is a typical feature of the Bosch process.

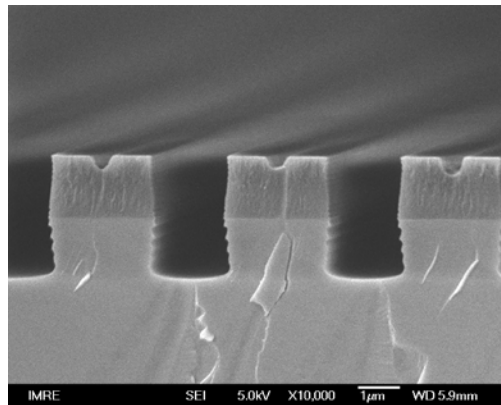


**Figure 3.6** A Si grating obtained in this work after DRIE with photoresist unstripped.

### 3.3 Characterization Equipment

#### 3.3.1 Scanning Electron Microscope

Developed in the early 1950s', scanning electron microscope (SEM) is a kind of electron microscope that obtain image of a sample surface by scanning it with a focused beam of electron. As the wavelength of electron can be adjusted to be very small, the resolution of SEM is much higher than an optical microscope. Modern SEM can achieve a resolution better than 1 nanometer. Basic working principle of SEM is shown in

**Figure 3.7.** At the top of the microscopy, a beam of electrons is produced by an electron gun.



When the electron beam follows a vertical path through the microscope, it travels through electromagnetic fields and lenses, which focus the beam to the sample. The focused electrons interact with the atoms at the sample surface, producing several signals that can be detected to determine the surface morphology and chemical composition. As shown in **Figure 3.8**, the interaction of electrons with atoms at sample surface will produce signals like secondary electrons, back-scattered electrons, characteristic X-rays, cathodoluminescence, transmitted electrons, etc.

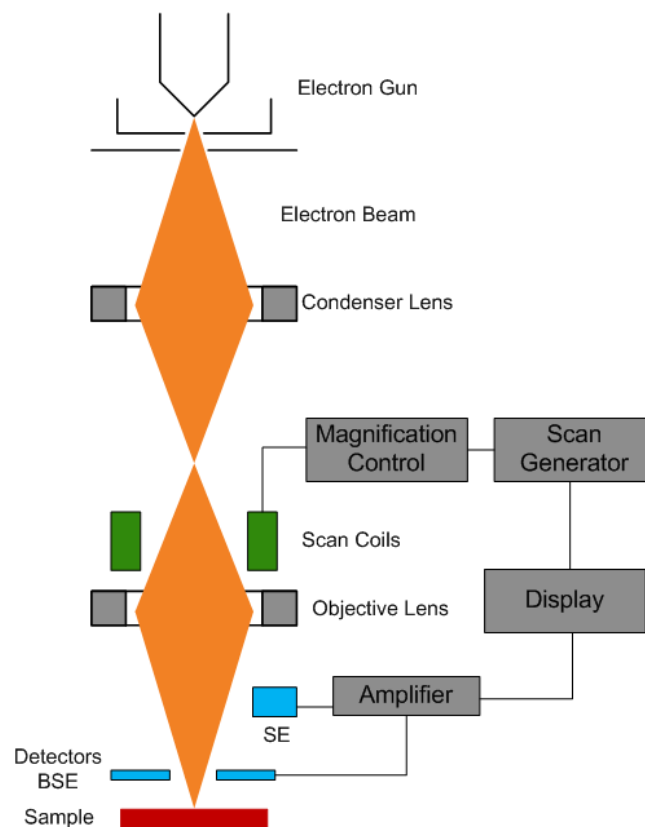


**Figure 3.7** Basic working principle of a SEM.

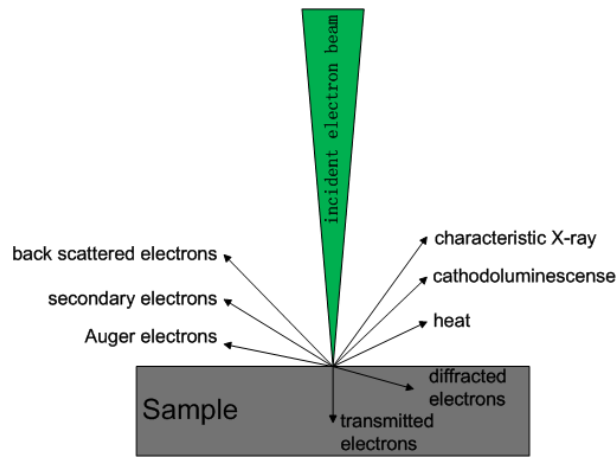


**Figure 3.8** Illustration of signals produced by interaction of electrons with atoms.

Secondary electrons are the most commonly used for imaging. Because the energy of secondary electrons is relatively low ( $< 10$  eV), only the secondary electrons originated from surface atoms can escape the sample and be detected. So secondary electrons give a good description of the surface morphology of samples. As atoms with higher atomic number scatter more electrons in the backward direction, back scattered electrons reveal information of the surface chemical composition. Together with characteristic X-ray, they are often used to detect chemical compositions of surface materials.

In this project, JOEL field emission (FE) SEM 6700 was used to characterize the surface morphology of samples. At an acceleration voltage of 5 kV, the resolution is better than 30 nm. The chamber pressure is better than  $1 \times 10^{-4}$  Torr during imaging. To reduce the charging effect which blurs the images, insulating samples are often covered with a thin layer of Au or Pt by a sputter coater prior to SEM imaging to enhance conductivity.

### 3.3.2 Fourier transform infrared spectroscopy

Fourier transform infrared (FTIR) spectroscopy is a technique that can obtain the infrared spectrum of gases or condensed matters. It is widely used by analytical chemists to elucidate organic compounds, determine the structure of complex molecules and so on. Compared to traditional dispersive infrared spectroscopy, FTIR possesses the advantages of higher speed and throughput. As the word “*FT*” which stands for “Fourier transform” illustrates, Fourier transform is essential to obtain the final spectrum.

The basic working principle is shown schematically in **Figure 3.9**. Broadband light emitted from an infrared light source is collimated and shined to a beamsplitter. Ideally, 50% of the light is transmitted to a fixed mirror and 50% is reflected to a moving mirror. After reflecting by the mirrors, the split light is recombined and directed to samples. After passing through samples, the light intensity is recorded by a detector. Beamsplitter, fixed mirror and moving mirror form a Michelson interferometer. The optical path difference between two branches of Michelson interferometer can be changed by changing position of the moving mirror. At each position, interference between the two waves reflected from mirrors occurs, resulting in an interferogram [48]. Computer processing turns the interferogram into desired spectrum by applying Fourier transform. The resolution of FTIR spectroscopy is determined by the maximum moving distance of the moving mirror. Although early FTIR setup only had a resolution on the order of  $4\text{ cm}^{-1}$ , nowadays a FTIR spectroscopy with  $0.001\text{ cm}^{-1}$  resolution is commercially available.

In FTIR spectroscopy, information of all frequencies is collected simultaneously, so the scan time is greatly reduced. Also, due to the elimination of usage of slits which are commonly adopted in a monochromator, more light coming from the source can be received by the detector, which greatly enhances the signal-to-noise ratio.

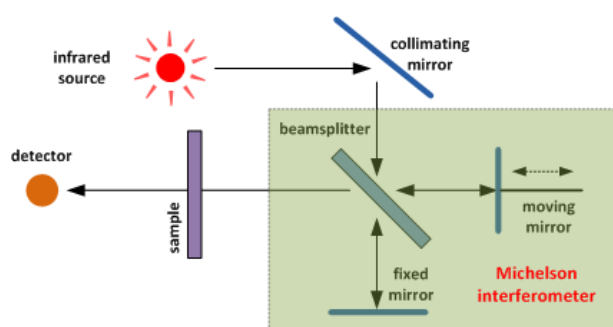


**Figure 3.9** Schematic of Fourier transform infrared spectroscopy.

In this project, FTIR spectroscopy is used to measure the transmission spectrum in THz frequencies (far-infrared). The equipment model used is BRUKER Vertex 80V. Mercury lamp, acting like a black body radiation, is used as THz source and deuterated triglycine sulfate (DTGS) is used as detector. The unique property of DTGS is that its electrical polarization varies with temperature. When illuminated with the infrared radiation, temperature of the DTGS will change, the resulting electrical polarization change will induce a current flow [49]. During scanning, the sample compartment is kept in vacuum to eliminate absorption by water vapor. A resolution of  $2\text{ cm}^{-1}$  is used in all the related measurements in this project.

### 3.3.3 THz time-domain spectroscopy

The development of terahertz science and technology is greatly promoted by the invention of THz time-domain spectroscopy (THz-TDS) in the past decades. In THz-TDS, properties (transmission, reflection or absorption) of samples are characterized by pulses of THz radiation. Compared to FTIR, THz-TDS can provide information of phase change introduced by sample owing to its specific generation and detection scheme. Also, the THz pulse used in THz-TDS is highly linearly polarized, which is beneficial to our characterization of high performance THz polarizers in this thesis.

Basic working principles of THz-TDS and photoconductive THz emitter/detector are schematically shown in **Figure 3.10** and **Figure 3.11**, respectively [30, 50]. Femtosecond pulses generated from the laser source are divided into two parts by a beamsplitter. One part named excitation pulse is focused and shines onto a photoconductive emitter, which is a biased antenna electrodes patterned on a low-temperature-grown GaAs (LT-GaAs) substrate, to generate THz pulse. The other part, called detection pulse, is directed to the detector via a time delay line. THz pulse is emitted as a result of the sudden photo-induced current change in semiconductor materials after femtosecond laser illumination. Emitted THz pulse has a short duration (typically ~2 ps) due to the short carrier lifetime of LT-GaAs. The emitted THz pulse is collimated and focused onto a sample by a pair of off-axis paraboloidal mirrors, and then directed to the photoconductive detector. The detector works similar to the emitter, whereas the antenna is not biased. At the time when THz pulses and laser detection pulses

arrive at the detector simultaneously, laser pulse generates photo-carriers at the surface of semiconductors (called the detector is gated open by the laser pulse), and the electric field of the THz pulse drive generated carriers moving to electrodes, creating a current which is often amplified by an external amplifier. The amplified current is the measured parameter corresponding to the THz field strength. As the carriers in LT-GaAs have an extremely short lifetime, the THz electric field strength is sampled only for an extremely narrow part of the entire electric field profile. By changing the time delay, that is the gating time of the detection laser pulse, electric field strength of the THz pulse at a different time can be measured. Repeating this procedure to cover the full time duration of a THz pulse, the electric field profile in time domain can be portrayed. After performing Fourier transform, transmission properties in frequency domain are obtained.

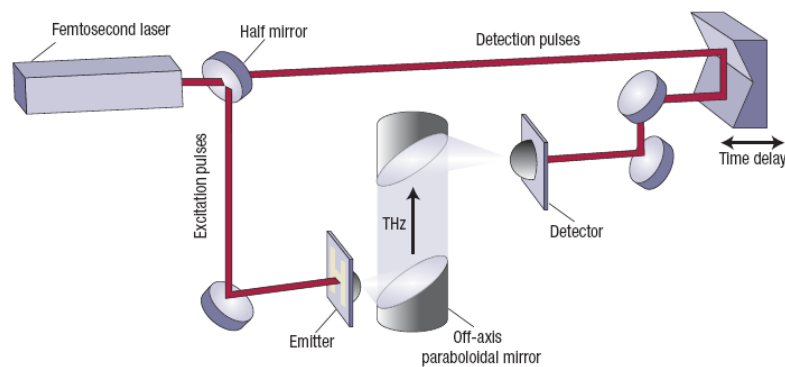


**Figure 3.10** Schematic of the setup for THz-TDS, adopted from Ref. [30].

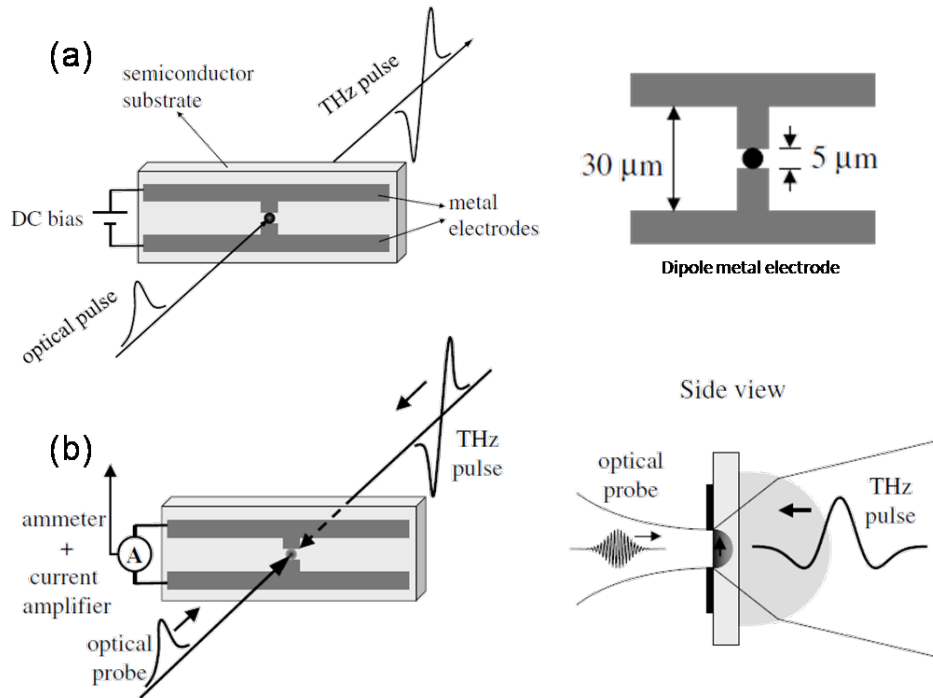


**Figure 3.11** Schematic for (a) photoconductive emitter and (b) photoconductive detector, adopted from Ref. [50].

In this project, transmission spectra of wire-grid THz polarizers were measured by TeraView TPS3000 THz-TDS system with a spectral resolution of 15 GHz. Titanium: sapphire femtosecond pulsed laser was used, emitting ultrashort optical laser pulses ( $\sim 100$  fs) centered at 800 nm with a repetition rate of 76 MHz. The whole setup is purged with dry  $N_2$  to eliminate the water vapor absorption.

### 3.3.4 Optical-pump THz-probe spectroscopy

Optical-pump THz-probe spectroscopy (OPTP, or called *time-resolved THz spectroscopy*) is a technique intensely used to characterize carrier dynamic behaviors in various materials like semiconductors and polymers. Similar to THz-TDS, OPTP is also a time-domain technique,

whereas it contains an optical excitation beam with a time delay line. The optical excitation initiates a change in the far-infrared absorption properties of a material, which is detected on a sub-picosecond timescale.

Basic configuration of OPTP setup used in this project is schematically shown in **Figure 3.12**.

The base is a regeneratively amplified Ti: sapphire laser with outputs 35 fs, 800 nm pulses at a repetition rate of 1 kHz. The output is split into two beams: one for optical pump and one for THz generation and detection. The optical pump beam is frequency-doubled by BBO crystal to 400 nm and shines onto the sample to generate carriers. In our measurement, time delay line (Delay line 1) for THz generation and detection pulses is fixed to a value that the peak of THz pulse in time-domain is detected. While, the time delay (Delay line 2) between the pump and probe beams is changed, so the change in the peak of THz time-domain transmission along with transient behavior of photo-generated carriers is monitored. The time resolution can be achieved is 500 fs.



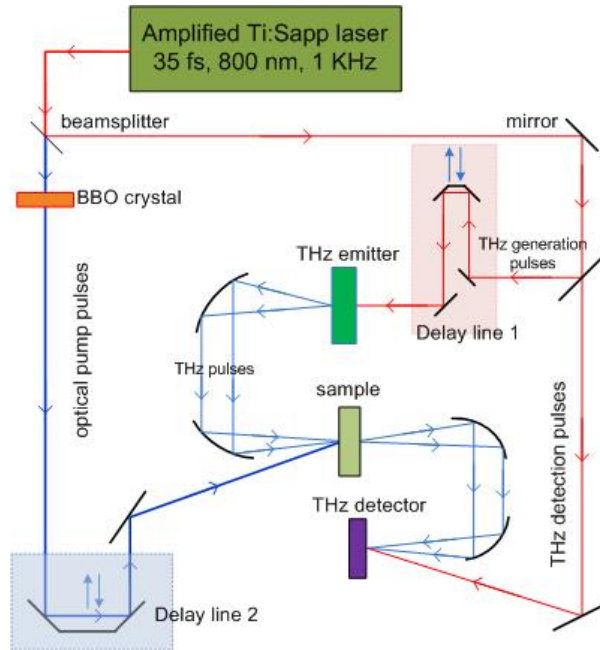


**Figure 3.12** Schematic of OPTP setup used in this project.

For THz generation and detection, different from the photoconductive antennas used in THz-TDS, we used electro-optical rectification and electro-optical sampling effects of non-linear crystal ZnTe (110) to accomplish the task in OPTP. EO rectification is a second-order nonlinear effect that THz waves are generated as a result of a difference-frequency process between the frequency components in fs laser pulses (**Figure 3.13**). EO sampling is based on the Pockels effect, in which the birefringence properties of a material are induced or modified by the existence of an electric field. **Figure 3.14** shows the measuring method adopted in our OPTP setup. When no THz wave shines on the EO crystal, the ellipticity of the probe laser beam is set so that electric fields of both polarizations are equal and the net current from photodiodes assembly is zero. When a THz wave illuminates the EO crystal, the electric field of THz wave changes the birefringence of the material and, thus, the ellipticity of probe laser beam. This change in ellipticity breaks the balance between

two photodiodes and a net current is generated that is proportional to the amplitude of the electric field of the THz wave.

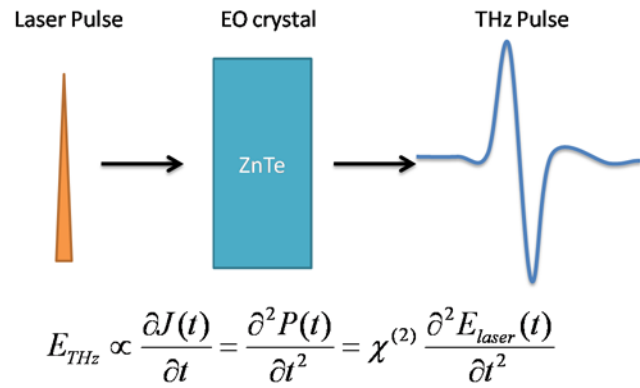


**Figure 3.13** Electro-optical rectification of ZnTe for THz generation.

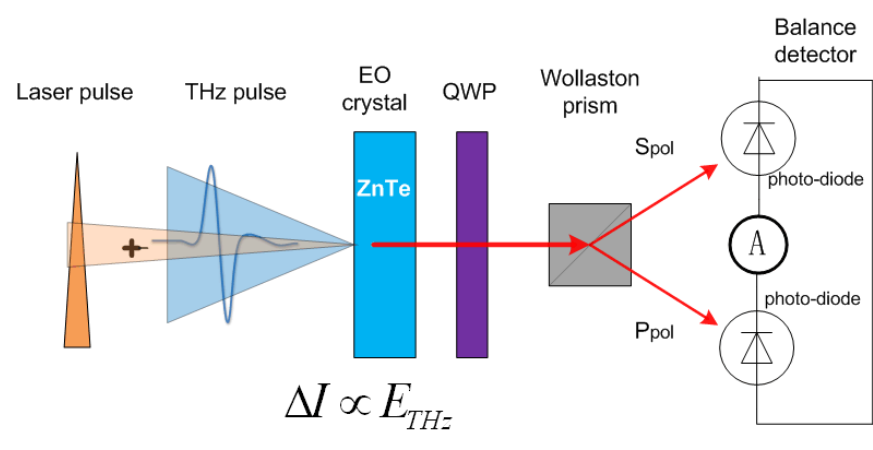


**Figure 3.14** Schematic of electro-optical sampling.

### 3.4 Summary

Equipment that are employed to fabricate subwavelength devices and characterize fabrication

results and device performance are reviewed, i.e. photolithography, e-beam lithography, RIE, SEM, FTIR, THz-TDS, and OPTP.

# Chapter 4 Application of Subwavelength Metallic Grating as a High Performance THz Polarizer

## 4.1 Introduction

In this chapter, we demonstrate an extremely high performance THz polarizer by utilizing bilayer subwavelength grating structure. It is known from Chapter 1 that a subwavelength grating can be used as a linear polarizer, which is applicable in THz frequency range. To improve the performance of subwavelength grating polarizer in THz range, we proposed the usage of bilayer subwavelength structure. The fabricated THz polarizer with bilayer subwavelength structure exhibits outstanding polarization performance, the best ever reported.

### 4.1.1 Linear polarizer

Linear polarizer is a device that can convert unpolarized light to linearly polarized, i.e. after passing through a linear polarizer, the oscillating direction of the electric field of a light will be restricted to one direction. Generally, there are two parameters characterizing the performance of a wire-grid linear polarizer, which are the transmittance of TM transverse magnetic (TM) wave  $T_{TM}$  and extinction ratio (ER). The extinction ratio is defined as  $10 \times \log_{10}(T_{TM}/T_{TE})$  (unit: dB), where  $T_{TE}$  is the transmittance of transverse electric (TE) wave. It is known that light with any polarization can be devolved into two orthogonal polarization states, i.e. TM and TE polarized waves. The electric field of a TM polarized light is perpendicular to the metal wires of a wire-grid linear polarizer, so the TM wave can transmit

through. While for TE wave whose electric field is parallel to the metal wires, the transmission is prohibited. For a high performance linear polarizer, both high  $T_{TM}$  and high ER are desired.

#### **4.1.2 THz polarizer**

Several kinds of THz polarizers have been developed based on different technologies such as liquid crystal polarizer (LCP) [51], Brewster's angle polarizer (BAP) [52], and wire-grid polarizer (WGP) [53-56]. LCPs have a good performance in general but can only work in a narrow frequency band from 0.2 - 1.0 THz. BAP's working principle is based on polarization dependent reflection and transmission of dielectric plates. At Brewster's angle, there is no reflection of  $p$ -polarized light but substantial reflection of  $s$ -polarized light. Therefore, after one interface, part of  $s$ -polarized light is filtered out by reflection in the transmitted light. By adding plates, i.e. interfaces,  $s$ -polarized light will go through multiple-reflections that continuously decreasing its proportion in the transmitted light. After tens of plates, the transmitted light will be highly  $p$ -polarized. It is apparent that BAP has its applicability limited by the specified incident angle (Brewster's angle). Also a polarizer containing tens of plates is often bulky and awkward, making it inconvenient to use and unsuitable for compact systems.

With uniformly spaced metal wires or carbon nanotubes, WGP are widely adopted in THz frequencies. Free-standing metal WGP show low loss but it is challenging to fabricate well-aligned uniformly spaced free-standing metal wires. Recently, a metal WGP with 3  $\mu\text{m}$  period Al grating on Si substrate had been demonstrated with a ER larger than 23 dB in the

frequency range of 0.5 – 3 THz [57]. To achieve higher ER, much smaller period gratings are needed by nano-lithography and fabrication, which are often costly and challenging especially considering the large device size required for THz applications. A double-grating structure has been theoretically suggested by Sun *et al* with the potential to enhance the ER of THz polarizer by utilizing two well-aligned 1- $\mu\text{m}$ -thick Au gratings with a vertical spacing of 25  $\mu\text{m}$  [58]. Even though the double-grating showed high performance numerically, it is extremely challenging to fabricate it in real case. In this chapter, we experimentally demonstrate a bilayer WGP composed of two self-complementarily-aligned gratings, which was fabricated by a one-step etching and metal deposition process. The polarizer was tested by THz-TDS and showed an average ER of 69.9 dB in a broad spectral range from 0.6 – 3 THz and maximum ER of 84.9 dB at 1.67 THz, outperforming all the THz polarizers ever demonstrated. The effects of various parameters of the subwavelength metal grating on the performance of the THz polarizer were analyzed by FDTD simulation. The results have been published in a peer-reviewed paper [59].

## 4.2 Grating Design

**Figure 4.1** shows the schematic diagrams of the single-layer WGP (SWGP) and bilayer WGP (BWGP) formed on Si platform. The SWGP has an Au grating on the surface of Si substrate, while the BWGP has two Au gratings, one at the top of an etched Si grating and the other at the trench of the Si grating. For performance optimization and a better understanding of the WGP performance, firstly we carried out 2D FDTD analysis. Parameters determining the

performance of a WGP include: metal material, substrate material, grating period  $P$ , metal wire width  $w$ , and metal wire thickness  $t$ . For bilayer WGP, one more parameter, i.e. two metal layers spacing  $d$  needs to be considered.

In THz frequency ranges, metals have very high conductivity. The responses of metals to THz waves (dielectric constant of metal) are mainly determined by the behavior of free electrons and can be well described by Drude model. **Figure 4.2** shows the complex permittivity of three different metals (Au, Al and Ag) in 0.6 - 3 THz calculated by Drude model. It should be noted that the real parts of the permittivity are negative, which are almost one order of magnitude smaller than the imaginary parts. Both real and imaginary parts are several orders higher than that of metal in near IR or optical frequency range. The differences between the three metals are not significant, especially for imaginary part. For convenience, Au is chosen as grating material in the following simulations and experiments. Intrinsic Si is chosen as substrate as it is transparent and has very low absorption to THz waves. In the simulations, Si is assumed to be non-dispersive and lossless with a refractive index of 3.4.

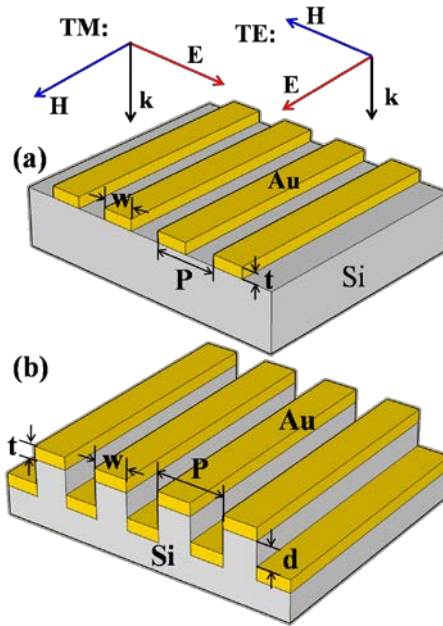


**Figure 4.1** Schematics of (a) SWGP and (b) BWGP. P: wire-grid period; w: metal wire width; t: metal layer thickness; d: metal layer spacing. Normally incident THz radiation with TM or TE polarization is also indicated. H: magnetic field; E: electric field.

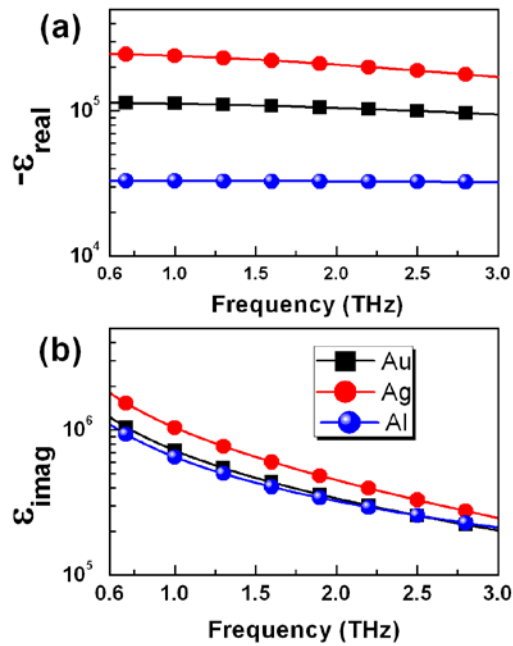


**Figure 4.2** Complex permittivity of three metals (Au, Al and Ag) in THz frequency range.



**Figure 4.3** shows the simulation results of grating period dependent TM transmittance and ER of SWGP in 0.6 – 3 THz. The thickness of Au grating is 200 nm and duty cycle (defined as  $w/P$ ) is 50%. It is noticed that a grating with a smaller period gives a better polarization performance and the difference is greater at higher frequencies. Grating with 0.5  $\mu\text{m}$  period shows a TM transmittance of above 97.7% in the whole frequency range considered, while that for grating with 10  $\mu\text{m}$  period decreases to below 97%. Also, grating with period 0.5  $\mu\text{m}$  has a much higher ER than that of 10  $\mu\text{m}$  grating. At 3 THz, the former outperforms the latter by more than 15dB. Although a smaller period grating (500 nm or smaller) gives a higher performance, it is difficult and more costly to fabricate a large area uniform grating with sub-micron period. In this thesis, the grating period was chosen as 4  $\mu\text{m}$  because it is reasonably small, i.e. much smaller than the interested wavelengths of ~100-500  $\mu\text{m}$  corresponding to frequency of 0.6-3 THz, to render a reasonable high performance and can be easily achieved by conventional micron-processing techniques in large area, considering the large device size needed for THz applications.

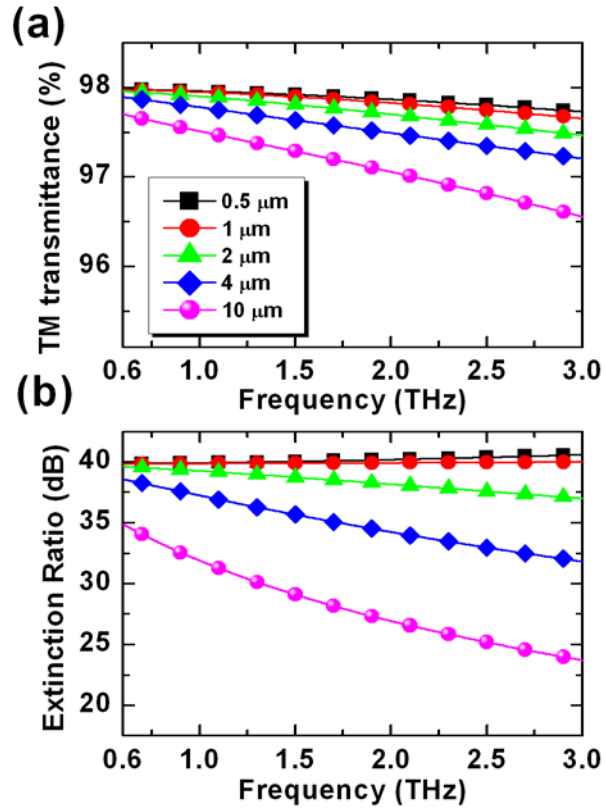


**Figure 4.3** FDTD simulation results of the TM transmittance and ER of SWGPs with different periods.

Next, the effect of metal thickness is investigated by varying Au thickness from 50 nm to 400 nm with period fixed at 4 μm and a duty cycle at 50%. The results are shown in **Figure 4.4**. It is clearly shown that the ER increases by more than 10 dB in the whole spectral range as the metal thickness increases from 50 nm to 400 nm; while the TM transmittances decrease a little. This is because transmitted TE wave through the subwavelength slits is essentially evanescent wave, of which the exponentially decay character decreases TE transmittance and increases ER with metal thickness. This result indicates that increasing the thickness of grating is one approach to enhance the performance of the polarizer. At higher frequencies, the shorter wavelength, the metal thickness appears thicker and thus one would expect a decrease in transmittance.

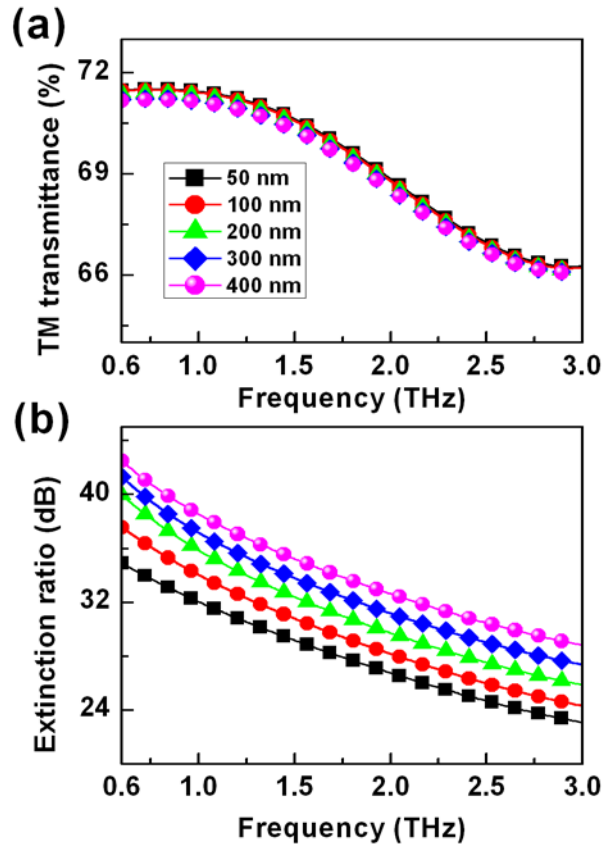


**Figure 4.4** (a) TM transmittance and (b) ER as a function of frequency (0.6 – 3 THz) when the Au thickness is increased from 50 nm to 400 nm. Period and duty cycle are fixed at 4  $\mu\text{m}$  and 50%, respectively.

Next, polarization performance of SWGP and that of BWGP are compared by FDTD analysis.

**Figure 4.5(a)** shows the transmission spectra for both TM and TE polarized waves at normal incidence for metal wire width  $w$  of 2  $\mu\text{m}$ , metal layer thickness  $t$  of 200 nm and two metal layer spacing  $d$  of 1.5  $\mu\text{m}$ , respectively. It shows clearly that the TM transmittances are almost the same for SWGP and BWGP. Nonetheless, there is still a slight drop in TM transmittance of BWGP in higher frequency range, which is assigned to the increased loss caused by the additional metal layer. On the other hand, the TE transmittance of BWGP is two orders of magnitude smaller than that of SWGP. The calculated ER is shown in Figure 4.5(b). As a result

of the dramatic decrease in TE transmittance, the ER of BWGP is about 27 dB higher than that of SWGP. The enhancement in ER by BWGP can be intuitively understood by modeling the BWGP as two SWGPs arranged in tandem [60]. When THz wave with TE polarization reaches the first metal wire-grid layer, it is mostly reflected back, with only a small fraction passing through. This small fraction of TE polarized wave will experience a same process as it reaches the second metal wire-grid layer, with an even smaller fraction transmitted. In this way, the BWGP results in a much decreased TE transmittance and increased ER compared with SWGP. Note that ER decreases with frequency for both BWGP and SWGP due to the smaller wavelength to period ratio at a higher frequency. Considering the significantly increased ER while maintaining the high transmittance for TM waves, BWGP has obvious advantages over SWGP and is a promising candidate for high performance THz polarizers.

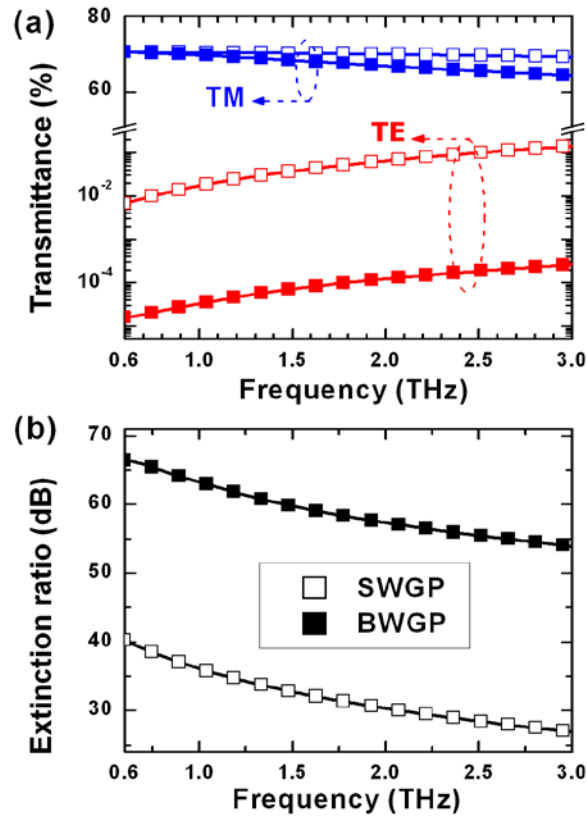


**Figure 4.5** Comparison of polarization performance of SWGP with that of BWGP by FDTD analysis. (a) Frequency dependent TM and TE transmittances. (b) ER as a function of frequency. Lines with solid squares are for BWGP and lines with open square are for SWGP.

The dependences of the BWGP performance on metal thickness  $t$  and two metal layer spacing  $d$  were also investigated. **Figure 4.6(a)** shows the metal thickness dependent transmittance and ER with  $d$  kept at  $1.5 \mu\text{m}$  at 2 THz. It can be seen that both TM and TE transmittance decrease with metal thickness, where the decrease of latter is at a faster pace, leading to a nearly linear increase of ER. This can be explained by treating the subwavelength grooves of grating as an array of “slit waveguide” with a length of  $t$ , cladding by metal strips [61]. For TM incident wave, ohmic loss is increased as it travels through longer slit waveguides due to the non-perfect conductivity of metal claddings. While for the TE case, as the wavelengths of incident waves

are far beyond the cutoff wavelength, the evanescent characters of the electromagnetic fields insides the slits lead to the decreased transmittance as metal thickness increased. In addition, the transmission and ER of BWGP are also affected by the two metal layer spacing, as shown in Figure 4.6(b). The ER decreases significantly (from 80 dB to 55 dB) with the spacing until  $d$  reaches  $\sim 2 \mu\text{m}$ ; after that the ER starts to increase slowly. This is understandable that the strong coupling between two narrow-spaced metal-grid layers results in the additional dissipation of incident waves, as indicated by the simultaneous drop in TM and TE transmittances with narrower spacing. However, as the spacing gets larger, Fabry-Pérot resonant cavity effect starts to dominate, leading to the slow increase in ER within the spacing range we considered.

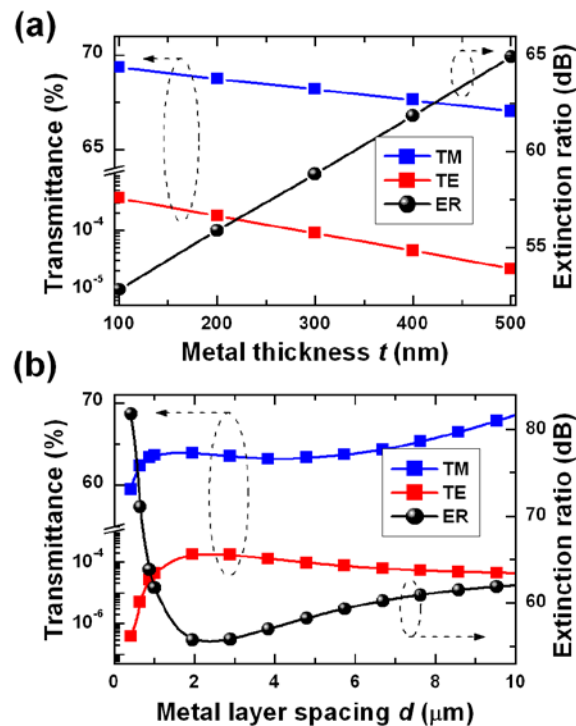


**Figure 4.6** Dependence of the performance of BWGP on (a) metal thickness and (b) two metal layer spacing by FDTD analysis.

### 4.3 Grating Fabrication

The polarizers were fabricated on intrinsic Si (100) wafer, with a resistivity  $>18,000 \Omega \text{ cm}$  and thickness of  $500 \mu\text{m}$ . The intrinsic Si wafer possesses a low absorption loss in THz range, good thermal durability and high robustness. Conventional photolithography was performed to create grating patterns with  $4 \mu\text{m}$  period and 50% duty cycle on photoresist AZ5214E. To fabricate the BWGP, the photoresist pattern was first transferred to the underlying Si substrate by DRIE with Bosch process described in section 3.2.4. After removal of the residual photoresist by acetone, gold was deposited onto the sample by an electron-beam evaporator under a pressure lower than  $2 \times 10^{-6}$  Torr with a rate of  $0.1 \text{ nm/s}$ . Gold atoms are uniformly deposited on both the trenches and ridges of the Si grating, forming the two metal wire-grid layers. The SEM images of the fabricated BWGP viewed from top and cross-section are shown in **Figure 4.7**(a) and (b), respectively. The inset of Figure 4.7(b) shows the enlarged view of the Si ridges and two metal layers. It can be seen clearly that the etched profile of Si by DRIE has an inverse trapezoid shape, which was deliberately controlled by adjusting the gas flow rate and etch-passivation cycle ratio. The inverse trapezoid profile is critical in forming the bi-layer Au grating by effectively preventing gold atoms depositing on the side walls of Si ridges. The undulating sidewall shown in inset is the characteristic result of the Bosch process. For comparison, a SWGP was also fabricated. It was accomplished by gold deposition and lift-off process after the conventional photolithography. To verify the dependence of the behaviors of BWGPs on metal thickness and the two metal layer spacing, four different samples were

fabricated. The dimensions of the four samples A, B, C and D are shown in **Table 4.1**.

**Table 4.1** Dimensions of the four polarizers fabricated.

Sample	t (nm)	d ( $\mu\text{m}$ )
A	200	1.5
B	400	1.5
C	200	5
D	400	5

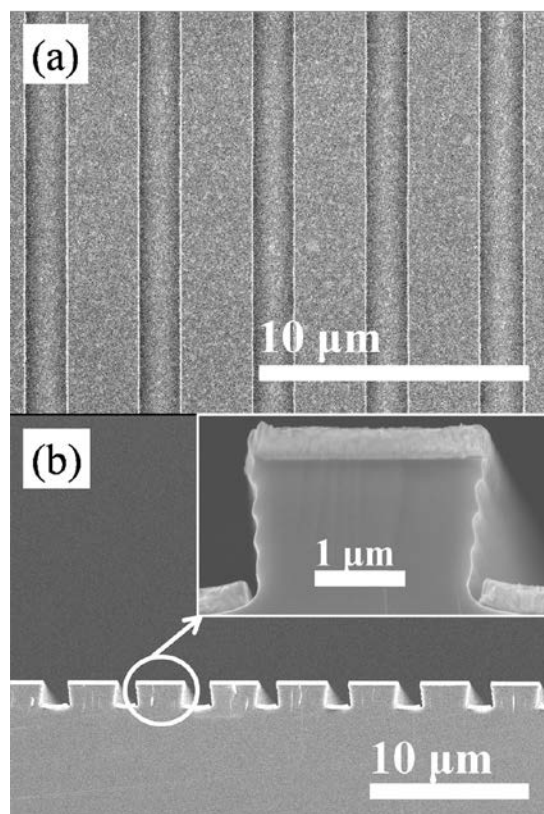


**Figure 4.7** Scanning electron micrographs of the fabricated BWGP. (a) Top view; (b) Cross-section view. Inset: Enlarged view of the Si ridge and two metal layers.



## 4.4 Results and Discussion

We characterized the polarization performance using THz-TDS. The 100 fs optical pulses centered at 800 nm with a repetition rate of 76 MHz from a mode-locked Ti:sapphire laser were focused onto a low-temperature-grown GaAs photoconductive antenna to generate THz pulse. The emitted THz pulse was collimated and focused to the sample by a pair of off-axis paraboloidal mirrors, and then directed to the photoconductive detector, which was gated by the same fs laser pulse. The transmission through a metal hole aperture in N<sub>2</sub> ambient served as reference. The measurement setup was described in detail in section 3.3.3. The transmitted signals for TM and TE polarized waves with normal incidence in time domain are shown in **Figure 4.8**(a) and (b), respectively. The signals of TM polarized waves for different samples cannot be clearly distinguished, showing there is no significant difference in TM transmissions. However, the signals of TE polarized waves of BWGPs are more than ten times smaller than that of SWGP. We should point out specifically that the peak value of TE signal for sample D is only 6, which is close to the noise level of our THz-TDS system (~ 2 in our testing environment), indicating the superior extinction in transmission of TE-polarized THz waves. We performed Fourier transform to extract information about transmittances in frequency domain and calculated the ER as a function of frequency, which are shown in **Figure 4.9**(a) and (b), respectively. It is shown that there is a slight drop in TM transmittances for BWGPs at high frequencies, which is in good agreement with the previous simulation results shown in Figure 4.5(a). The TE transmittances of BWGPs are three orders of magnitude lower than that of

SWGPs. Comparing the ER of sample A with sample B, and that of sample C with sample D, we can conclude that the BWGPs with thicker metal show higher ER, as predicted by the FDTD analysis (Figure 4.6(a)). Comparing the behaviors of sample A with sample C, and sample B with sample D, it also partially verified our simulation results regarding the influence of two metal layer spacing on polarization performance. As shown clearly in Figure 4.9(b), sample D has the best polarization performance among the WGPs we fabricated. The ER is constantly greater than 52 dB in the whole frequency range of 0.6 – 3 THz, or an average ER of 69.9 dB, with the highest ER reaching 84.9 dB at 1.67 THz. This is the highest ER for THz polarizers ever obtained by experiment so far. Also note that at frequencies higher than 1.75 THz, the difference between the ER of different samples is hardly observable due to the poor signal to noise ratio of our THz-TDS system at high frequencies. Since an ideal polarizer should follow Malus's law ( $T(\theta) = T(0) \cos^2\theta$ ), we also measured the transmitted intensity of sample D as a function of polarizer angle  $\theta$  ( $\theta=0^\circ$  represents TM case while  $\theta=90^\circ$  represents TE case) at 1.0 THz, as shown in the inset of Figure 4.8(a). It is clearly seen that the experimental data agrees well with Malus's law, indicating the high quality of our BWGP.

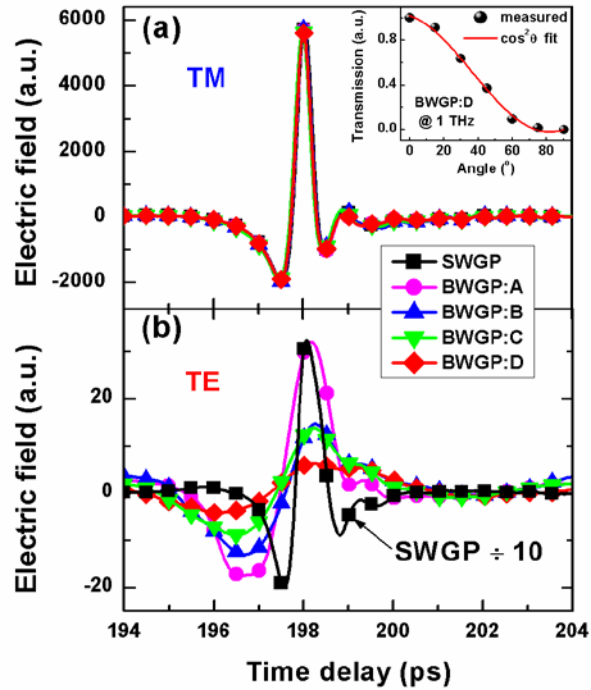


**Figure 4.8** Electric field signals in time domain for (a) TM polarized incident wave and (b) TE polarized incident wave passing through the fabricated WGP. Inset: Normalized transmittance of BWGP as a function of polarizer angle at 1 THz and the corresponding fitting curve to  $\cos^2\theta$ .

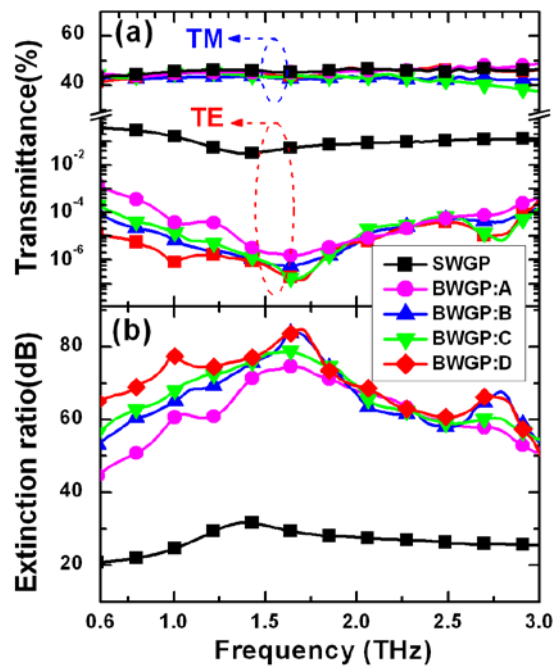


**Figure 4.9** (a) TM and TE transmittance and (b) ER of the WGP as a function of frequency.

It is known that the ER of WGP increases with decreasing grating period or increasing metal thickness [19, 62]. We numerically calculated that for SWGP to achieve an ER above 80 dB in 1.67 THz, a 200 nm period grating with a duty cycle of 1:1 and a metal thickness of around 400 nm is needed. This means that for a nano-metallic single grating structure with an aspect ratio of 4:1 is required, which is an extremely challenging task for nano-patterning and fabrication, especially in a large area for THz application. With BWGP, a high ER of over 80 dB can be easily achieved by conventional micron-fabrication techniques. The BWGP shows a superior advantage in terms of ease of fabrication with high performance. It should also be noted that both BWGP and SWGP have broad frequency bandwidth from 0.6 – 3 THz. Still, this is not the full capability of WGP and our results are limited by the effective spectral range of our THz-TDS system. We are confident to predict that the BWGP can work in an even broader frequency range.

## **4.5 Summary**

In summary, a broadband THz polarizer with an extremely high ER using a bilayer subwavelength metal wire-grid structure is presented in this chapter. Average ER of 69.9 dB in a frequency range of 0.6 – 3 THz and 84.9 dB at 1.67 THz have been observed, the highest values ever demonstrated. The polarization performance is in good agreement with the FDTD analysis. Considering its extremely good performance, ease of fabrication and compatibility with semiconductor process, this BWGP would be widely adopted in various THz applications.

# **Chapter 5 Application of InSb Subwavelength Gratings as an All Optical Terahertz Plasmonic Modulator**

## **5.1 Introduction**

In this chapter, we describe the application of InSb subwavelength grating as a THz modulator due to its directly optical tunable THz plasmonic response. By pumping the InSb subwavelength grating with an external laser, its plasmonic properties are altered and the THz transmission is modulated as a consequence. This chapter is organized as follows: firstly a brief introduction of the properties of InSb as a THz plasmonic material is given. Next the fabrication of the InSb subwavelength grating is elaborated. Lastly, the modulated THz transmittance and the potential modulation speed are experimentally characterized and the results are shown and discussed. Theoretical calculations of the THz transmission of the subwavelength grating based on the fabricated structure and the are also presented and the comparison with the experimental results is given. Further detailed simulations are given to illustrate the effects of structural parameter variations and reveal the full potential of this structure. The results have been published in a peer-reviewed paper [63].

### **5.1.1 InSb as the THz plasmonics Material**

Research on THz electromagnetic radiation has boomed in the past two decades in view of its unique properties and important applications in sensing, imaging, and spectroscopy [30, 32, 64]. However, THz technology suffers a lot from the fact that there is a lack of materials that

naturally response to THz radiations. The recent advancement of plasmonics has brought new approaches for manipulating THz waves. Significant progress has been achieved in the development of THz components exploiting THz plasmonics, such as beam collimated THz quantum cascade laser [65], high efficiency THz photomixer, near field on-chip THz detector [66], THz modulators [34, 67-69], and THz spoof surface plasmon waveguides [70, 71].

As has been discussed in section 2.3.3, semiconductor materials like InSb are excellent candidates for THz plasmonics. Very recently, broadband THz plasmonic absorption in InSb touching disks was demonstrated, which showed consistency with the theoretical predictions of transformation optics for gold nanostructures at visible frequencies [72]. By taking advantage of the fast response time of the optical processes, semiconductor-based optically tunable THz active plasmonics is a very suitable concept for high-speed THz modulation.

InSb is a III-V semiconductor with a very small direct bandgap ( $\sim 0.17$  eV at room temperature) and high electron mobility ( $> 10^4$  cm<sup>2</sup>/V·s). In the THz frequency range, InSb can be modeled as a classic solid-state plasma, with its permittivity given by  $\epsilon_{InSb}(\omega) = \epsilon_{\infty} [1 - \omega_p^2 / (\omega^2 + i\omega\gamma)]$ , where  $n$  is the carrier concentration,  $\gamma$  is the electron collision frequency,  $\epsilon_{\infty}$  is the high-frequency permittivity and  $\omega_p = \sqrt{ne^2 / \epsilon_0 \epsilon_{\infty} m^*}$  is the plasma frequency [73]. At room temperature, the plasma frequency of InSb lies within the THz frequency range. **Figure 5.1** shows the permittivity of InSb with carrier concentration  $2 \times 10^{17}$  cm<sup>-3</sup> in 0 – 3 THz range. It can be seen that permittivity of InSb resembles that of noble metals in the optical frequencies, enabling plasmonic resonances of subwavelength structures with incident THz radiations [74,

75]. As indicated by the above equations, the permittivity and plasma frequency of InSb depends strongly on carrier concentration, which allows the permittivity and consequently plasmonic resonant frequency to be tuned via carrier injection. The mobility and plasma frequency of InSb with different carrier concentrations is listed in **Table 5.1**. It is shown that the plasma frequency blue shifts with increasing carrier concentration. This effect provides an opportunity for modulating InSb based plasmonic devices directly through changes in carrier concentration. The modulation speed will therefore depend on the carrier decay time.

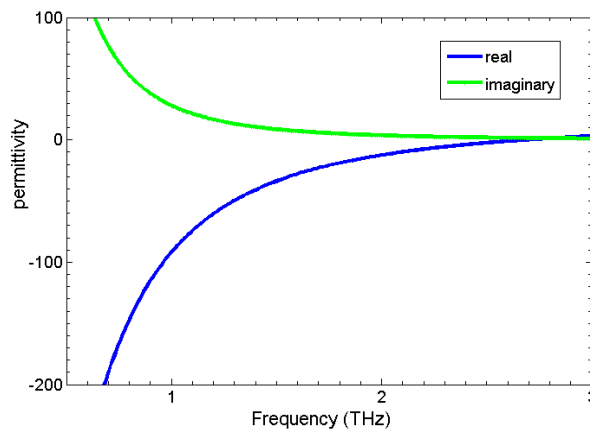


**Figure 5.1** Permittivity of InSb in THz frequency range.

**Table 5.1** Mobility and plasma frequency of InSb with different carrier concentrations [76].

Carrier concentration ( $\text{cm}^{-3}$ )	Mobility ( $\text{cm}^2/\text{V}\cdot\text{s}$ )	Plasma frequency (rad/s)	Plasma frequency (Hz)
$2 \times 10^{16}$	$5.2 \times 10^4$	$1.7 \times 10^{13}$	$2.7 \times 10^{12}$
$5 \times 10^{16}$	$4.5 \times 10^4$	$2.7 \times 10^{13}$	$4.3 \times 10^{12}$
$1 \times 10^{17}$	$3.5 \times 10^4$	$3.8 \times 10^{13}$	$6.1 \times 10^{12}$
$1 \times 10^{18}$	$1.5 \times 10^4$	$1.2 \times 10^{14}$	$1.9 \times 10^{13}$

## 5.2 Subwavelength Grating Design and Fabrication

A 1D subwavelength InSb grating structure was used in our investigation, which was one of the most commonly used structures in plasmonic studies. As we have previously used the one dimensional subwavelength metal grating for high-performance THz polarizer study (Chapter 4), it is convenient for us to use the same mask to fabricate a similar grating structure on InSb to verify the concept of direct optical tuning of plasmonic material itself. The subwavelength InSb grating was fabricated from a 2- $\mu\text{m}$ -thick InSb layer grown by molecular beam epitaxy (MBE) on double side polished semi-insulating (001) GaAs substrates [77]. The average growth rate of InSb layer was  $\sim 1000$  nm/hour and the Sb/In flux ratio was kept at 2. The as-grown InSb has an electron concentration and mobility of  $\sim 2 \times 10^{16}$   $\text{cm}^{-3}$  and  $\sim 52000$   $\text{cm}^2/\text{Vs}$  respectively at room temperature according to Hall measurements. The thickness is chosen as 2  $\mu\text{m}$  to get a stronger plasmonic response from InSb. For example, if the sample thickness is decreased from 2  $\mu\text{m}$  to 0.3  $\mu\text{m}$ , the simulated TM transmittance resonant dip will drop from 51% to 81%, as shown in **Figure 5.2**. Thus, a thicker sample will render a sharper modulation contrast.



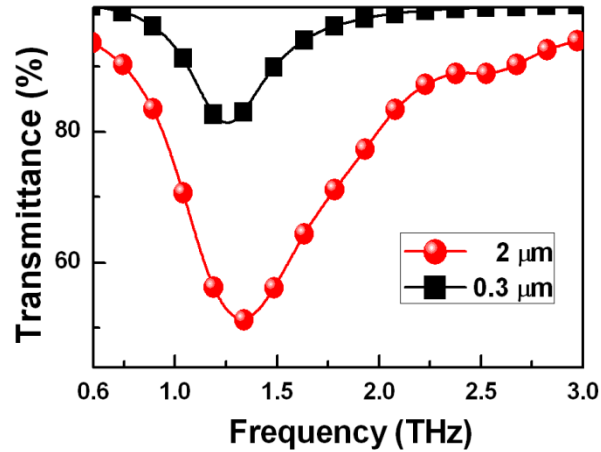


**Figure 5.2** Simulated TM transmittances of InSb gratings with different thicknesses.

To fabricate the InSb subwavelength grating, conventional photolithography was initially performed to create a 4- $\mu\text{m}$ -period grating pattern on photoresist. The photoresist pattern was then transferred to the underlying InSb by ICP etching using  $\text{Cl}_2$  and  $\text{BCl}_3$  gases. The photoresist was finally removed by acetone after the ICP etching. Planar and cross-sectional SEM images of the fabricated InSb grating are shown in **Figure 5.3** (a) and (b), respectively. The electric and magnetic field directions of TM and TE polarizations are also indicated with respect to the grating. As revealed by SEM images, the fabricated InSb strip had a trapezoidal profile. The upper and bottom edges of the trapezoid had lengths of 1.9  $\mu\text{m}$  and 3.6  $\mu\text{m}$ , respectively. A 0.4- $\mu\text{m}$ -gap was formed at the bottom of two adjacent trapezoidal grating strips.

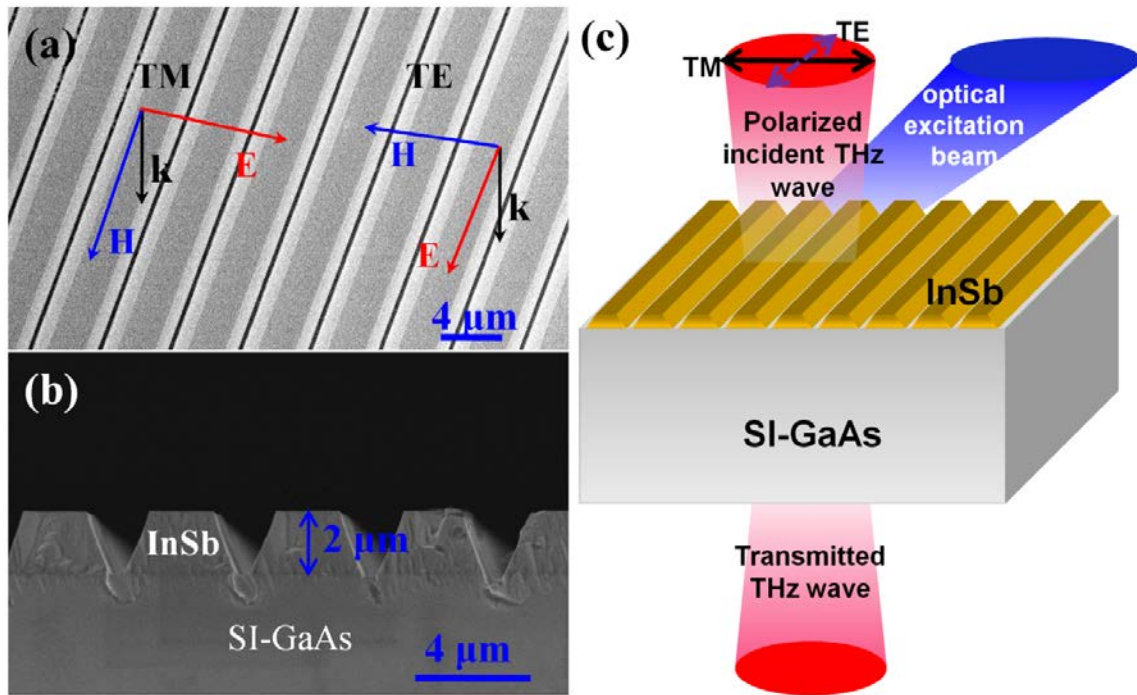


**Figure 5.3** Scanning electron microscope (SEM) images of the fabricated InSb grating viewed from (a) top and (b) cross section. (c) Schematic of the transmission measurement configuration used in FTIR. The 405 nm c.w. laser is shone onto the InSb grating at an incident angle of  $\sim 45^\circ$ . Electric and magnetic field configurations of normally incident TE and TM waves are indicated in (a). H: magnetic field; E: electric field.

The effect of grating period on the THz transmittance was also studied by FDTD simulation based on the fabricated grating shape. As shown in **Figure 5.4**, for TM polarization the resonant frequency decreases and resonance intensity increases as the grating period is increased from 2  $\mu\text{m}$  to 10  $\mu\text{m}$ .

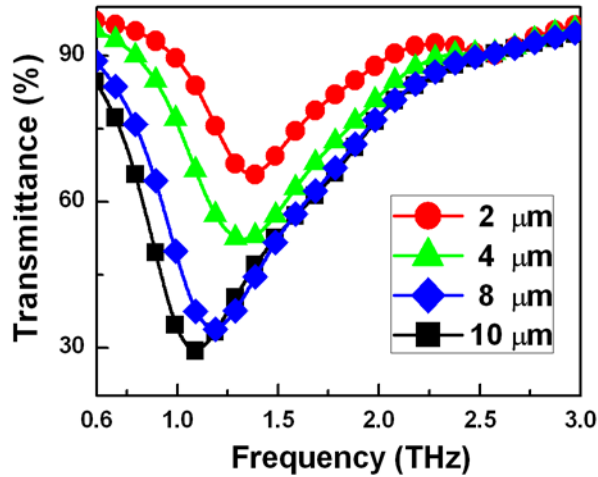


**Figure 5.4** Dependence of TM transmittances on the period of the InSb grating.

### 5.3 Characterization and Discussion

Transmission of THz waves through the subwavelength grating was characterized by Bruker Vertex 80V FTIR with a mercury lamp as THz source and DTGS as THz detector. Transmission through a bare hole aperture was chosen as reference.

As schematically shown in Figure 5.3(c), a polarized incident THz wave was shone normally onto the sample and a laser beam with an incident angle of  $\sim 45^\circ$  was used to optically pump the sample. The transmittance of TM and TE polarized THz waves through an unexcited InSb grating are shown as black curves in **Figure 5.5(a)** and Figure 5.5(b), respectively. The InSb grating under study with a period of  $\sim 2 \mu\text{m}$  is much smaller than wavelength of  $\lambda \sim 100 - 500 \mu\text{m}$  (frequency 0.6 – 3 THz) of the THz signal. For TM polarization, a localized surface plasmon resonance occurs, resulting in a dip in the transmission spectrum with the minimum at  $\sim 1.3$  THz. At frequencies higher than  $\omega_p$ , at which InSb behaves as a dielectric, there is no

energy shunted by LSRP and the transmittance of TM wave was determined mainly by refractive index. For the TE case, as the electric field oscillates along the InSb strip, there is no coupling and hence no surface plasmon resonance effect. The transmittance increases with frequency due to the decrease in effective refractive index.

The subwavelength InSb grating sample was then subjected to a 120 mW, 405 nm wavelength continuous wave semiconductor laser pumping during the transmittance measurement by FTIR. The corresponding transmittance of TM and TE polarized THz waves through laser excited InSb grating are shown in Figure 5.5(a) and Figure 5.5(b), respectively. It is shown clearly that the transmittance minimum of TM wave shifted from 1.3 THz to 1.5 THz after laser excitation. This is because laser excitation generates extra free carriers in InSb and hence increases electron concentration, which in turn results in an increase in the plasma frequency and hence the LSPR frequency. As a consequence, the transmittance at 1.5 THz decreased from 0.6 to 0.32, revealing a change of 46.7%. On the other hand, for TE polarization, the change in transmission is hardly observable.

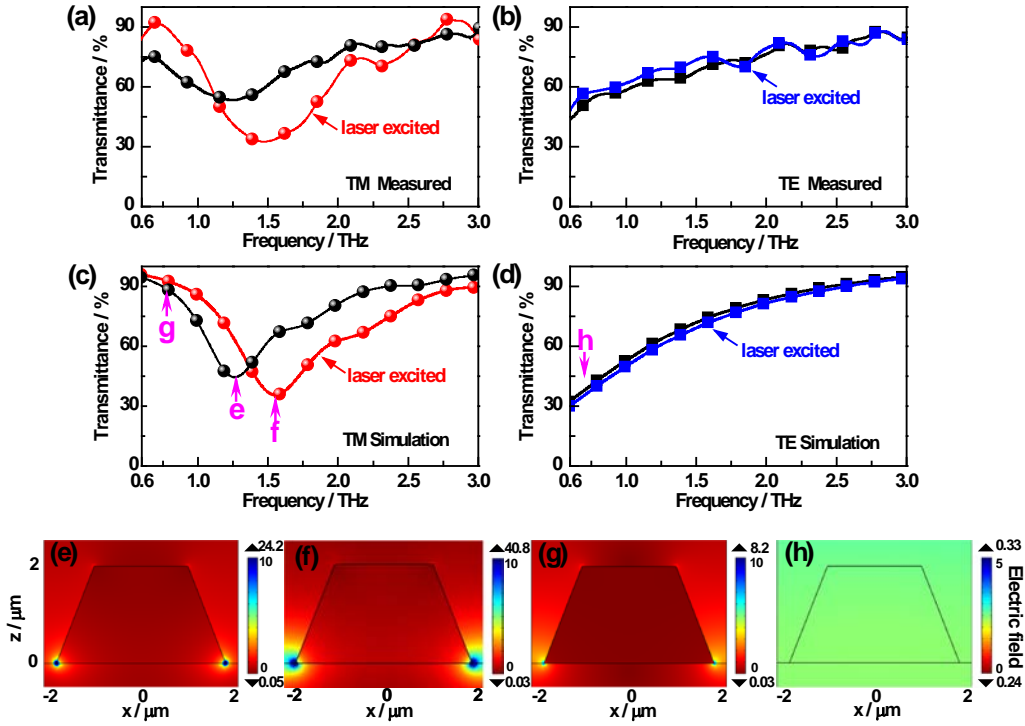


**Figure 5.5** Measured transmittances of (a) TM and (b) TE polarized THz waves through samples without and with laser excitations. (c) and (d) are the corresponding simulated transmittances. (e) ~ (h): Electric field patterns under different conditions calculated by FEM. (e): TM at 1.3 THz without laser excitation; (f): TM at 1.5 THz with laser excitation; (g): TM at 0.7 THz without laser excitation; (h): TE at 0.7 THz without laser excitation. The maximum values of electric fields are indicated at the top of intensity bar.

To fully understand the experimental results, we performed full-wave electromagnetic simulations. The grating specifications and InSb thickness used in the simulation are all based on experimentally measured values. Permittivity of SI-GaAs was taken from literature [78]. The permittivity of InSb was modeled via a Drude model, with electron concentration dependent mobility [76]. The situation under laser excitation is considered as follows. Light with different wavelengths has different penetration depths into semiconductor materials. As the photon energy is higher above the bandgap of semiconductor, the absorption becomes stronger and the penetration depth becomes smaller. At 3.1 eV (~400 nm), InSb has optical

constants of  $n = 3.419$ ,  $k = 2.015$  and absorption coefficient  $\alpha = 633.2 \times 10^3 \text{ cm}^{-1}$  [79, 80]. Therefore the penetration depth (defined as the distance over which the light intensity is attenuated by a factor of  $e^{-1}$ ) is given by  $d_p = 1/\alpha = 15.8 \text{ nm}$ . Also it is calculated that penetration depth at 413 nm is 16.5 nm. Then it can be estimated that penetration depth  $d_p$  at 405 nm is  $\sim 16 \text{ nm}$ . The diffusion of photoexcited carriers should also be considered. Diffusion length  $L_d$  is given by  $L_d = \sqrt{\mu\tau(kT/q)}$ . At 300 K, by substituting the value of electron mobility  $\mu = 52000 \text{ cm}^2/\text{Vs}$  and  $\tau = 1.2 \text{ ns}$ ,  $L_d$  is calculated to be  $12.7 \text{ }\mu\text{m}$ . As the diffusion length is much larger than the thickness of grating used in the experiment ( $12.7 \gg 2$ ), it is reasonable to assume a uniform carrier concentration in the whole InSb grating layer under laser excitation. Assuming the laser intensity in InSb across the penetration depth is uniform and substituting the value of laser spot area of  $2.25 \times 10^{-2} \text{ cm}^2$  and  $\tau = 1.2 \text{ ns}$ , it is calculated that the electron concentration in the 16 nm-thick InSb layer is  $2.82 \times 10^{16} \text{ cm}^{-3}$ . Under this carrier concentration,  $\omega_p = 8.25 \times 10^{13} \text{ rad/s}$  and  $\gamma = 2.56 \times 10^{12} \text{ rad/s}$ .

The simulated transmittances for TM and TE incident waves are shown in Figure 5.5(c) and Figure 5.5(d), respectively. After laser excitation, the resonant frequency is blue shifted to  $\sim 1.58 \text{ THz}$  and the resonance is enhanced in its strength, in good agreement with the experimental results. However the resonance spectrum is broader in the experiments, which can be attributed to additional loss in real structures. Figure 5.5(e) shows the electric field distribution under TM illumination without laser pumping at the resonant frequency (1.3 THz), obtained from one unit cell of the grating. It can be seen that at resonant frequency the electric

field at the sharp corners between InSb and GaAs has very high amplitude (maximum: 24.2), indicating a LSPR. This is different from the lightning rod effect, as shown in Figure 5.6(g) of the unexcited sample at a non-resonant frequency at 0.7 THz (maximum: 8.2). While the field distribution is similar, differences between the LSPR and the lightning rod effect are clearly visible in the absolute field amplitude, in agreement with theoretical prediction [75]. When the subwavelength grating sample was optically excited (Figure 5.5(f)), the field concentration at the corners is much stronger (maximum: 40.8), leading to the decreased TM transmittance at resonance frequency compared to that of unexcited sample. It should be noted that for TE illumination no such field concentration occurs across the whole spectrum studied, even at frequencies below  $\omega_p$  where InSb acts like a metal, as represented in Figure 5.6(h) at 0.7 THz without excitation.

This optically tunable plasmonic response of InSb structures can be used for an all optical modulation, in which the response speed is an important parameter. We characterized the carrier lifetime of the MBE grown InSb material with 400 nm wavelength optical pumping while probed by THz signals using OPTP spectroscopy. In the OPTP system, ~35 fs amplified laser pulses with a center wavelength of 800 nm and a repetition rate of 1 kHz (Coherent.Inc) were splitted into three beams. One beam was frequency-doubled by a BBO crystal and then used to excite the InSb sample. The second beam is used to generate the THz probe pluses and the third beam is used to gate the THz detector. Electric field of the transmitted THz probe beam was measured as a function of the delay time of THz probe beam with respect to the laser

pump beam. It was assumed that the change of carrier concentration in InSb during the short duration of each THz probe pulse (several picoseconds) was negligible. As the transmission of THz probe beam is related to carrier concentrations, the carrier decay time can be extracted.

**Figure 5.6(a)** shows the measured THz signal intensity versus the delay time of THz probe beam at different optical pumping intensities. As can be seen in Figure 5.6(a), the THz signal was steady when the THz probe beam was ahead of the optical pump beam (before 100 ps). However, the transmission of THz probe beam decreased dramatically when it arrived at the sample at the same time with the optical pump beam. After ~21 ps, the THz transmittance drops to its minimum. The free carriers generated by femtosecond laser pulses created a high-carrier-concentration layer in InSb and blocked the transmission of THz pulses, which recovered along with the decay of photoexcited carriers. By applying an exponential curve fitting, the carrier decay times of InSb at different pump laser fluences were extracted and shown in Figure 5.6(b). The fitted lifetime decreased from 1360 ps to 834 ps as the pump laser fluence decreased from 29.3  $\mu\text{J}/\text{cm}^2$  to 0.74  $\mu\text{J}/\text{cm}^2$ , indicating a modulation speed potentially up to ~1.2 GHz. The pump laser fluence dependent carrier lifetime can be attributed to surface defect assisted recombination [81, 82]. At a low carrier concentration, the surface defects act as recombination centers and accelerate free carrier recombination. However, the available trapping sites will be filled up at a higher concentration, leading to a slower recombination process than at lower concentration. It is reasonable to expect a higher modulation speed of InSb subwavelength gratings or other subwavelength structures because of their larger surface



area and more surface states introduced by plasma etching.

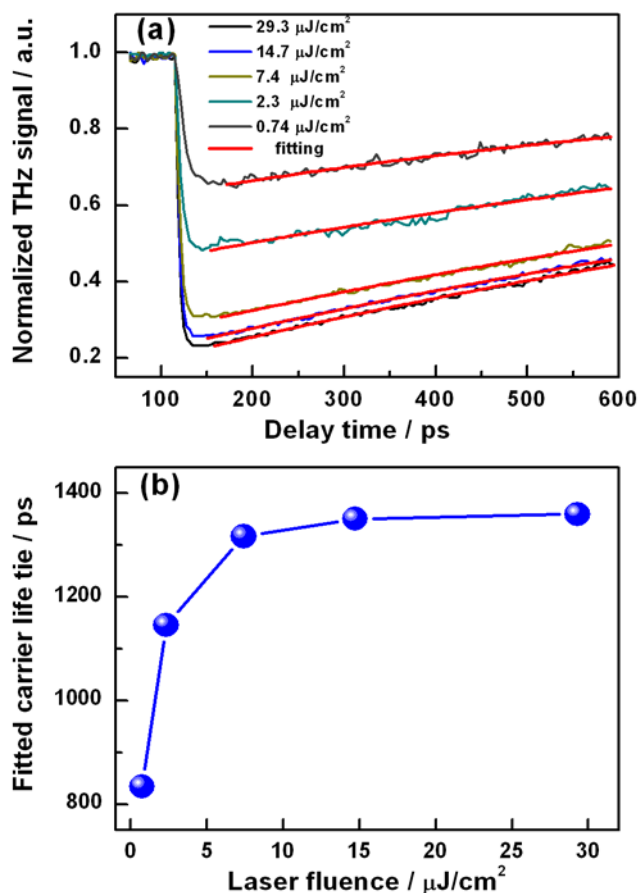


**Figure 5.6** (a) Normalized THz signals as a function of delay time measured by OPTP under different pump laser fluences and the exponential curve fittings. (b) Fitted carrier lifetime as a function of pump laser fluence.

To explore the full potential of this directly tunable THz plasmonic response in the InSb subwavelength grating, we calculated the transmittance at higher carrier concentrations in the whole THz range (0.1 – 10 THz). As a comparison, the transmission spectrum of a Au based subwavelength grating with the same profile and dimension was also examined. As shown in **Figure 5.7(a)**, for TM polarized incident waves, the resonant frequency increased with

increasing carrier concentration, and shifted from 1.3 THz to ~10 THz as the carrier concentration increased from  $2 \times 10^{16} \text{ cm}^{-3}$  to  $1 \times 10^{18} \text{ cm}^{-3}$ . This indicates a great potential for broadband tuning and modulation for InSb based THz plasmonic devices. The frequency of LSPR increased as a result of blue shifting of plasma frequency [83]. It is also apparent that the dips in the transmittance spectra become deeper and broader as the carrier concentration increases. As the plasma frequency increases, the imaginary component of the permittivity at resonance frequency becomes larger, leading to an increase in loss and hence resonance broadening. For TE polarized THz wave, the transmittance decreases with carrier concentration. At  $1 \times 10^{18} \text{ cm}^{-3}$ , the TE transmittance is almost 0, approaching the perfect conductor limit. At this carrier concentration, the InSb grating acts as an effective THz polarizer, i.e. it blocks the TE wave while transmits the TM wave. The fact that the resonance frequency and intensity depend on carrier concentrations and can be modulated by external optical excitation or other means renders great potential and flexibility for applications such as modulators, switches or tunable filters.

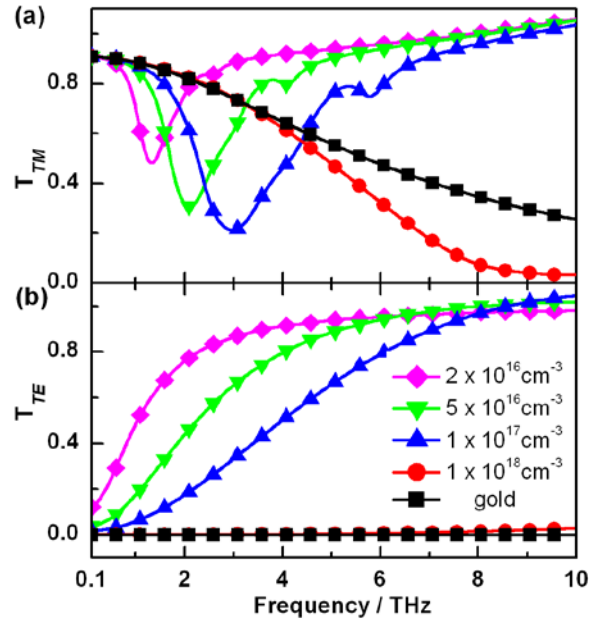


**Figure 5.7** Simulated transmittance of (a) TM and (b) TE polarized waves through InSb gratings with different electron concentrations and a Au grating in the frequency range of 0.1 – 10 THz.

## 5.4 Summary

In summary, we have experimentally demonstrated the tunable THz plasmonic response of InSb subwavelength gratings by optically tuning the carrier concentration. The InSb grating consisted of a 2- $\mu\text{m}$ -thick InSb layer, which was etched to form an arrayed trapezoidal ridges of 1.9  $\mu\text{m}$  width at the top and 3.6  $\mu\text{m}$  at the base. The ridges are separated with a period of 4  $\mu\text{m}$ . The resonance frequency of the structure can be shifted in a broad THz frequency range. At 1.5 THz, the transmittance was reduced from 0.6 to 0.32 when the InSb grating was subjected to the excitation by a 405 nm laser with 120 mW power, a change of 46.7%. At laser pump fluence of 0.74  $\mu\text{J}/\text{cm}^2$ , the excited carrier lifetime was determined to be 834 ps using optical pump-THz probe technique, giving a potentially high-speed THz modulator with a

modulation speed up to 1.2 GHz. Numerical calculation reveals the wide tunability of this modulator in terms of both modulation frequency and depth. The direct all optical tuning and modulation of the plasmonic response of InSb provides much flexibility and new possibilities in future THz component development.

# **Chapter 6 Application of Subwavelength Grating in Visible Range to Realize a Polarized InGaN Light Emitting Diode**

## **6.1 Introduction**

After demonstrating the applications of subwavelength grating in THz range as a high performance polarizer and a high speed modulator, the application of subwavelength grating in the visible range as a linear polarizer to realize a polarized GaN LED will be shown in this chapter. By fabricating Al subwavelength grating directly on top of the conventional LED chip, light emitted from the LED becomes polarized. Simulation results on the effects of different grating parameters and fabrication steps are described in detail. Characterization results on conventional GaN LED, subwavelength grating polarizer in visible range and integrated polarized LED are shown.

### **6.1.1 Polarized LED**

In the past decades, there have been considerable efforts in improving quality and reducing cost of GaN-based LEDs, which have successfully led to their commercialization in various areas such as solid-state lighting, large-panel display and back lighting for LCD, with the advantages of high brightness, low power consumption and long lifetime. At the same time, special-functional LEDs such as LEDs with polarized light emission are also highly desirable for their potentials in making display and imaging systems more compact and robust.

There are several approaches to realize polarized light emission from LEDs. LEDs fabricated

on non-polar or semi-polar GaN substrates are partially polarized, but the expense of non-polar/semi-polar substrates is fairly high. It is known that the light emitting laterally from the side facet of a GaN LED chip is initially polarized due to the strain effect and wave guiding effect of InGaN/GaN quantum wells [84]. In 2007, E. F. Schubert *et al* proposed that by putting a carefully designed polarization enhancement reflector around the LED chip, the polarized light emitting from the side facet can be directed to vertical direction. In this way, the light emitting from the LED surface was polarized with a polarization ratio of 3.5:1 [85]. Incorporating photonic crystal pattern onto the emitting surface of a LED is also an approach to realize polarized LED. In 2009, L. Zhang *et al* from our group suggested that polarized LED can be realized by integrating a subwavelength metal grating with LED. The subwavelength metal grating serves as a polarizer and by putting an Al grating with a period of 150 nm on top of the p-GaN surface, they were able to reach a polarization ratio of 7:1 [86]. Polarized LED with integrated subwavelength metal grating is compact and compatible with semiconductor processing, which shows great advantages especially in applications where space is a big concern.

There is still much room to improve the performance of polarized emission from LEDs. In this chapter, we demonstrated polarized light emission directly from InGaN/GaN multiple quantum well (MQW) blue/green LED by integrating subwavelength metallic grating with the LED chip. Two-dimensional finite-difference in time-domain (FDTD) analysis was performed to fully examine the dependence of subwavelength metallic gratings' polarization behavior on various

grating parameters. The fabrication steps and measurement results are elaborated.

## 6.2 Subwavelength Grating Design

The structure of polarized GaN LED used is schematically shown in **Figure 6.1**. The subwavelength metal grating resides on top of the p-contact area of a LED die, serving as a linear polarizer. Light emitted from the InGaN/GaN quantum well becomes linearly polarized after passing through the metal grating. As mentioned before, grating parameters such as material, period, height, and duty cycle will greatly influence the polarization performance. So the grating parameters were optimized prior to fabrication.

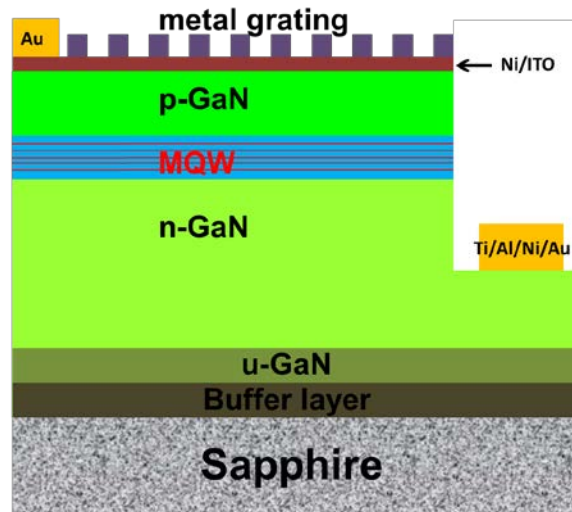


**Figure 6.1** Schematic diagram of the GaN LED integrated with a subwavelength grating.

Light emitted by an InGaN/GaN LED normally falls into the wavelength range of 400 - 600 nm, thus we will focus on this range in the following simulation. The first concern is the choice of

metal. In visible range, the differences between metals are mainly caused by electron inter-band transition and the different plasma frequencies. **Figure 6.2** shows the simulation results of TM transmittance and ER for subwavelength gratings made from three commonly used metals, i.e. Al, Ag and Au. The FDTD simulation scheme is described in Chapter 2. It can be seen clearly that Al has the highest TM transmittance and ER in the whole wavelength range considered. Ag has better performance at longer wavelengths ( $> 520$  nm) than shorter wavelengths. The performance of Au is the poorest. As Al has the highest plasma frequency (in UV range), its metallic character is more obvious in the blue and green region, so the subwavelength Al grating has the best polarization performance. The slightly lower plasma frequency of Ag (in blue region) results in its relatively poorer behavior in the shorter wavelength range. The behavior of Au is hampered by both low plasma frequency and interband transition. Considering its pronounced high performance compared with other candidates, Al is chosen as the material for subwavelength gratings in the following simulations and fabrication.



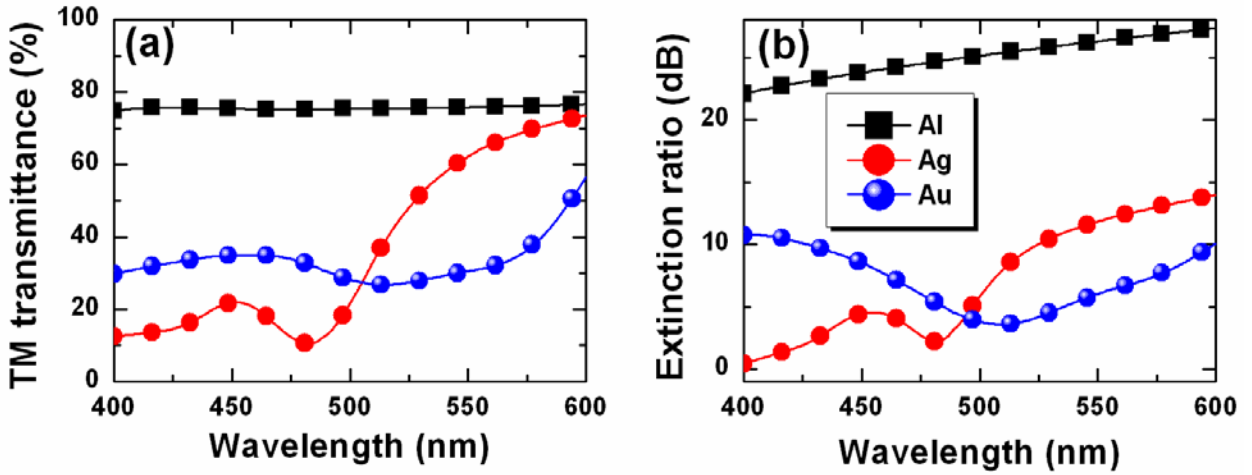


**Figure 6.2** Polarization performances of subwavelength gratings made by different metals, Al, Ag and Au.

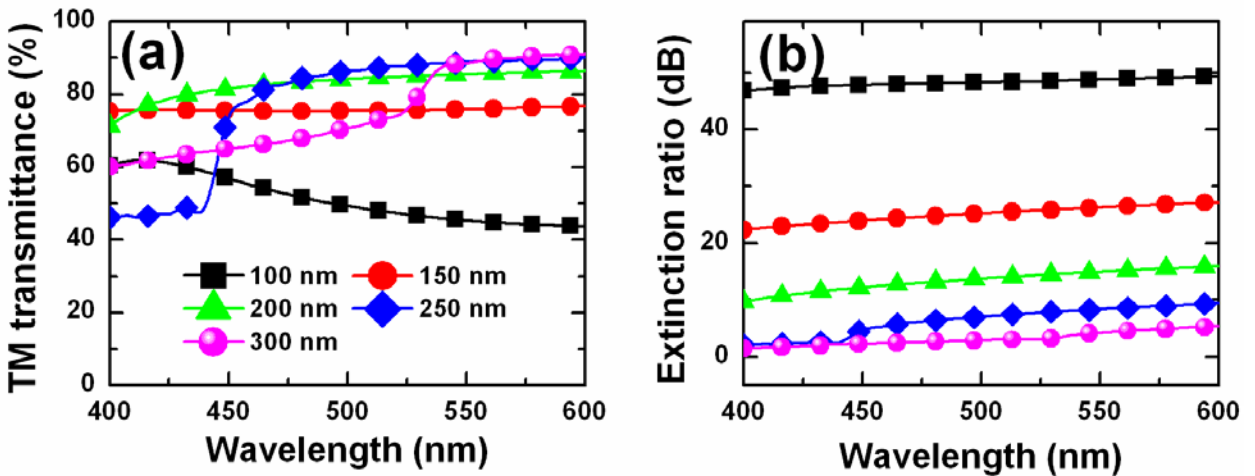


**Figure 6.3** Dependence of polarization performance on grating period.

Next, the effect of grating period is investigated. **Figure 6.3** shows the simulation results for gratings with different periods ranging from 100 nm to 300 nm at a step of 50 nm, with duty cycle kept at 50%. It shows that at wavelengths larger than 530 nm, the TM transmittance decreases with shrinking grating period. The more complicated behavior at a shorter

wavelength is probably caused by the excitation of surface plasmons. There is a transition from low to high TM transmittance and it moves towards longer wavelength as the grating period increases. On the other hand, a smaller grating period renders a higher ER. The ER of 100 nm period grating exceeds 40 dB in the whole wavelength range. Thus, ER and TM transmittance are a trade-off. By considering the overall performance and fabrication simplicity, the grating period was chosen to be 200 nm for fabrication.

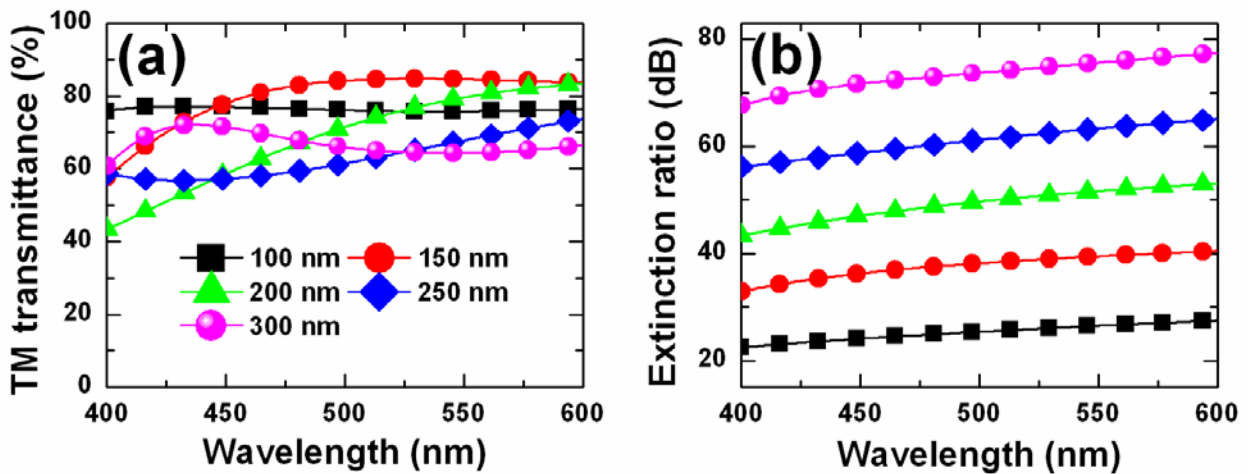


**Figure 6.4** Dependence of polarization performance on metal thickness.

As discussed in Chapter 4 of metal subwavelength grating for THz polarizer, metal thickness will greatly influence the polarization performance. The simulation results of the effect of metal thickness are shown in **Figure 6.4**. The TM transmittance does not change dramatically and shows an oscillating dependence on metal thickness, which can be understood by considering the cavity mode of TM-polarized light. The air gaps between metal wires can be treated as slit waveguides, where the metal wires serve as cladding and the length of the

waveguides is equal to metal thickness. It is known that there are reflections at the two ends of the waveguide (top and bottom interface with air) due to impedance mismatch. The multiple reflection results in a Fabry-Pérot resonant cavity, leading to the oscillating behavior of metal thickness dependent TM transmittance. However for the TE case, the electromagnetic wave inside the slit waveguide is an evanescent wave as the wavelengths of incident waves are larger than its cut-off wavelength. The evanescent character of the electromagnetic fields leads to the dramatically decreased transmittance as metal thickness increases. As a result, ER increases almost linearly as metal thickness increases. Since it is difficult to fabricate high-aspect-ratio metallic nanostructures, the metal thickness is chosen to be 200 nm.

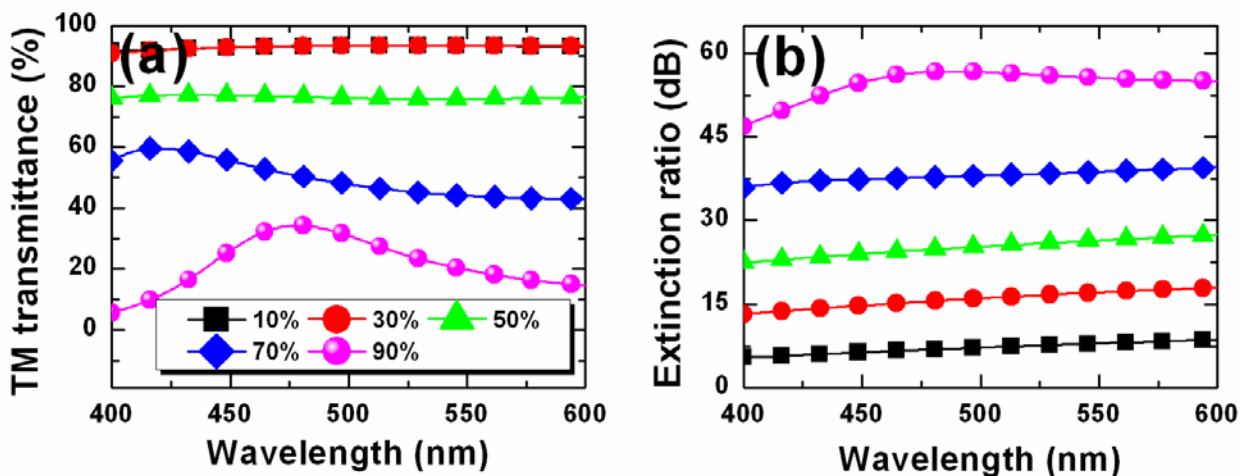


**Figure 6.5** Dependence of polarization performance on grating duty cycle.

Lastly, the effect of duty cycle (or metal occupation ratio) is examined and shown in **Figure 6.5**.

Again, the TM transmittance and ER are a trade-off as for duty cycle. From effective medium theory, we know that the grating layer behaves more like a pure metal layer for larger duty

cycles. So the TM transmittance decreases with duty cycle. While for TE wave, the transmittance decreases exponentially when the air gap between metal wires decreases, as the wavelength is larger than the cut-off wavelength. The duty cycle is chosen as 50% by considering the overall performance.

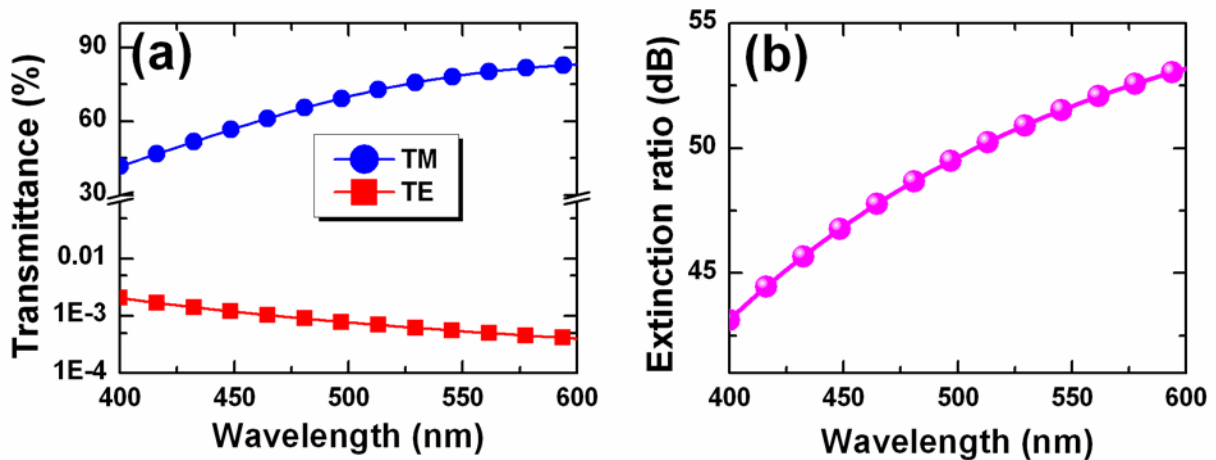


**Figure 6.6** FDTD simulation results of the polarization performance of grating with optimized parameters.

In summary of the above simulations, optimized grating parameters are: Al grating with period 200 nm, Al thickness 200 nm and 50% duty cycle. **Figure 6.6** shows the transmittance and ER of the optimized grating. It can be seen that the transmittance is larger than 50% for wavelengths larger than 450 nm (blue LEDs and green LEDs), and the overall ER is greater than 40 dB. The higher performance at longer wavelengths is attributed to the larger wavelength-to-period ratio.

## 6.3 Polarized LED fabrication

### 6.3.1 GaN LED fabrication

The GaN wafer used for polarized LED fabrication was grown on a *c*-plane sapphire substrate by metal organic chemical vapor deposition (MOCVD). The LED structure consists of 2  $\mu\text{m}$  n-GaN:Si grown on GaN template on sapphire, 5 periods of GaN/InGaN quantum well and 150 nm p-GaN:Mg.



**Figure 6.7** Schematic diagrams of the fabrication steps of GaN LED.

The processing steps to fabricate the GaN LED are schematically illustrated in **Figure 6.7**. Prior to fabrication, the GaN LED wafer was cleaned by hydrochloric acid (HCl), solvents (acetone, IPA) and DI water to remove organic and metal contaminations. 10 nm Ni was then deposited on top of the cleaned wafer surface by e-beam evaporation at a rate of 0.1 nm/s, followed by deposition of 150 nm indium tin oxide (ITO) by sputtering (Figure 6.7(1)). Photolithography was performed to define LED mesa (Figure 6.7(2)). The patterned sample was submerged into HCl: H<sub>2</sub>O (1:1) for 10 seconds to remove exposed ITO and Ni layer. The exposed GaN was then etched by ICP under pressure of 5 mTorr for 150 seconds. The etching depth was ~ 1 μm to ensure the n-GaN layer was exposed, which lays underneath the p-GaN layer and multiple quantum wells (MQW) (Figure 6.7(3)). BCl<sub>3</sub> (20 sccm) and Cl<sub>2</sub> (10 sccm) were used as etching gases. After removal of residual photoresist by acetone, the sample was annealed at 600 °C in air for 2 minutes to form Ni/ITO ohmic contact to p-GaN. Ni/ITO ohmic contact possesses the advantages of higher transmittance (> 85% at 470 nm), better current spreading, higher output power and less leakage current compared to conventional contacts Ni/Au or ITO [87]. After p-contact, photolithography was performed again to form the n-contact. Ti (5 nm)/Al (200 nm)/Ni (10 nm)/Au (100 nm) layers as n-contact metals were evaporated onto the exposed n-GaN windows through e-beam evaporation. After stripping photoresist (lift-off), the sample was annealed at 750 °C for 45 seconds in N<sub>2</sub> ambient to complete the n-contact fabrication (Figure 6.7(4)). Finally, a p-pad consisting of 200 nm Au was formed on top of the p-contact by photolithography, metal deposition and lift-off (Figure

6.7(5)). The p-pad helps to spread current and facilitates testing or wire bonding. The GaN LED was finished after p-pad formation.

### 6.3.2 Subwavelength Al grating fabrication

The processing steps to fabricate Al subwavelength gratings are schematically shown in **Figure 6.8**. Firstly 200 nm Al was deposited on top of the substrate (GaN LED or quartz) by e-beam evaporation at 0.2 nm/s. 50 nm SiO<sub>2</sub> was then evaporated on top of the aluminum also by e-beam evaporation at a rate of 0.1 nm/s. The SiO<sub>2</sub> layer served as hard mask during ICP etching of Al. Diluted e-beam lithography resist (ZEP-520A, 1:1 with Anisol) was then spun coated onto the sample at 3000 rpm for 90 seconds and baked on a hotplate at 180 °C for 2 minutes. After exposure to high energy electron beam and developing, grating pattern with a period of 200 nm was formed on the EBL resist. The grating pattern was transferred to underneath SiO<sub>2</sub> by RIE etching. CHF<sub>3</sub> (25 sccm) and Ar (25 sccm) were used as etching gases. Under a pressure of 30 mTorr and power of 200W, RIE was carried out for 90 seconds. The grating pattern was further transferred to Al layer by ICP etching. Cl<sub>2</sub> (30 sccm) and BCl<sub>3</sub> (40 sccm) were used as etching gases. Under 5 mTorr pressure, 200 W RIE power and 500 W ICP power, ICP etching was carried out for 30 seconds. Finally, the residual resist and SiO<sub>2</sub> were stripped off by RIE. It is found that the ICP parameters are critical in transferring the grating pattern to Al layer [88]. SEM images of the sample at different fabrication steps are shown in **Figure 6.9**. It can be seen that the final Al wires have rectangular cross-sectional profile and smooth side walls. The occasional small bumps at the top surface are probably caused by the

non-uniform grains in Al and SiO<sub>2</sub> films deposited by e-beam evaporation.

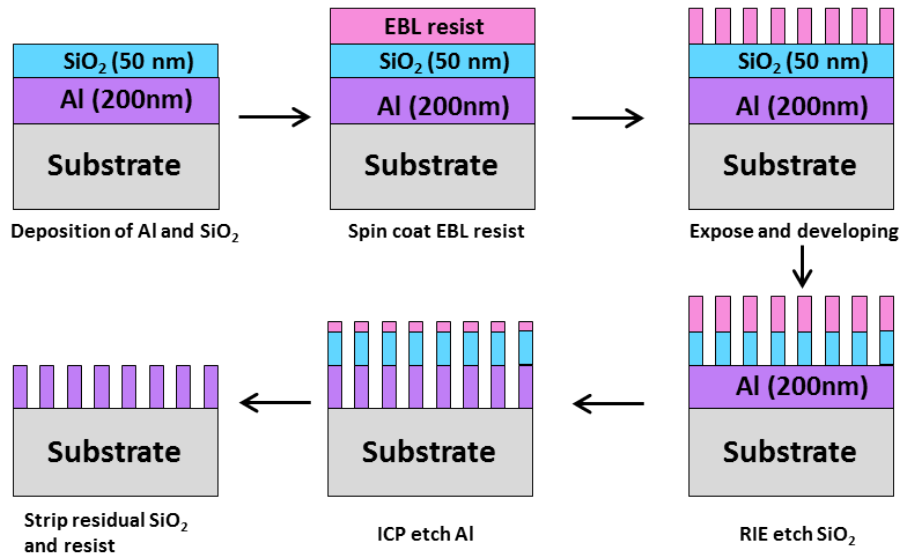


**Figure 6.8** Schematic diagrams showing the fabrication steps of Al subwavelength grating.

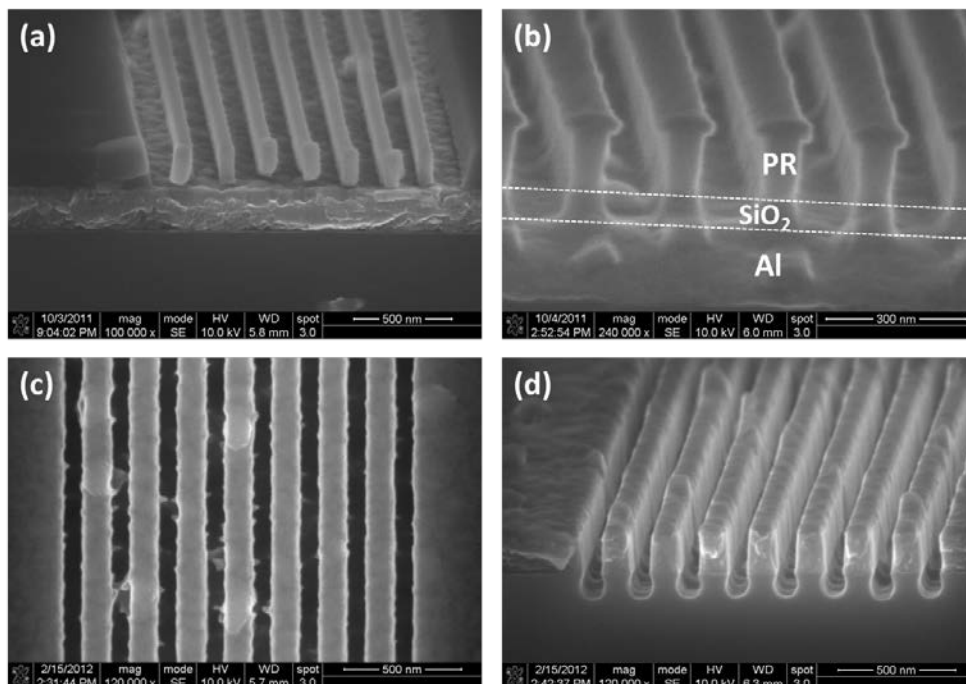


**Figure 6.9** SEM pictures of (a) resist grating after e-beam exposure and developing; (b) after RIE etching of SiO<sub>2</sub>; (c) top view of the final Al grating; (d) cross-sectional view of the final Al grating.



## 6.4 Polarized LED Characterization

After fabrication, the current-voltage (I-V) characteristic and output power of the GaN LED were measured by probe station, semiconductor parameter analyzer and power meter. The results in **Figure 6.10** show that the turn-on voltage of the GaN LED is around 3.5 V. Forward voltage of 5.2 V is needed to achieve 20 mA current. The camera image of a lighted LED die under 4.5 V forward bias shows that the LED is very bright and works very well. The uniform lighting area indicates the good lateral current spreading by the Ni/ITO p-contact layer. The output power from the front LED surface as a function of injection current was measured by mounting the photodetector 20 mm above the LED surface. The result shows that the output power is 73.9  $\mu\text{W}$  under an injection current of 20 mA. The output power increases with current. However at a higher current, the rate of increment decreases and the output power tends to saturate. It should be pointed out that the output power measurement can only give a qualitative information as the light emitted into other directions are not collected by the detector. An integral sphere should be used if a more accurate measurement is required.

We also measured the electroluminescence (EL) spectra of the LED under different injection currents, as shown in **Figure 6.11**. It can be seen that the peak emission wavelength is around 520 nm. The peak wavelength blue shifts as the current increases from 1 mA to 70 mA. However, the peak wavelength turns to red shift when the current is increased further. This can be understood as follow: The GaN LEDs were fabricated with c-plane (polar plane) GaN substrates. The piezoelectric effect associated with polar plane grown GaN induces a huge

electric field in the quantum well (on the order of several MV/cm). Due to this electric field, the energy levels of electrons and holes in the quantum well are altered and the energy of the bound states in the quantum well is decreased, which effectively decreases the bandgap and is known as quantum-confined stark effect (QCSE). When the LED is lit, the injected carriers screen the electric field, relieving the QCSE, which in turn results in the blue shift in the emission peak. While, at higher injection current, the carriers inside the quantum well tend to saturate, so is the screening effect. At further higher currents (forward voltages), the QCSE will dominate and causes the emission peak to red shift again. In addition to altering the peak position, the electric field also shifts the electron and hole wavefunctions to opposite sides of the quantum well, decreasing the overlap integral and reducing the recombination efficiency, so the EL intensity will not increase linearly with injection current. The thermal effect at high currents will also decrease the recombination efficiency.

The EL intensity also tends to saturate at a high injection current, consistent with the output power measurement. The various characterizations performed above show that the fabricated LED performs very well and is suitable to be integrated with Al nanogratings.

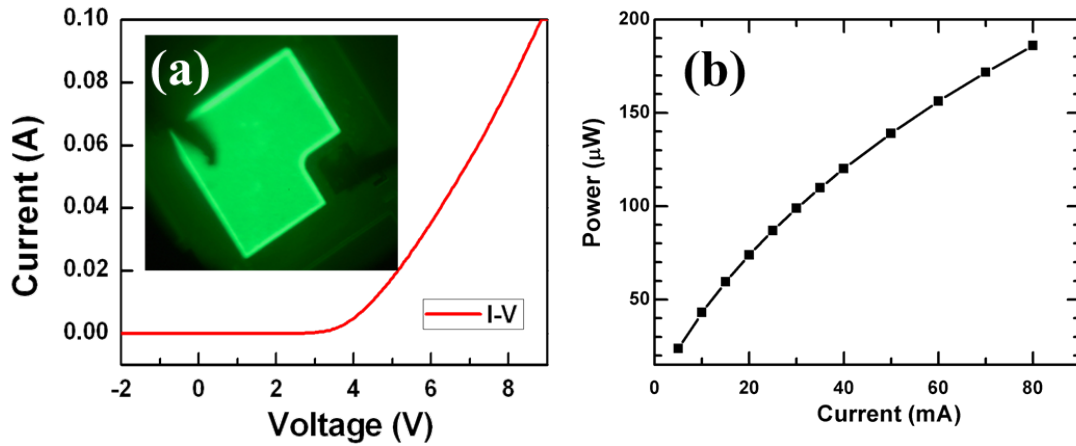


**Figure 6.10** (a) I-V curve of the fabricated LED, showing a turn-on voltage of 3.5 V. (b) Output power from the front surface of LED as a function of injection current. The photodetector of the power meter was placed 20 mm above the LED surface.

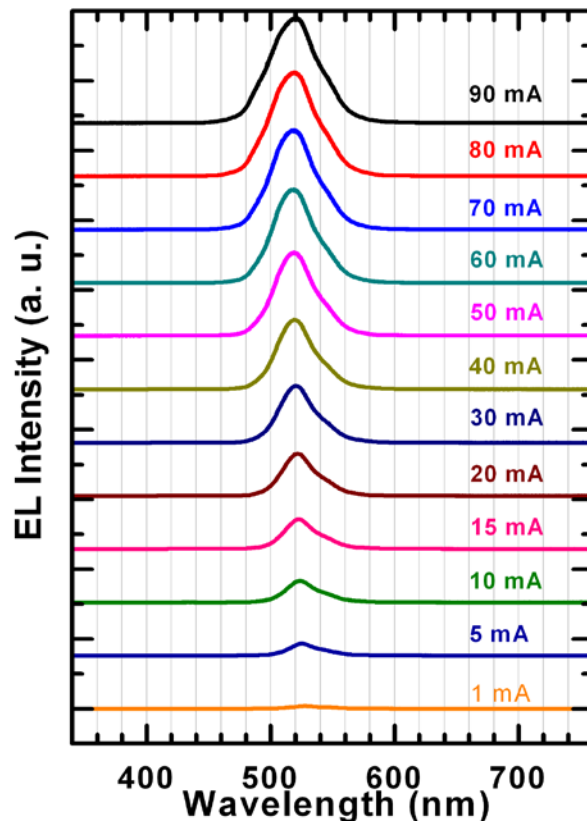


**Figure 6.11** Electroluminescence (EL) spectra of the fabricated GaN LED under different injection currents. There is a slight blue-shift as the current is increased from 1 to 70 mA.

Next, the performance of the Al nanograting on quartz substrate as a polarizer alone was characterized using CRAIC UV-VIS-NIR microspectrometer. The results are shown in **Figure 6.12**. It can be seen that the transmittance of the polarizer is about 50%, i.e. about a half of the incident light (TE component) is blocked by the polarizer. The polarization ratio ( $T_{TM}/T_{TE}$ ) is  $\sim 200$  at the vicinity of 520 nm. The Al nanograting shows high polarization performance. The discrepancy with simulation results shown in Figure 6.6 can be assigned to fabrication and material imperfection, such as grating non-uniformity, non-smooth surface and side wall, oxidation of Al and so on.

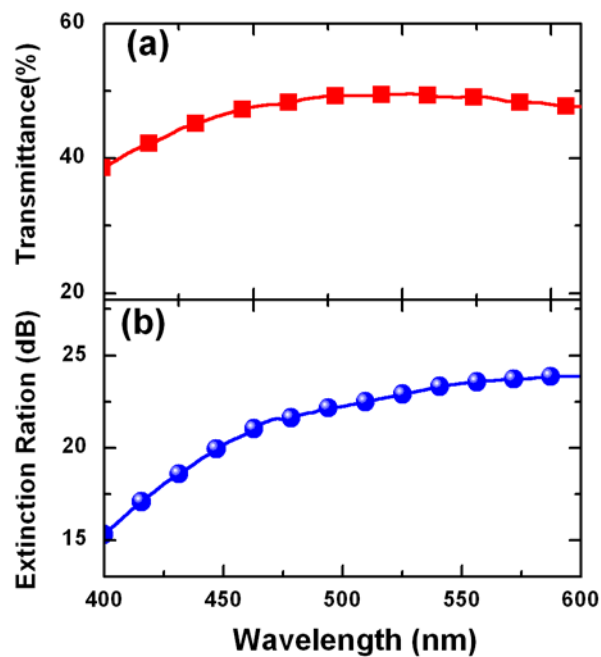


**Figure 6.12** Transmission and ER of the Al nanograting on quartz substrate. The nanograting's parameters are: Al thickness 190 nm, grating period 200 nm, and duty cycle 55%.

Finally, the GaN LED integrated with the Al grating was tested. A polarizer was mounted on

top of the lighted LED and a power meter was used to measure the light intensity. The emitted intensity was measured as a function of the polarizer angle. During measurement, the polarizer was rotated in steps of 10 degrees. **Figure 6.13** shows the measurement results plotted at 525 nm. It can be seen that the measured intensity depends strongly on the polarizer angle, indicating a linearly polarized light emitted from the GaN LED. It is found that the ER is ~3.22 dB.

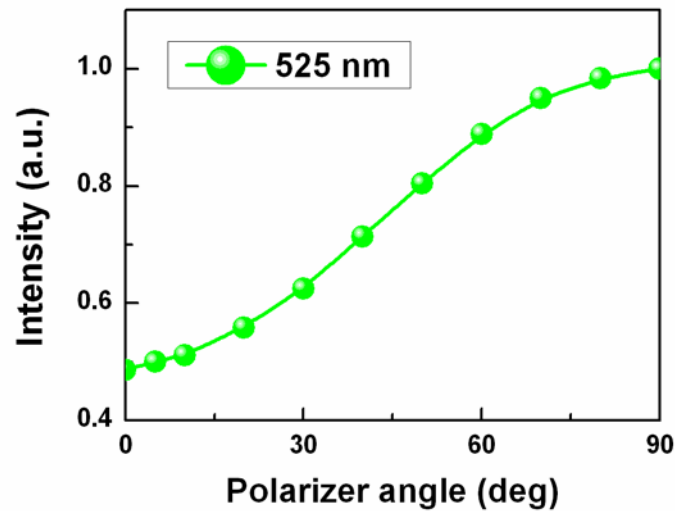


**Figure 6.13** Polarization measurement of the polarized green GaN LED.

The measured polarization ratio was low compared to Al gratings on quartz or the simulation results. It is also abnormal as compared to the blue GaN LED fabricated. As shown in **Figure 6.14**, the ER of the same grating on blue GaN LED was 7.5 dB when measured at 450 nm. From subwavelength grating polarizer theory, the 200 nm period Al grating polarizer should perform better at 525 nm than at 450 nm. The two fabricated samples are carefully examined and it is found that the Al grating on the green LED sample has poor morphology (**Figure 6.15**)

caused by the surface roughing of the original green GaN LED sample. It is believed that the Al grating will render a higher polarization ratio if the original LED surface is smoother.

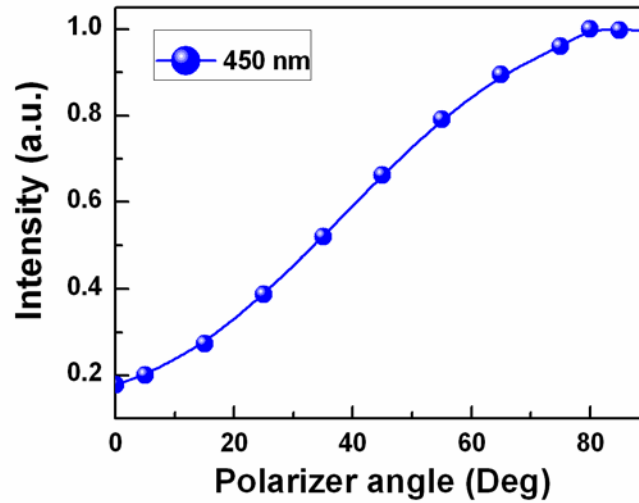


**Figure 6.14** Polarization measurement of the polarized blue GaN LED.

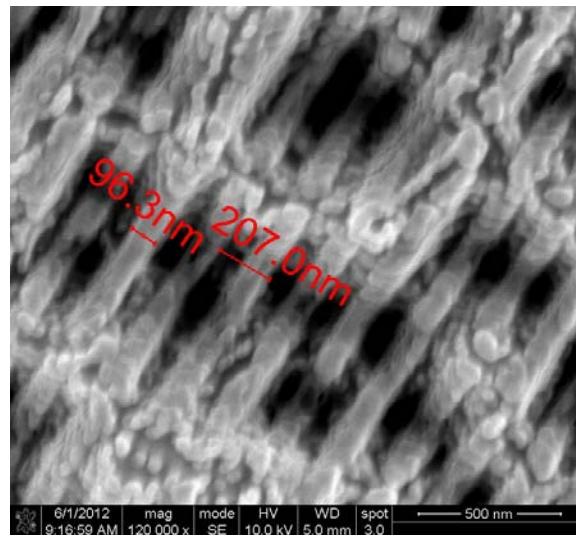


**Figure 6.15** SEM image of the fabricated Al nanograting on a green GaN LED.

## 6.5 Summary

In summary, we demonstrated polarized light emission directly from the InGaN/GaN MQW LED by integrating it with a subwavelength Al grating. The grating parameters were optimized by FDTD simulations. Considering the overall polarization performance and fabrication complexity, Al grating with period 200 nm, Al thickness 200 nm and duty cycle 50% was chosen. The polarized GaN LEDs show a polarization ratio of 5.6 for blue LED and 2.1 for green LED. The poor performance of green LED is due to the surface roughing. A higher polarization performance is expected if a smooth-surface green LED is utilized.

## **Chapter 7 Summary and Future Work**

To summarize, I have demonstrated three devices incorporating subwavelength gratings for polarization control in THz and visible frequency ranges.

In Chapter 1, after giving an overview of the background of this work, motivation and organization of the thesis are outlined. Fundamental theories that are necessary to understand the following chapters, such as finite difference in time-domain and surface plasmons are then briefly described in Chapter 2. The software used to carry out simulations is also introduced.

In Chapter 3, the principles of the fabrication and characterization equipment used in the thesis are explained in details. In particular, the processing parameters adopted and specifications of the equipment are given, which are crucial in fabricating devices with desired properties and analyzing measurement results properly.

Chapter 4 demonstrates one application of subwavelength grating in THz frequency range, i.e. high performance THz polarizer. By using bilayer subwavelength grating other than single-layer being adopted previously, an extremely high polarization performance has been obtained. The average ER is 69.9 dB in frequency range of 0.6 – 3 THz and 84.9 dB at 1.67 THz, the highest values ever demonstrated. The demonstrated polarizer will be widely used in various THz applications, considering its extremely good performance, ease of fabrication and compatibility with semiconductor process.

Chapter 5 is dedicated to the experimentally demonstration of the tunable THz plasmonic



response of InSb subwavelength gratings by optically tuning the carrier concentration. The InSb subwavelength grating shows polarization-sensitive response due to the inherent nature of surface plasmons. Resonance frequency of the InSb subwavelength grating can be tuned in a broad THz frequency range. By optically pumping the InSb with a 405 nm wavelength laser emitting at 120 mW, the transmittance at 1.5 THz was reduced from 0.6 to 0.32, a change of 46.7%. At a laser pump fluence of  $0.74 \mu\text{J}/\text{cm}^2$ , the excited carrier lifetime was determined to be 834 ps using optical pump-THz probe technique, giving a potentially high-speed THz modulator with modulation speed up to 1.2 GHz. The direct optical tuning and modulation of the plasmonic response of InSb subwavelength grating provides much flexibility and new possibilities in future THz component development.

Chapter 6 demonstrates polarized light emission directly from the InGaN/GaN MQW LED by integrating it with a subwavelength Al grating. Al grating with period 200 nm, Al thickness 200 nm and duty cycle 50% was fabricated directly on top of the LED chip. The polarized GaN LEDs show a polarization ratio of 5.6 for blue GaN LEDs and 2.1 for green ones. The demonstrated polarized LED is compact and compatible with semiconductor processing, enabling its applications in LCD backlight, 3D display, and polarization-resolved microscopy. Through the accomplishment of the preceding research topics, I anticipate a number of possible works worth doing in the future, in order to further explore the potential applications of subwavelength gratings. In particular, there are several specific ideas:

- It has been shown in Chapter 4 that the distance between two metallic grating layers greatly affects the performance of bilayer polarizer, especially when strong coupling between the two layers occurs at a small spacing. However, the coupling mechanism and strength are still not clear. It deserves future investigation by carrying out more detailed simulation and fabrication. Novel polarization devices making use of the coupling mechanism are anticipated.
- Through the verification in THz frequency range, it has confirmed that bilayer subwavelength grating structure is superior to single layer one in term of polarization performance. It is natural to extend this concept of bilayer subwavelength grating structure to the polarized GaN LED topic and integrate bilayer Al nanograting with GaN LED chips. By doing so, it is expected that the polarization ratio of the polarized GaN LED will be greatly enhanced.
- One drawback of the polarized GaN LED demonstrated is the low throughput resulting from electron-beam lithography. However, this can be overcome by patterning the Al subwavelength grating on the backside of LED wafer with nanoimprinting lithography or laser interference lithography. By using reflective top contacts, light emitted from the quantum wells will be directed to the Al subwavelength grating residing on the backside of sapphire substrate and convert to be linearly polarized. Easier fabrication steps and higher throughput are expected.

- It has been demonstrated that when the metal nano-structures are close to MQWs, the spontaneous emission behavior will be greatly affected by surface plasmons, resulting in higher emission luminescence [89]. My preliminary result shows that the polarization ratio of polarized GaN LED is also affected by the distance between Al subwavelength grating and LED MQWs. More experiments and detail measurements are still needed to confirm the observation and explore theoretical explanations.

## Bibliography

- [1] Available: <http://www.itrs.net/>
- [2] H. Hertz, *Electric waves*. London: McMillan and Company, Ltd, 1893.
- [3] G. H. Thomson, "Uber den Durchgang Hertzscher Wellen durch Gitter," *Ann. Physik*, vol. 22, pp. 365-390, 1907.
- [4] J. J. Thomson, *Recent Researches in Electricity and Magnetism*. Oxford: Clarendon Press, 1893.
- [5] H. Lamb, "On the reflection and transmission of electric waves by a metallic grating," *Proceedings of the London Mathematical Society*, vol. 1, pp. 523-546, 1897.
- [6] W. V. Ignatowsky, "Zur theorie der Gitter," *Ann. Physik*, vol. 44, 1914.
- [7] W. Wessel, "Uber den Durchgang elektrischer Wellen durch Drahtgitter " *Hochfrequenetechn. Elekt. Akust*, vol. 54, pp. 62-70, 1939.
- [8] R. Hornejager, "Uber die Beugung elektromagnetischer Wellen an einem Drahtgitter," *Ann. Physik*, vol. 4, pp. 25-35, 1948.
- [9] E. A. Lewis and J. P. Casey, "Metal Grid Interference Filter," *J. Opt. Soc. Am.*, vol. 41, pp. 360-360, 1951.
- [10] W. K. Pursley, doctoral thesis, University of Michigan, 1956.
- [11] G. R. Bird and M. Parrish Jr, "The wire grid as a near-infrared polarizer," *JOSA*, vol. 50, p. 886, 1960.
- [12] M. Hass and M. O'Hara, "Sheet infrared transmission polarizers," *Applied optics*, vol. 4, pp. 1027-1031, 1965.
- [13] J. Auton, "Infrared transmission polarizers by photolithography," *Applied optics*, vol. 6, pp. 1023-1027, 1967.
- [14] P. K. Cheo and C. D. Bass, "Efficient Wire-Grid Duplexer Polarizer for CO<sub>2</sub> Lasers," *Applied Physics Letters*, vol. 18, pp. 565-567, 1971.
- [15] S.-W. Ahn, K.-D. Lee, J.-S. Kim, S. H. Kim, J.-D. Park, S.-H. Lee, *et al.*, "Fabrication of a 50 nm half-pitch wire grid polarizer using nanoimprint lithography," *Nanotechnology*, vol. 16, p. 1874, 2005.

- [16] K. W. Sun, S.-C. Huang, A. Kechiantz, and C.-P. Lee, "Subwavelength gratings fabricated on semiconductor substrates via E-beam lithography and lift-off method," *Optical and Quantum Electronics*, vol. 37, pp. 425-432, 2005.
- [17] J. Si and Y. Wu, "Fabrication of infrared wire grid polarizer by ion beam milling," *Holographic optical elements and displays: 4-5 November 1996, Beijing, China*, vol. 2885, p. 196, 1996.
- [18] S. Y. Chou, P. R. Krauss, and P. J. Renstrom, "Imprint Lithography with 25-Nanometer Resolution," *Science*, vol. 272, pp. 85-87, April 5, 1996 1996.
- [19] J. J. Wang, L. Chen, X. Liu, P. Sciortino, F. Liu, F. Walters, *et al.*, "30-nm-wide aluminum nanowire grid for ultrahigh contrast and transmittance polarizers made by UV-nanoimprint lithography," *Applied Physics Letters*, vol. 89, p. 141105, 2006.
- [20] T. Weber, T. Käsebier, A. Szeghalmi, M. Knez, E.-B. Kley, and A. Tünnermann, "High aspect ratio deep UV wire grid polarizer fabricated by double patterning," *Microelectronic Engineering*, 2012.
- [21] T. Weber, T. Käsebier, A. Szeghalmi, M. Knez, E.-B. Kley, and A. Tünnermann, "Iridium wire grid polarizer fabricated using atomic layer deposition," *Nanoscale research letters*, vol. 6, pp. 1-4, 2011.
- [22] Z. Yang, M. Zhao, N. Dai, G. Yang, H. Long, Y. Li, *et al.*, "Broadband polarizers using dual-layer metallic nanowire grids," *Photonics Technology Letters, IEEE*, vol. 20, pp. 697-699, 2008.
- [23] S. Y. Chou and W. Deng, "Subwavelength amorphous silicon transmission gratings and applications in polarizers and waveplates," *Applied Physics Letters*, vol. 67, pp. 742-744, 1995.
- [24] J. Kim, Y.-W. Lim, and S.-D. Lee, "Brightness-enhanced transmissive liquid crystal display having single-cell gap in vertically aligned configuration," *Jpn. J. Appl. Phys*, vol. 45, pp. 810-812, 2006.
- [25] T. Doumuki and H. Tamada, "An aluminum-wire grid polarizer fabricated on a gallium-arsenide photodiode," *Applied Physics Letters*, vol. 71, pp. 686-688, 1997.
- [26] G. Zhang, C. Wang, B. Cao, Z. Huang, J. Wang, B. Zhang, *et al.*, "Polarized GaN-based LED with an integrated multi-layer subwavelength structure," *Optics Express*, vol. 18, pp. 7019-7030, 2010.
- [27] B. Ferguson and X.-C. Zhang, "Materials for terahertz science and technology,"

- Nature Materials*, vol. 1, pp. 26-33, 2002.
- [28] S. M. Sze and K. K. Ng, *Physics of Semiconductor Devices*: Wiley, 2006.
- [29] C. Sirtori, "Applied physics: Bridge for the terahertz gap," *Nature*, vol. 417, pp. 132-133, 2002.
- [30] M. Tonouchi, "Cutting-edge terahertz technology," *Nature Photonics*, vol. 1, pp. 97-105, 2007.
- [31] B. S. Williams, "Terahertz quantum-cascade lasers," *Nature Photonics*, vol. 1, pp. 517-525, 2007.
- [32] R. Köhler, A. Tredicucci, F. Beltram, H. E. Beere, E. H. Linfield, A. G. Davies, *et al.*, "Terahertz semiconductor-heterostructure laser," *Nature*, vol. 417, pp. 156-159, 2002.
- [33] F. Sizov and A. Rogalski, "THz detectors," *Progress in Quantum Electronics*, vol. 34, pp. 278-347, 2010.
- [34] H.-T. Chen, W. J. Padilla, J. M. O. Zide, A. C. Gossard, A. J. Taylor, and R. D. Averitt, "Active terahertz metamaterial devices," *Nature*, vol. 444, pp. 597-600, 2006.
- [35] O. Losev, "Luminous carborundum [silicon carbide] detector and detection with crystals," *Telegrafiya i Telefoniya bez Provodov*, vol. 44, pp. 485-494, 1927.
- [36] N. Zheludev, "The life and times of the LED—a 100-year history," *Nature Photonics*, vol. 1, pp. 189-192, 2007.
- [37] Available: <http://www-opto.e-technik.uni-ulm.de/lehre/cs/>
- [38] S. Nakamura, T. Mukai, and M. Senoh, "High-power GaN pn junction blue-light-emitting diodes," *Japanese Journal of Applied Physics*, vol. 30, pp. L1998-L2001, 1991.
- [39] Available: <http://www.lumerical.com/tcad-products/fdtd/>
- [40] W. L. Barnes, A. Dereux, and T. W. Ebbesen, "Surface plasmon subwavelength optics," *Nature*, vol. 424, pp. 824-830, 2003.
- [41] K.-i. Murata and H. Tanaka, "Surface-wetting effects on the liquid–liquid transition of a single-component molecular liquid," *Nat Commun*, vol. 1, p. 16, 2010.
- [42] S. A. Maier, *Plasmonics: fundamentals and applications*: Springer, 2007.
- [43] J. Pendry, L. Martin-Moreno, and F. Garcia-Vidal, "Mimicking surface plasmons with

- structured surfaces," *Science*, vol. 305, pp. 847-848, 2004.
- [44] A. P. Hibbins, B. R. Evans, and J. R. Sambles, "Experimental verification of designer surface plasmons," *Science*, vol. 308, pp. 670-672, 2005.
- [45] I. Haller, M. Hatzakis, and R. Srinivasan, "High-resolution positive resists for electron-beam exposure," *IBM Journal of Research and Development*, vol. 12, pp. 251-256, 1968.
- [46] A. Mayadas and R. Laibowitz, "One-dimensional superconductors," *Physical Review Letters*, vol. 28, pp. 156-158, 1972.
- [47] W. W. Hu, K. Sarveswaran, M. Lieberman, and G. H. Bernstein, "Sub-10 nm electron beam lithography using cold development of poly (methylmethacrylate)," *Journal of Vacuum Science & Technology B: Microelectronics and Nanometer Structures*, vol. 22, pp. 1711-1716, 2004.
- [48] P. Griffiths and J. A. De Haseth, *Fourier transform infrared spectrometry* vol. 171: Wiley-Interscience, 2007.
- [49] B. C. Smith, *Fundamentals of Fourier transform infrared spectroscopy*: CRC press, 2011.
- [50] Y. S. Lee, *Principles of Terahertz Science and Technology*: Springer, 2008.
- [51] C.-F. Hsieh, Y.-C. Lai, R.-P. Pan, and C.-L. Pan, "Polarizing terahertz waves with nematic liquid crystals," *Optics letters*, vol. 33, pp. 1174-1176, 2008.
- [52] A. Wojdyla and G. Gallot, "Brewster's angle silicon wafer terahertz linear polarizer," *Optics Express*, vol. 19, pp. 14099-14107, 2011.
- [53] A. Costley, K. Hursey, G. Neill, and J. Ward, "Free-standing fine-wire grids: their manufacture, performance, and use at millimeter and submillimeter wavelengths," *JOSA*, vol. 67, pp. 979-981, 1977.
- [54] L. Ren, C. L. Pint, L. G. Booshehri, W. D. Rice, X. Wang, D. J. Hilton, *et al.*, "Carbon nanotube terahertz polarizer," *Nano Letters*, vol. 9, pp. 2610-2613, 2009.
- [55] J. Kyoung, E. Y. Jang, M. r. D. Lima, H.-R. Park, R. O. Robles, X. Lepró, *et al.*, "A reel-wound carbon nanotube polarizer for terahertz frequencies," *Nano Letters*, vol. 11, pp. 4227-4231, 2011.
- [56] K. Takano, H. Yokoyama, A. Ichii, I. Morimoto, and M. Hangyo, "Wire-grid polarizer sheet in the terahertz region fabricated by nanoimprint technology," *Optics letters*, vol.

36, pp. 2665-2667, 2011.

- [57] I. Yamada, K. Takano, M. Hangyo, M. Saito, and W. Watanabe, "Terahertz wire-grid polarizers with micrometer-pitch Al gratings," *Optics letters*, vol. 34, pp. 274-276, 2009.
- [58] L. Sun, Z.-H. Lv, W. Wu, W.-T. Liu, and J.-M. Yuan, "Double-grating polarizer for terahertz radiation with high extinction ratio," *Applied optics*, vol. 49, pp. 2066-2071, 2010.
- [59] L. Y. Deng, J. H. Teng, L. Zhang, Q. Y. Wu, H. Liu, X. H. Zhang, *et al.*, "Extremely high extinction ratio terahertz broadband polarizer using bilayer subwavelength metal wire-grid structure," *Applied Physics Letters*, vol. 101, p. 011101, 2012.
- [60] J. d. Boer, G. Kroesen, W. De Zeeuw, and F. De Hoog, "Improved polarizer in the infrared: two wire-grid polarizers in tandem," *Optics letters*, vol. 20, pp. 800-802, 1995.
- [61] F. J. Garcia-Vidal, L. Martin-Moreno, T. Ebbesen, and L. Kuipers, "Light passing through subwavelength apertures," *Reviews of Modern Physics*, vol. 82, p. 729, 2010.
- [62] J. J. Wang, F. Walters, X. Liu, P. Sciortino, and X. Deng, "High-performance, large area, deep ultraviolet to infrared polarizers based on 40 nm line/78 nm space nanowire grids," *Applied Physics Letters*, vol. 90, pp. 061104-061104-3, 2007.
- [63] L. Deng, J. Teng, H. Liu, Q. Y. Wu, J. Tang, X. Zhang, *et al.*, "Direct Optical Tuning of the Terahertz Plasmonic Response of InSb Subwavelength Gratings," *Advanced Optical Materials*, vol. 1, pp. 128-132, 2013.
- [64] C. A. Schmuttenmaer, "Exploring dynamics in the far-infrared with terahertz spectroscopy," *Chemical Reviews-Columbus*, vol. 104, pp. 1759-1780, 2004.
- [65] N. Yu, J. Fan, Q. J. Wang, C. Pflügl, L. Diehl, T. Edamura, *et al.*, "Small-divergence semiconductor lasers by plasmonic collimation," *Nature Photonics*, vol. 2, pp. 564-570, 2008.
- [66] Y. Kawano and K. Ishibashi, "An on-chip near-field terahertz probe and detector," *Nature Photonics*, vol. 2, pp. 618-621, 2008.
- [67] H.-T. Chen, W. J. Padilla, M. J. Cich, A. K. Azad, R. D. Averitt, and A. J. Taylor, "A metamaterial solid-state terahertz phase modulator," *Nature Photonics*, vol. 3, pp. 148-151, 2009.
- [68] M. Seo, J. Kyoung, H. Park, S. Koo, H.-s. Kim, H. Bernien, *et al.*, "Active Terahertz



- Nanoantennas Based on VO<sub>2</sub>Phase Transition," *Nano Letters*, vol. 10, pp. 2064-2068, 2010.
- [69] W. M. Zhu, A. Q. Liu, X. M. Zhang, D. P. Tsai, T. Bourouina, J. H. Teng, *et al.*, "Switchable magnetic metamaterials using micromachining processes," *Advanced Materials*, vol. 23, pp. 1792-1796, 2011.
- [70] C. R. Williams, S. R. Andrews, S. A. Maier, A. I. Fernández-Domínguez, L. Martín-Moreno, and F. J. García-Vidal, "Highly confined guiding of terahertz surface plasmon polaritons on structured metal surfaces," *Nature Photonics*, vol. 2, pp. 175-179, 2008.
- [71] S. A. Maier and S. R. Andrews, "Terahertz pulse propagation using plasmon-polariton-like surface modes on structured conductive surfaces," *Applied Physics Letters*, vol. 88, pp. 251120-251120-3, 2006.
- [72] S. Hanham, A. Fernández-Domínguez, J. Teng, S. Ang, K. Lim, S. Yoon, *et al.*, "Broadband Terahertz Plasmonic Response of Touching InSb Disks," *Advanced Materials*, vol. 24, pp. OP226-OP230, 2012.
- [73] P. Y. Yu and M. Cardona, *Fundamentals of Semiconductors: Physics and Materials Properties*: Springer Berlin Heidelberg, 2010.
- [74] V. Giannini, A. Berrier, S. A. Maier, J. A. Sánchez-Gil, and J. G. Rivas, "Scattering efficiency and near field enhancement of active semiconductor plasmonic antennas at terahertz frequencies," *Opt. Express*, vol. 18, pp. 2797-2807, 2010.
- [75] J. G. Rivas, C. Janke, P. H. Bolivar, and H. Kurz, "Transmission of THz radiation through InSb gratings of subwavelength apertures," *Opt. Express*, vol. 13, pp. 847-859, 2005.
- [76] E. Litwin-Staszewska, W. Szymańska, and R. Piotrkowski, "The electron mobility and thermoelectric power in InSb at atmospheric and hydrostatic pressures," *physica status solidi (b)*, vol. 106, pp. 551-559, 1981.
- [77] K. Lim, S. Yoon, and H. Pham, "Properties of InSbN grown on GaAs by radio frequency nitrogen plasma-assisted molecular beam epitaxy," *Journal of Physics D: Applied Physics*, vol. 42, p. 135419, 2009.
- [78] D. Grischkowsky, S. Keiding, M. Van Exter, and C. Fattinger, "Far-infrared time-domain spectroscopy with terahertz beams of dielectrics and semiconductors," *J. Opt. Soc. Am. B*, vol. 7, pp. 2006-2015, 1990.

- [79] D. E. Aspnes and A. A. Studna, "Dielectric Functions and Optical-Parameters of Si, Ge, GaP, GaAs, GaSb, InP, InAs, and InSb from 1.5 to 6.0 eV," *Physical Review B*, vol. 27, pp. 985-1009, 1983.
- [80] E. D. Palik, *Handbook of Optical Constants of Solids: Index* vol. 3: Academic press, 1998.
- [81] P. Parkinson, H. J. Joyce, Q. Gao, H. H. Tan, X. Zhang, J. Zou, *et al.*, "Carrier lifetime and mobility enhancement in nearly defect-free core-shell nanowires measured using time-resolved terahertz spectroscopy," *Nano Letters*, vol. 9, pp. 3349-3353, 2009.
- [82] M. Schall and P. U. Jepsen, "Above-band gap two-photon absorption and its influence on ultrafast carrier dynamics in ZnTe and CdTe," *Applied Physics Letters*, vol. 80, pp. 4771-4773, 2002.
- [83] L. Novotny, "Effective wavelength scaling for optical antennas," *Physical Review Letters*, vol. 98, p. 266802, 2007.
- [84] M. F. Schubert, S. Chhajed, J. K. Kim, E. F. Schubert, and J. Cho, "Polarization of light emission by 460 nm GaInN/GaN light-emitting diodes grown on (0001) oriented sapphire substrates," *Applied Physics Letters*, vol. 91, Jul 30 2007.
- [85] M. F. Schubert, S. Chhajed, J. K. Kim, E. F. Schubert, and J. Cho, "Linearly polarized emission from GaInN lightemitting diodes with polarization-enhancing reflector," *Opt. Express*, vol. 15, pp. 11213-11218, 2007.
- [86] L. Zhang, J. H. Teng, S. J. Chua, and E. A. Fitzgerald, "Linearly polarized light emission from InGaN light emitting diode with subwavelength metallic nanograting," *Applied Physics Letters*, vol. 95, p. 261110, Dec 28 2009.
- [87] Y. Lin, S.-J. Chang, Y.-K. Su, T.-Y. Tsai, C. Chang, S.-C. Shei, *et al.*, "InGaN/GaN light emitting diodes with Ni/Au, Ni/ITO and ITO p-type contacts," *Solid-State Electronics*, vol. 47, pp. 849-853, 2003.
- [88] S.-W. Ahn, K.-D. Lee, J.-S. Kim, S. H. Kim, S. H. Lee, J.-D. Park, *et al.*, "Fabrication of subwavelength aluminum wire grating using nanoimprint lithography and reactive ion etching," *Microelectronic Engineering*, vol. 78, pp. 314-318, 2005.
- [89] K. Okamoto, I. Niki, A. Shvartser, Y. Narukawa, T. Mukai, and A. Scherer, "Surface-plasmon-enhanced light emitters based on InGaN quantum wells," *Nature Materials*, vol. 3, pp. 601-605, 2004.

## List of Acronyms

<b>Acronym</b>	<b>Meaning</b>
1D	one-dimensional
2D	two-dimensional
3D	three-dimensional
BAP	Brewster's angle polarizer
BBO	beta Barium Borate
BWGP	bilayer wire-grid polarizer
CAD	computer-aided design
CD	critical dimensions
DRIE	deep reactive ion etching
DI	deionized
DTGS	deuterated triglycine sulfate
EBL	electron-beam lithography
EL	electroluminescence
EMT	effective medium theory
EO	electro-optical
ER	extinction ratio
FDTD	finite-different in time-domain
FE	field emission
FTIR	Fourier transform infrared spectroscopy
HCl	hydrochloric acid
HMDS	hexamethyldisilazane
ICP	inductively coupled plasma
IPA	isopropyl alcohol
ITO	indium tin oxide
I-V	current-voltage
LCD	liquid crystal display

LCP	liquid crystal polarizer
LED	light emitting diode
LSPR	localized surface plasmon resonance
LT-GaAs	low-temperature-grown GaAs
MBE	molecular beam epitaxy
MQW	multiple quantum wells
OPTP	optical-pump THz-probe spectroscopy
PEC	perfect electrical conductor
PMMA	polymethylmethacrylate
RF	radio frequency
RIE	reactive ion etching
SEM	scanning electron microscopy
SPP	surface plasmon polariton
SPR	surface plasmon resonance
SPs	surface plasmons
SWG	single-layer WGP
TE	transverse electric
THz	terahertz
THz-TDS	terahertz time-domain spectroscopy
TM	transverse magnetic
UV	ultraviolet
VLSI	very large scale integration
WGP	wire-grid polarizer